Parameterization of canopy processes for atmospheric models

Dissertation

zur Erlangung des Doktorgrades

an der Fakultät für Mathematik, Informatik und Naturwissenschaften

Fachbereich Erdsystemwissenschaften

der Universität Hamburg

vorgelegt von

Ge Cheng

aus Zhejiang, China

Hamburg, 2023

Fachbereich Erdsystemwissenschaften

Datum der Disputation:	09.10.2023
Gutachter/innen der Dissertation:	Prof. Dr. K. Heinke Schlünzen
	Prof. Dr. Bernd Leitl
Zusammensetzung der Prüfungskommission:	Prof. Dr. K. Heinke Schlünzen
	Prof. Dr. Bernd Leitl
	Prof. Dr. Jörn Behrens
	PD Dr. Thomas Pohlmann
	Dr. Marcus Thatcher
Vorsitzender des Fach-Promotionsausschusses Erdsystemwissenschaften:	Prof. Dr. Hermann Held
Dekan der Fakultät MIN:	Prof. Dr. Ing. Norbert Ritter

Abstract

Urban and forest canopies have strong effects on boundary layer meteorology by modifying wind and turbulence characteristics, the surface energy balance, and air quality, which further influence weather and climate at various scales. To better understand the interaction between the canopy and the atmosphere, and to investigate the influence of canopies on the Earth's climate system and climate change, it is important to introduce canopies into numerical atmospheric models. This thesis aims to develop a Generalized Canopy Parameterization (GeCap) that is able to represent the most important canopy effects in various high-resolution atmospheric models in a simple, efficient, and generalized way.

A comprehensive analysis was conducted on the forest canopy effects (FCEs) and urban canopy effects (UCEs) on aerodynamics, thermodynamics, hydrology, and air quality. Secondly, a qualitative assessment of FCEs and UCEs compared to grass-covered surfaces was performed to identify the similarities between the FCEs and UCEs, which can be represented by the GeCap in a unified way. Based on this analysis, a conceptual model for GeCap was developed. The conceptual model emphasizes the connections between canopy characteristics, processes, fluxes, and the canopy effects on the atmosphere, and provides a methodological framework for an integrated analysis of the properties and dynamics of the canopy system.

Based on the conceptual model, a numerical parameterization of the GeCap model was developed by using a nudging approach, aiming to represent the impacts of urban canopies on airflow. The parameterization adds a nudging term as a sink term in the momentum equation and a source term to the turbulent kinetic energy equation to account for building effects. Three-dimensional urban morphology is represented by the weighting function in the nudging term. The developed parameterization is implemented in the mesoscale atmospheric model METRAS and first tested with idealized urban morphology. By using data from an obstacle resolving model as comparison datasets, the parameterization effects were assessed, and the comparison results indicate that GeCap using the extended nudging approach can effectively capture canopy-induced aerodynamic effects, such as the wind-blocking effects and turbulence production by buildings, as well as the vertical characteristics of mean wind speeds and turbulence within urban canopies.

To further represent both aerodynamic and thermodynamic urban canopy effects, a nudging term has been added to the thermodynamic energy equation. The parameterization is then employed with realistic urban morphology for the city of Hamburg. Model results demonstrate that GeCap can accurately simulate the urban heat island effects (UHI) and the negative relationship between wind speeds and the UHI intensity.

This study presents GeCap, a generalized canopy parameterization based on the nudging concept, as a useful tool for representing urban canopy effects in high-resolution atmospheric models. GeCap can be implemented in models with various scales, structural, and computational constraints, yet will accurately represent the most important canopy effects. GeCap's effectiveness and simplicity suggest its applicability for different types of canopies, as well as for various global- and regional-scale weather and climate models.

Zusammenfassung

Städte und Wälder beeinflussen stark die bodennahe atmosphärische Grenzschicht, indem sie die Bewegung der Luft durch Hindernisse (Gebäude und Bäume) beeinflussen, die Oberflächenenergiebilanz modifizieren und die Luftqualität verändern – was direkte Auswirkungen auf das Wetter und das Klima auf verschiedenen Skalen hat. Um die Wechselwirkung zwischen Prozessen in der Hindernisschicht und der darüber befindlichen Atmosphäre besser zu verstehen und den Einfluss der Hindernisschicht auf das Klimasystem sowie auf den Klimawandel zu untersuchen, ist es wichtig, eine Hindernisschicht in numerische atmosphärische Modelle einzuführen. Ziel dieser Arbeit ist es, eine allgemeine Hindernisschicht-Parameterisierung (Generalized canopy parameterization, GeCap) zu entwickeln, um in verschiedenen hochauflösenden atmosphärischen Modellen auf einfache, effiziente und allgemeine Weise die wichtigsten Effekte von Hindernissen auf die Atmosphäre darzustellen.

Zunächst wurde eine umfassende Analyse durchgeführt, um die Effekte von Wäldern (forest canopy effects, FCEs) und Städten (urban canopy effects, UCEs) auf Aerodynamik, Thermodynamik, Hydrologie und Luftqualität zu analysieren. Anschließend wurde eine qualitative Bewertung der FCEs und UCEs im Vergleich zu Grasland durchgeführt, um Ähnlichkeiten zwischen den FCEs und UCEs zu identifizieren. Diese Ähnlichkeiten können durch die Parameterisierung auf einheitliche Weise dargestellt werden. Danach wurde ein konzeptionelles Modell für GeCap entwickelt. Dieses Modell versucht, die Verbindungen zwischen den Eigenschaften, Prozessen, Flüssen und den Effekten von Hindernissen auf die Atmosphäre darzustellen und bietet einen Rahmen für eine integrierte Analyse der Eigenschaften und Dynamik des Hindernissystems.

Auf Basis des konzeptionellen Modells wurde GeCap numerisch realisiert, um die aerodynamischen Auswirkungen von Städten darzustellen. Hierbei wurde ein Nudging-Ansatz verwendet, bei dem ein Nudging-Term als Senken-Term in die Impulsgleichung und ein Quellterm in die turbulente kinetische Energie-Gleichung eingefügt wurden, um die Wirkung von Gebäuden zu berücksichtigen. Die dreidimensionale Stadtmorphologie wird durch die Gewichtungsfunktion im Nudging-Term repräsentiert. Die Parameterisierung wurde in das mesoskalige atmosphärische Modell METRAS implementiert und zunächst mit idealisierten städtischen Morphologien getestet. Mithilfe von Daten eines

hindernissauflösenden Modells als Vergleichsdatensatz wurden die Parameterisierungeffekte evaluiert. Die Vergleiche zeigen, dass GeCap mithilfe des Nudging-Ansatzes effektiv die von Städten verursachten aerodynamischen Effekte wie Windblockadeffekte und die Turbulenzproduktion durch Gebäude sowie die vertikalen Charakteristika der mittleren Windgeschwindigkeiten und der Turbulenz innerhalb urbaner Hindernisschichten erfassen kann. Um sowohl aerodynamische als auch thermodynamische städtische Effekte darzustellen, wurde ein Nudging-Term zu der thermodynamischen Energiegleichung hinzugefügt. Dann wurde die Parameterisierung mit einer realistischen städtischen Morphologie der Stadt Hamburg angewendet. Die Modellergebnisse zeigen, dass GeCap den urbanen Wärmeinsel-Effekt (UHI) und die negative Beziehung zwischen Windgeschwindigkeit und UHI-Intensität effektiv simuliert.

Zusammenfassend stellt diese Studie GeCap, eine allgemeine Hindernisschicht-Parameterisierung basierend auf dem Nudging-Konzept, als ein nützliches Werkzeug zur Berücksichtigung städtischer Effekte in hochauflösenden atmosphärischen Modellen vor. GeCap ist sowohl einfach genug, um in Modellen mit verschiedenen Skalen, Strukturen und Rechenbeschränkungen einfach implementiert zu werden, als auch komplex genug, um die wichtigsten Effekte von Dächern genau darzustellen. Die Effizienz und Einfachheit von GeCap deuten auf ihre Anwendbarkeit für verschiedene Hindernisarten in verschiedenen globalen und regionalen Wetter- und Klimamodellen hin.

Contents

List of Figures

List of Tables

1. Introduction

1.1. Study background

1.1.1. An introduction to urban and forest canopies

A canopy is located within the lowest layer of the atmosphere and encompasses the space from ground level to the top of vertically extended structures such as buildings and trees. It acts as an interface between surface related processes and the atmosphere. Cities and forests are two prominent examples of canopies, namely urban canopies (UCs) and forest canopies (FCs). Cities only cover ~2% of the Earth's surface, but are home to more than half of the world's population (UN, 2019). Forests cover 4.06 billion hectares – about 31% of the total land area, but host more than 75% of the world's life on land (FAO, 2020). While cities are major contributors to climate change, due to human activities being the main source of greenhouse gas (GHG) emissions, forests are considered as key elements for mitigating climate change by carbon uptake and storage (Bonan, 2008; Oke et al., 2017). The report of the Intergovernmental Panel on Climate Change (IPCC) pointed out that climate change has adverse influences on human health, social activities and infrastructure in urban areas, and thus adaptation and mitigation measures must be included into climate policies and urban planning processes (IPCC, 2022). Since cities will experience more intensified extreme heat waves in the future (IPCC, 2022), one of the mitigation measures is to introduce green infrastructure such as green roofs, urban parks, street trees, and urban forests into cities, as they help to reduce human heat stress (Lee et al., 2016a; Lindberg et al., 2016). It is projected that urban canopies are transitioning to a combination of urban canopies and forest canopies – forested urban canopies (FUCs).

1.1.2. Representation of canopy effects in atmospheric models at various scales

Urban, forest, and forested urban canopies influence weather and climate through modifications of the energy exchanges with the atmospehre. Influences are on the water balance,

the carbon cycle, and chemical reactions (Bonan, 2008; Oke et al., 2017). When discussing canopy effects, it is important to consider spatial and temporal "scales" of the relevant processes, especially when representing them in numerical atmospheric models. Figure 1.1 illustrates how canopies are represented in global scale numerical models and provides schematic diagrams of canopy structures and processes at mesoscale, local scale, and microscale. Sharma et al. (2021) highlighted the importance of an accurate representation of urban areas and urban processes at various scales, as well as the feedback across scales in modelling studies.

Most global climate models (GCMs) have grid resolutions of at least 50 km or greater (Haarsma et al., 2016). At these scales, models can be used to study the impact of canopies on the Earth's climate system, and the role of canopies in climate change and recent and future climates. However, only two main canopy effects are usually represented in GCMs: the influence of modification of the surface energy balance on climate change due to large-scale changes in land use and land cover, such as urbanization or deforestation; and the influence of anthropogenic heat release (some climate models) and GHGs emissions from canopies on the global climate (Oleson et al., 2008; McCarthy et al., 2010; Lawrence and Vandecar, 2015; Chen et al., 2016). Due to the coarse resolution and limited computational capabilities, these effects are represented either by implementing simple canopy parameterizations within the land surface scheme of GCMs (a bulk approach or a single layer canopy parameterization) (Oleson et al., 2008; McCarthy et al., 2010; Katzfey et al., 2020) or adjusting surface parameters to the surface cover, such as urban and forest land cover and surface albedo, anthropogenic heat and GHGs release (Chen et al., 2016). Different to GCMs, global numerical weather prediction (NWP) models focus on predicting the evolution of global weather over shorter time scales. A recent study by McNorton et al. (2023) has shown that including a single layer urban canopy parameterization can improve the local prediction of near-surface weather variables.

Mesoscale atmospheric models (MeMs) have a typical grid resolution of ~100 m - 1 km, with domains on the order of 10^2-10^3 km (WMO, 2023). MeMs are used to understand the role of a canopy on local, city-wide or regional climate, and can represent a wide range of canopy effects, such as the air temperature differences between urban and rural areas (the well-known urban heat island phenomenon), wind speed reduction, turbulence production, precipitation interception, and radiation trapping and absorption (Kusaka et al., 2001; Martilli et al., 2002; Hamdi and Masson, 2008; Krayenhoff et al., 2014; Bonan et al., 2018). The physical processes associated with radiative transfer, turbulent mixing, momentum exchanges between the surface and the atmosphere, as well as the modification

of energy and water balance are parameterized in MeMs (e.g. Masson, 2000; Brown, 2000; Kusaka et al., 2001; Martilli et al., 2002; Krayenhoff et al., 2014; Bonan et al., 2018; Wang et al., 2021). MeMs can also be used to study the interaction of canopies with other atmospheric phenomena, such as the effects of urbanization on cloud and precipitation at regional scale (e.g. Shepherd, 2005; Trusilova et al., 2013). Depending on the complexity of the parameterizations, input data should include land cover and land use, 2D or 3D urban and forest canopy morphology, roughness length, and information on thermal and radiative properties.

Microscale atmospheric models (MiMs) resolving obstacles that focus on small areas, such as individual buildings and trees, or small communities, typically have a spatial resolution on scales of $\mathcal{O}(1)$ m and a model domain size of 1-100 km^2 (WMO, 2023). At these spatial scales, obstacles within canopies like trees and buildings are resolved; however, canopy effects such as small vortices generated by buildings need to be parameterized, as they are sub-grid-scale processes and can not be resolved by the grid (WMO, 2023). MiMs can be used to study the role of a canopy on the local environment, such as building and tree shadings, the impact of buildings and trees on local airflow, and cooling effects due to evapotranspiration of trees (e.g. Schlünzen et al., 2003; Salim et al., 2015; Morakinyo et al., 2016; Berardi et al., 2020). High-resolution data on three-dimensional (3D) building and tree morphology, street, canyon, as well as surface material-related thermal and radiative properties, should be provided as input data for the MiMs (WMO, 2023).

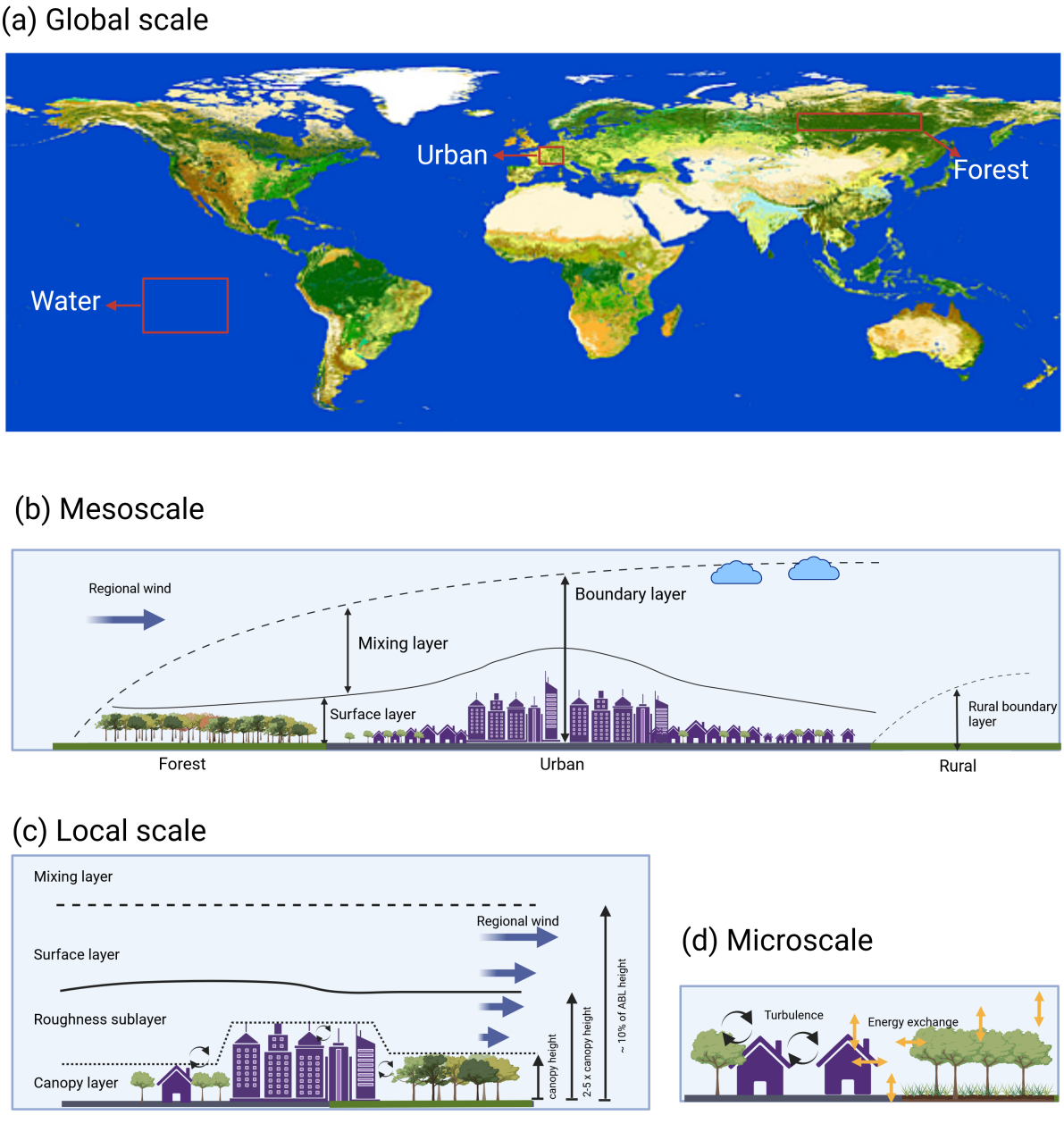

Figure 1.1.: Schematic diagram showing (a) canopies represented in global-scale numerical models by land cover classes such as urban areas and forests; canopy structures and processes at (b) mesoscale; (c) local scale; and (d) microscale within the boundary layer. Blue arrows indicate regional winds, curved black arrows indicate produced turbulence, yellow arrows indicate energy exchange processes. Figure (a) modified after the ESA GLOBCover 2009 Global Land Cover Map (ESA, 2010). Figures (b)-(d) modified after Oke (1997); Barlow (2014); Helbig et al. (2021).

1.2. Key research questions

In the last decades, a large number of canopy parameterizations has been developed, aiming to represent various aerodynamic, thermodynamic, and hydrological processes in atmospheric numerical models (Mills, 1997; Masson, 2000; Brown, 2000; Walko et al., 2000; Ronda et al., 2001; Kusaka et al., 2001; Martilli et al., 2002; Gustafsson et al., 2003; Lee and Park, 2008; Krayenhoff et al., 2014; Bonan et al., 2018; Redon et al., 2020; Wang et al., 2021). The current trend is to increase model complexity and level of detail, which however comes with a few drawbacks. First, there is an increase in computational costs, as more sophisticated and powerful computing systems are needed to solve the equations and can lead to longer run times for simulations. Secondly, there is an increased risk of numerical errors and model uncertainty due to the complexity of the code and data. Thirdly, the more complex a canopy parameterization is, the more input data is required to accurately represent the canopy, which can be difficult to obtain. Lastly, the code becomes more difficult to maintain and debug as it becomes more complex.

The aim of the present thesis is to develop a canopy parameterization that is simple enough to be applicable to different types of mesoscale or global climate models with their various structural, computational and data restrictions, yet complex enough to represent effects of the physical processes known to be relevant in terms of canopy effects. To achieve this objective, the following research questions will be addressed:

Q1: Is it possible to develop a generalized canopy parameterization (GeCap) applicable to forest, urban, and forested urban canopies?

Q2: Can we achieve the wind profiles found within urban areas by using a simple parameterization?

Q3: What are the influences of a simple parameterization on the urban heat island?

Note that the city of Hamburg, Germany, is the focus of the current work for the application tests and evaluation cases, rather than using multiple sites in different climate regimes around the world.

1.3. Structure of the thesis

In the following chapters, I approach the three research questions Q1-Q3 by starting with the conceptualization (**Chapter 2**), then moving to the development of the parameterization (**Chapter 3**), and further exploring the application of the parameterization (**Chapter 4**).

By a "Generalized Canopy parameterization (GeCap)" it is meant that the parameterization is able to represent different types of canopies, and different canopies' effects on the atmosphere in a unified way. The precondition for achieving this is that there are strong similarities between the urban, forest and forested urban canopies. **Chapter 2** investigates these similarities and differences between the three types of canopies, from the perspective of their effects on the aerodynamics, thermodynamics, hydrology, and air quality. Using this information, a conceptual model of GeCap was developed.

Based on the conceptual model constructed in Chapter 2, **Chapter 3** develops a numerical parameterization of GeCap. The parameterization uses a wind nudging approach, and was implemented within the mesoscale model METRAS. A series of simulations with idealized urban morphology for the city Hamburg was carried out to evaluate the parameterization effects, with a particular focus on the representation of building effects on airflows within and above the urban canopy layer.

Chapter 4 further investigates the parameterization effects under different meteorological conditions. In addition to wind nudging, temperature nudging is used to examine how the parameterization represents the thermodynamic effects of urban canopies. Unlike the idealized urban morphology used in the Chapter 3, realistic Hamburg building structures are introduced as input data. Chapter 4 also discusses the possibility of introducing nudging as an efficient parameterization approach into global scale numerical models.

In **Chapter 5**, comprehensive responses are provided for the above research questions posed in Section 1.2. In addition, a general conclusion is drawn, along with limitations of the thesis and suggestions for future work.

2. Conceptual model for a Generalized Canopy parameterization (GeCap)

This chapter has been published as:

Cheng, G. & Schlünzen, K. H.(2023) A conceptual model for a generalized canopy parametrization for atmospheric models. *Quarterly Journal of the Royal Meteorological Society*, 149(751), 494–514. https://doi.org/10.1002/qj.4420

This chapter includes the full manuscript of the published paper. The original title of the paper and small parts of the text have been slightly modified. Layout and numbering of the paper have been adapted to this thesis document. The references and acknowledgements have been combined at the end of this thesis. K. Heinke Schlünzen has contributed to the conceptualization.

Abstract

The forest canopy and the urban canopy are the two vertically most extended canopies and have a great influence on boundary-layer processes. Many studies in the past have analyzed and discussed forest canopy effects (FCEs) and urban canopy effects (UCEs) on aerodynamics, thermodynamics, hydrology, and air quality individually. Few studies have compared them. To better understand to what extent FCEs differ from UCEs, this study carries out a qualitative assessment of FCEs and UCEs in comparison with grass-covered surfaces. In addition, as canopy effects are represented in atmospheric models by employing canopy parametrizations, this study assesses the existing parametrizations with respect to their ability to consider the relevant canopy processes. For parametrizations being globally applicable and for multiple types of forest, urban, and forested urban canopies, it is desirable to treat both forest and urban canopies in models in a unified way. In this context, a conceptual model for a generalized canopy parametrization (GeCap) has been developed based on the assessments of this chapter. It focuses on the interactions between canopy characteristics, processes, and fluxes as they relate to canopy effects. GeCap can serve as a methodological framework for an integrated analysis of properties and dynamics of canopy systems and for the design of forested urban canopy parametrizations.

2.1. Introduction

Forests and cities play important roles in land-atmosphere exchanges of momentum, heat, water vapor, carbon dioxide, and other trace gases (Bonan, 2008; Oke et al., 2017). A better understanding of these exchange processes is important for many environmental applications as well as for weather and climate forecasting. Both forest canopies and urban canopies are not resolved in the atmospheric models with a typical horizontal resolution of 1-10 km. However, their effects on atmospheric processes in the lower planetary boundary layer should be included in the models (WMO, 2023).

To explicitly represent relevant processes and effects of canopies, forest canopy parameterizations and urban canopy parameterizations have been developed for use in atmospheric models. Forest canopy parameterizations (FCPs) have been intensively developed since the 1970s (Deardorff, 1978; Dickinson et al., 1986); urban canopy parameterizations (UCPs) about 20 years later (Mills, 1997; Brown, 2000; Masson, 2000; Kusaka et al., 2001; Martilli et al., 2002). As forest canopies and urban canopies share common features, in

terms of their physical properties and effects on the atmosphere, FCPs and UCPs are in parts similar. For example, both forest and urban canopies reduce wind speed and enhance turbulence intensity just above the canopies (Roth, 2000). This effect is parameterized by using the same approaches, namely roughness-length approach (Mills, 1997; Masson, 2000) or drag-force approach (Yamada, 1982; Brown, 2000; Martilli et al., 2002). In addition, complex radiative processes including radiation absorption, trapping, and shadowing effects are represented in both FCPs and UCPs (Dupont et al., 2004; Hamdi and Masson, 2008; Bonan et al., 2018). Moreover, FCPs and UCPs can be categorized into three types in terms of their representation of the surface: slab parameterization (e.g. Ronda et al., 2001; Alexander et al., 2015), single-layer parameterization (e.g. Walko et al., 2000; Kusaka et al., 2001; Ryu et al., 2011; Lipson et al., 2018), and multi-layer parameterization (e.g. Brown, 2000; Martilli et al., 2002; Hardy et al., 2004; Bonan et al., 2018). However, differences between FCPs and UCPs should not be neglected. For example, FCPs (e.g. Walko et al., 2000; Ronda et al., 2001; Bonan et al., 2018) consider forest-specific photosynthesis processes and uptake of water by plants and roots while UCPs (e.g. Oleson et al., 2008; Wang et al., 2013; Alexander et al., 2015) include urban-specific processes such as the anthropogenic heat emission and surface runoff.

Some urban canopy parameterizations include effects of street trees (Lee and Park, 2008; Krayenhoff et al., 2014; Wang, 2014; Ryu et al., 2016; Lee et al., 2016b; Redon et al., 2020); this type of parameterization is named forested urban canopy parameterization (FUCP). Compared to UCPs, FUCPs more realistically represent the effects of cities with vegetation on the atmosphere, as FUCPs include energetic and hydrological interactive processes between urban vegetation and built-up surfaces (Lee and Park, 2008), thermal and hydrological heterogeneities at the vegetation surfaces, roof, wall, and canyon surfaces (Wang, 2014), and shortwave and longwave radiation exchange between buildings and trees (Krayenhoff et al., 2014). Grimmond et al. (2009) stated that FUCPs better simulate outgoing shortwave radiation, net radiation and the turbulent fluxes than UCPs. However, each existing FUCP has its limits and often neglects some important physical processes. For example, heat and water fluxes of vegetation are not addressed in BEP-Tree by Krayenhoff et al. (2014), and exchange of longwave radiation between street trees and urban fabrics is not considered in the FUCP by Wang (2014).

Despite well-documented research on analyzing the effects of forest canopies and urban canopies, the similarities and differences between them are not fully clear. This chapter aims to fill this gap. We also explore in this study the possibility of developing a conceptual model for a canopy parameterization that sufficiently represents the important processes

of forest, urban and forested urban canopies in any combination and is usable in global scale models. By conceptual model we mean a qualitative model representing the various components, complexities, and interactions of canopy effects with variables relevant for weather and climate (e.g. temperature, humidity). It provides an easily understood system interpretation for the canopy and can be used for the construction of a quantitative model. For developing the conceptual model, the following key questions are addressed:

Q1: To what extent are parameters and processes in forest and urban canopies different from each other and from those above grass?

Q2: Which processes are relevant for a forest, urban, and forested urban canopy and need to be considered in a parameterization?

Q3: Is it possible to develop a generalized parameterization applicable to forest, urban, and forested urban canopies?

The paper is structured as follows: Section 2.2 describes the definition of canopies, canopy-relevant processes, and canopy effects on aerodynamics, thermodynamics, hydrology, and air pollution. Section 2.3 reviews and assesses the existing canopy parameterizations used in previous studies. Section 2.4 introduces the conceptual model for a generalized canopy parameterization (GeCap) and discusses the possibilities of GeCap. Section 2.5 provides conclusions of the study.

2.2. Canopy processes and effects

2.2.1. What is understood by canopy layer

The canopy layer is the lowest layer of the atmosphere and acts as the interface between atmosphere, anthroposphere, hydrosphere, and pedosphere. It extends from the ground level to the top of obstacles, which refer to vertically extended structures, such as buildings and trees (Figure 2.1). Theoretically, also e.g. grass forms a (grass) canopy with a vertical extension of a few centimeters to several tens of centimeters (Aylor et al., 1993; Phillips et al., 2012); effects of these canopies might be sufficiently well described in atmospheric models using a slab approach.

This paper focuses on vertically more extended canopies created by buildings and trees with heights larger than the lowest model level that might be at ˜10 m for a high-resolution atmospheric model. Heights of forest, urban or forested urban canopies are ten meters up to a few hundred meters (Figure 2.1). A forest canopy is generally defined as the assemblage of all foliage, twigs, fine branches, their attending flora and fauna, the air,

and their environment (Nadkarni et al., 2004). An urban canopy is traditionally defined as the combination of buildings and the air volume between them. A forested urban canopy is defined as an urban canopy with vegetation and trees (Lee and Park, 2008).

Oke et al. (2017) and WMO (2023) named the forested urban canopy as the urban canopy, however, the traditional definition of the urban canopy (without vegetation or trees) is used in the present study. Even though the three types of canopy layers differentiate themselves by their definitions and characteristics, they have some similarities, especially in terms of their effects on the atmosphere (Section 2.2.2 and 2.2.3). And this provides a baseline for developing a generalized parameterization for the forest, urban, and forested urban canopies (Section 2.4).

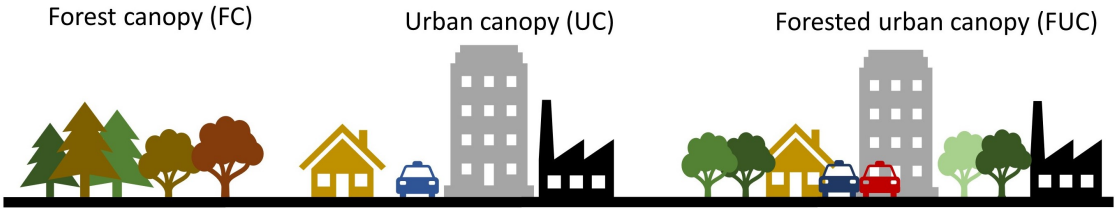

Figure 2.1.: Sketch of a forest canopy, an urban canopy, and a forested urban canopy.

2.2.2. Canopy effects

It is important to consider canopy effects in high-resolution atmospheric models, since the canopy affects exchange processes within and above it, and then influences weather and climate. To better understand how the atmosphere is modified due to the presence of canopies, we compare the forest canopy effects (FCEs) and urban canopy effects (UCEs) to the grassland effects from the perspective of aerodynamics, thermodynamics, hydrology, and air pollution. The differences and similarities are discussed at three vertical levels, namely at ground level, within canopies, and at top of canopies. Please note that for the comparison with grassland we assume the same atmospheric stability and use the same heights above ground and thus compare values within the forest and urban canopy with above grass.

Effects at different levels might be considered in single-layer and multi-layer canopy parameterizations. The main difference between these two types of parameterizations lies in the representation of the vertical structure of canopies (Masson, 2006). While single-layer canopy parameterizations treat an urban canopy as a single layer, multi-layer

canopy parameterizations divide an urban canopy into multiple layers (Ryu et al., 2011). In contrast, slab parameterizations in general aim at representing an integral effect, and are often using the information at the top of canopies above the displacement height. If the parameter/process is not applicable there, the surface values are used.

Canopies have multiple surfaces, such as leaves, stems, and branches in forest canopies; walls, roofs, windows, and roads in urban canopies. Each surface has a separate effect on exchange processes with the atmosphere and thereby separately influences the aerodynamics, thermodynamics, hydrological, and pollutant-related processes. In this section, these processes are not discussed per obstacle, but the overall canopy processes are presented as we aim at parametrizing them in global-scale models that have the typical resolutions of ˜1 km and do not resolve obstacles explicitly.

As morphology and phenology play important roles in forest effects on the atmosphere, here we only consider continuous forest canopies during the growing season. For this chapter, the forested urban canopy effects are not discussed individually, because they are considered as a combination of the forest canopy effects and urban canopy effects.

The results of the comparison are summarized in Table 2.1 with a detailed discussion of each element in the following subsections. Table 2.1 helps not only to understand to what extent forest canopies differ from urban canopies, but it also helps to determine what processes are relevant and should be considered in forest, urban as well as forested urban canopy modelling when compared to lower obstacles as grassland modelling (Section 2.2.3).

Table 2.1.: Summary of forest canopy effects (FCEs) and urban canopy effects (UCEs) on aerodynamics, thermodynamics, hydrology, and air quality. FCEs and UCEs are compared to grassland effects at ground level, within the canopy, and at the top of the canopy. Increase (+), decrease (-), little change (./.), or increases and decreases (±) can occur for a parameter/variable/process. Note that the assessment is done with values at the same heights, i.e. a value for a parameter/variable/process above ground but within the canopy is compared with a value at the same height above grassland and thus in fact in the air. NA denotes not applicable. # refers to the number of the input parameters (PA-PC) and the variables/processes (P1-P16) to be considered in a canopy parameterization (Section 2.2.3). Yellow cells denote a forest canopy and an urban canopy share the same effect at the same vertical level.

Canopy effect	**P#**	**Parameter/Variable/Process**	**FC compared to GL**			**UC compared to GL**		
			at the ground	**within FC**	**top of FC**	**at the ground**	**within UC**	**top of UC**
Aero dynamics	PA	Roughness length	NA	NA	+	NA	NA	+
	P1	Wind speed	-	-	-	-	-	-
	P2	Turbulence intensity	-	-	+	-	-	+
Thermo dynamics	PB	Albedo	-	-	-	-	-	-
	PC	Heat storage	+	+	+	±	+	+
	P3	Sensible heat	+	+	+	+	+	+
	P3	Latent heat	±	±	±	-	-	-
	P4	Incoming / Outgoing shortwave radiation	-	-	./.	-	-	-
	P4	Reflection of shortwave radiation	-	+	+	-	+	+
	P4	Shadowing	+	+	./.	+	+	./.
	P5	Incoming longwave radiation	+	+	./.	+	+	+

Canopy effect	P#	Parameter/Variable/Process	FC compared to GL			UC compared to GL		
			at the ground	within FC	top of FC	at the ground	within UC	top of UC
	P5	Outgoing longwave radiation	+	+	+	+	+	+
	P6	Anthropogenic heat emissions	NA	NA	NA	+	+	+
Hydrology	P7	Precipitation including interception	-	-	+	-	-	±
	P8	Evapotranspiration	±	±	±	-	-	-
	P8	Photosynthesis	+	+	+	NA	NA	NA
	P9	Surface runoff	-	NA	NA	+	+	+
	P10	Infiltration, soil water storage	+	NA	NA	-	NA	NA
	P11	Anthropogenic water & piped water	NA	NA	NA	+	+	+
Air quality	P12	Emissions of PM, NO_x, SO_2, CO	./.	./.	./.	+	+	+
	P13	Emission of BVOCs and pollen	+	+	+	NA	NA	NA
	P14	O_3 formation	±	±	±	±	±	±
	P15	AVOCs emissions	NA	NA	NA	+	+	+
	P16	Chemical reactions	±	±	±	±	±	±
	P17	Pollutant uptake	./.	+	+	./.	+	+

Canopy effects on wind and turbulence

The aerodynamic effects of forest canopies and urban canopies have been of interest to forest climate and urban climate science for a long time. It is commonly accepted that there are similarities between forest canopies and urban canopies, in terms of their effects on the mean and turbulent airflows. When air flows through forests or cities, a certain proportion of momentum is absorbed leading to a reduction of wind speeds within and above canopies (Yamada (1982); Oke (1988b); P1 in Table 2.1). For neutral stratification, mean wind speed profiles above both types of canopies are expressed in the integral approach as follows (Oke, 1987).

$$U(z) = \frac{u_*}{k} \ln\left(\frac{z-d}{z_0}\right) \tag{2.2.1}$$

where $U(z)$ is the horizontal wind velocity at height z, u_* is the friction velocity, k is von Karman constant (˜0.4), z is the height above the ground, z_0 is the aerodynamic roughness length, and d is the zero-plane displacement height (including z_0) at which the wind speed is 0 m/s. z_0 depends on roughness geometry, and forests and cities have similar values (˜0.7 m) that are much greater than for the open ground with small obstacles such as grass (˜0.1 m) (Stull (1988); PA in Table 2.1). According to Cleugh and Grimmond (2012), the obstacle influences can extend to about 2 to 3 times above the heights of the buildings, varying with the building dimensions and spacing.

Assuming the same stability, the turbulence intensity within the forest and urban canopies are lower compared to the turbulence above grassland due to the lower wind speed within canopies (P2 in Table 2.1). For instance, wind tunnel experiments by Kastner-Klein and Rotach (2004) showed that turbulent kinetic energy below the roof level in the modelled urban areas is lower than in non-urban areas. If the differences in stability are considered, e.g. the higher vertical mixing at height due to urban heat island effects (Bohnenstengel et al., 2014), the turbulence might be larger in the urban canopy than at the same height above ground over grass. However, in our comparison, we assume the stability is the same. Above canopies, the turbulence intensity depends on the surface roughness, the larger the value of roughness length (z_0) the greater is the turbulence intensity (Roth, 2000). As both forest and urban canopies have larger values of z_0, turbulence above canopies is enhanced. Surface measurements by Bowne and Ball (1970) showed that turbulence intensity above the city of Fort Wayne, Indiana, was 30% to 50% higher at a height of 60 m than that at a similar level over the surrounding rural area. Cleugh and Grimmond (2012) pointed out that under neutral stratification turbu-

lent kinetic energy for forest canopies and urban canopies reaches its maximum value at similar heights just above the top of canopies and the flow forms a highly turbulent shear layer (P2 in Table 2.1). It should be noted that for both forest and urban canopies, wind profiles and turbulence characteristics within and above canopies are strongly influenced by atmospheric stability and canopy morphology, such as building and vegetation structure, foliage density, as well as density and shapes of buildings (Roth, 2000; Zeng and Takahashi, 2000; Coceal and Belcher, 2005; Cleugh and Grimmond, 2012; Moon et al., 2019).

Canopy effects on energy balance

We discuss the thermodynamic effects of canopies using the integral canopy energy budget, which can be written as follows:

$$Q_A + Q^* = Q_S + Q_L + Q_G, \tag{2.2.2a}$$

$$Q^* = R_{S\downarrow} + R_{S\uparrow} + R_{L\downarrow} + R_{L\uparrow}, \tag{2.2.2b}$$

where Q_A is the anthropogenic heat flux, Q^* is the net all-wave radiation, Q_S is the sensible heat flux, Q_L is the latent heat flux, and Q_G is the net heat storage in canopies. Q^* is the sum of incoming ($R_{S\downarrow}$) and outgoing ($R_{S\uparrow}$) shortwave radiation, as well as incoming ($R_{L\uparrow}$) and outgoing ($R_{L\uparrow}$) longwave radiation, as given in Equation 2.2.2b.

The incoming shortwave radiation ($R_{S\downarrow}$) is the sum of the direct beam and diffuse radiation (P4 in Table 2.1). Forests have little impact on the $R_{S\downarrow}$ reaching the top of forest canopies (Baldocchi et al., 2004). As $R_{S\downarrow}$ penetrates through the forest canopies, a portion of the radiation is absorbed by canopy elements (tree crown, trunk, stem, etc.), the $R_{S\downarrow}$ within canopies and arriving at the forest floor is thus decreased (Ross, 1981; Baldocchi et al., 2000). The absorption and transmittance of $R_{S\downarrow}$ depend on the canopy structure, in terms of the size and location of the canopy gaps, as well as canopy density (Knyazikhin et al., 1998; Hardy et al., 2004). Higher canopy density results in a stronger reduction of $R_{S\downarrow}$.

For urban canopies, the $R_{S\downarrow}$ reaching the canopy top can decrease if the urban atmosphere contains high levels of particles and radiation is scattered by air pollutants (Cleugh and Grimmond, 2012). Besides, cities have impacts on boundary-layer clouds through enhanced convergence due to increased surface roughness and the release of aerosols as cloud

condensation nuclei resources (Shepherd, 2005). With increasing sky cloudiness, $R_{S\downarrow}$ declines (Liu and Jordan, 1960). The amount of $R_{S\downarrow}$ reaching the city ground is highly dependent on canopy architecture and structure, as the $R_{S\downarrow}$ within canopies is absorbed and intercepted by surfaces of canopy obstacles (Oke et al., 2017).

A portion of the incoming shortwave radiation is reflected by canopy elements (P4 in Table 2.1), and this loss depends on the albedo of canopy surfaces (PB in Table 2.1). Since only averaged canopy effects are considered in this section, a single albedo value for each canopy surface is not discussed. If canopies are treated as slab layers, the albedo of forest canopies (0.13-0.20) and urban canopies (0.14) is lower than that of grasslands (0.16-0.26) (Oke et al., 2017), thus solar radiation reflected by forests and by cities are less than grasslands (von Randow et al., 2004; Teuling et al., 2010; Cleugh and Grimmond, 2012). However, if we compare the reflection of shortwave radiation for both canopies with grassland at the same height above ground, it is higher within canopies and at the top of canopy layers than that for grassland, since at the same height above ground the air above grass is close to non-reflective, while forest and urban canopies have multiple reflecting surfaces. The multiple reflections and shades within the canopy result in 3D radiative fluxes. Note that the reflection of shortwave radiation at obstacles' surfaces is not the same as the outgoing shortwave radiation ($R_{S\uparrow}$). The $R_{S\uparrow}$ within and over canopies is lower compared to grasslands, because of the lower incoming shortwave radiation ($R_{S\downarrow}$) and stronger absorption by obstacles.

The incoming longwave radiation ($R_{L\downarrow}$) above canopies is emitted from the atmosphere. Observation studies show that forests have little impact on the change of $R_{L\downarrow}$ over forest canopies (Baldocchi et al. (2004); von Randow et al. (2004); P5 in Table 2.1). However, $R_{L\downarrow}$ above urban canopies can be enhanced due to high levels of greenhouse gas concentrations and aerosol emissions, elevated temperature and humidity levels (Cleugh and Grimmond, 2012; Wang et al., 2015), as well as higher cloudiness (Kotthaus and Grimmond, 2014). The $R_{L\downarrow}$ beneath canopies can be divided into two parts: the $R_{L\downarrow}$ emitted by canopy elements and the $R_{L\downarrow}$ passing through the canopies. Both of them are influenced by the canopy characteristics, such as building height heterogeneity, sky view factor, and leaf area index (LAI) or building coverage index (BCI) (Blankenstein and Kuttler, 2004; Yang and Li, 2015). Compared to open areas, both forest and urban canopies increase the $R_{L\downarrow}$ reaching the underlying surface considering the radiation from obstacles (Essery et al., 2008; Blankenstein and Kuttler, 2004). Blankenstein and Kuttler (2004) measured $R_{L\downarrow}$ by car at a height of 3.3 m above ground level through the city of Krefeld, Germany, and demonstrated that $R_{L\downarrow}$ increases with a decreased sky view

factor, suggesting that more $R_{L\downarrow}$ is emitted by horizon obstructions. For the $R_{L\downarrow}$ passing through the canopies, a numerical model study by Yang and Li (2015) has shown that more radiation is absorbed as building heights become more heterogeneous.

For both forest and urban canopies, the outgoing longwave radiation ($R_{L\uparrow}$) is generally enhanced relative to open areas due to the existence of the canopies (Hardy et al. (2004); Lawler and Link (2011); P5 in Table 2.1). And as LAI or BCI increases, the portion of longwave radiation from canopy elements increases. As $R_{L\uparrow}$ can be computed based on the Stefan–Boltzmann law, which depends on the emissivity of the canopy and the canopy temperature, the diurnal cycle of $R_{L\uparrow}$ should be calculated dependent on respective temperatures, e.g. of walls and roofs.

Sensible heat flux (Q_S) refers to heat transfer from canopies to the surrounding atmosphere (P3 in Table 2.1), thus Q_S mainly depends on the temperature difference between canopy surfaces and air, and wind speed. A comparison study of radiation over a Scots pine forest and an adjacent grassland in southwest Germany by Holst and Mayer (2006) showed that Q_S over forests exhibited stronger diurnal patterns than over grassland throughout the whole year, and the peak difference occurred in July after midday. Another study measuring fluxes over forests and grasslands at all European FLUXNET sites revealed that under high temperature and high incoming shortwave radiation (such as under heatwave conditions), forests emit more sensible heat than grassland (Teuling et al., 2010), which results from a different response of stomatal opening to radiation and atmospheric conditions (Teuling et al., 2010; van Heerwaarden and Teuling, 2014). The Q_S over and within cities is generally higher than that for grasslands due to higher surface temperatures of obstacles than surroundings. Li et al. (2015) pointed out that Q_S could far exceed that over non-urban areas, especially during heatwave days.

Latent heat flux (Q_L) refers to the transfer of heat from canopies to the surrounding air by evaporation of water on the obstacle surfaces (P3 in Table 2.1), thus Q_L is related to the evaporation process and moisture transport. Water supply plays an important role in the variation of Q_L for forests and grasslands. Studies indicate that Q_L over forests can be lower than that over grasslands under sufficient soil moisture conditions (Wicke and Bernhofer, 1996; Holst and Mayer, 2006), the reverse might occur for low soil water supply (von Randow et al., 2004). Besides, atmospheric conditions, plant functional-type, rooting depth of the vegetation, stomatal control as well as topography also have impacts on the temporal evolution of Q_L (Baldocchi et al., 2004; Holst and Mayer, 2006; Teuling et al., 2010; van Heerwaarden and Teuling, 2014). Q_L in cities is generally low because there is less vegetation and more impervious surfaces, which results in low moisture availability

and reduced evaporative cooling (Kotthaus and Grimmond, 2014).

Anthropogenic heat flux (Q_A) is specific for urban canopies, as it results from human activities including heat release of industrial plants, building heating, ventilation and air conditioning (HVAC systems), vehicle exhausts, etc. (P6 in Table 2.1). According to Sailor (2013), when including Q_A as an additional source term in the urban canopy surface energy balance, the vertical distribution of Q_A emission should be considered. At pedestrian level, heat emissions are from vehicles; within canopies, emissions from buildings occur throughout the vertical height of the building; at top of canopies, a substantial portion of Q_A is from the mechanical HVAC equipment, which is usually located at roof levels (Sailor, 2013). The value of Q_A depends on local climate and population density. In general, Q_A in winter is greater than that in summer and the greater population density at city scales results in substantially larger values for Q_A (Sailor et al., 2015).

Heat storage flux (Q_G) is a significant component of the surface energy balance for forests and urban areas (Roberts et al., 2006; Haverd et al., 2007). Compared to short grasslands, tall forests have higher heat storage, owing to larger volumes of air and biomass within the canopy (Holst and Mayer (2006); Haverd et al. (2007); PC in Table 2.1). Cities can better store heat than grassland because under urbanization natural materials (e.g. soils and vegetation) are replaced with construction materials (e.g. concrete, asphalt, brick) (Oke et al., 2017), which offer higher heat capacity. In addition, more heat storage is created due to the 3D building structures (Oke et al., 2017), and as a result, more heat is retained in buildings during the daytime (Grimmond and Oke, 1999; Roberts et al., 2006). However, it should be noted that the Q_G at the ground level in cities can be influenced by the shadow effects of tall buildings (P4 in Table 2.1), as buildings prevent solar radiation reaching the ground and thus reduce the heat storage underneath (Vuckovic et al., 2019).

Canopy effects on water balance

Canopy effects on water balance are discussed using canopy surfaces water budget, which can be written as (Anderson et al., 1976; Grimmond and Oke, 1991):

$$W_P + W_I + W_A = W_E + W_R + \Delta W_S \tag{2.2.3}$$

where W_P is precipitation, W_I is piped water supply, W_A is water released due to anthropogenic activities, W_E is evapotranspiration, W_R is surface runoff, and ΔW_S is the change in water storage in the soil and ground water aquifers for the period of interest.

Forests play important roles in regulating precipitation patterns over land (Ellison et al. (2017); P7 in Table 2.1). Modelling studies suggest that tropical forests increase precipitation compared with pastureland (Bonan, 2008). Meier et al. (2021) who used an observation-based continental-scale statistical model found that converting agricultural land to forest can increase summer precipitation by 7.6% on average over Europe. Moreover, a study by Hoek van Dijke et al. (2022) found that increasing large-scale tree-cover enhances precipitation indirectly, which combined with directly enhanced evaporation will shift regional water availability.

For cities precipitation connections are complex. Comprehensive reviews on urban impacts on precipitation indicate that both increase and decrease in precipitation caused by urbanization are possible (Han et al., 2014; Liu and Niyogi, 2019). The urban rainfall modification can be related to urban heat island intensity, large surface roughness, and aerosols (Han et al., 2014; Liu and Niyogi, 2019). For instance, precipitation downwind as well as over cities can be enhanced due to urban head island-induced updrafts (Han et al., 2014; Liu and Niyogi, 2019). Aerosols influence the development of clouds and precipitation as it serves as condensation nuclei for the formation of cloud droplets and atmospheric ice particles (Han et al., 2014). By using a cloud-resolving mesoscale model, van den Heever and Cotton (2007) found that under low background aerosol concentrations, increased urban aerosols can enhance convective storms and associated precipitation. However, according to Ntelekos et al. (2009) whether the increasing aerosol concentration can enhance the precipitation in intense convective storms depends on relative humidity, convective available potential energy, and wind shear. In addition, convective systems connected to precipitation can be disrupted by the larger urban surface roughness (Han et al., 2014).

Canopy interception of precipitation is an important component of the water balance (Xiao and McPherson, 2002; Miralles et al., 2010). Precipitation within forest canopies is partitioned into three fractions: interception (precipitation remains on trees), stemflow (precipitation flows to the ground via trunks or stems), and throughfall (precipitation that may or may not contact the canopy and falls to the ground between the various components of the trees) (Anderson et al., 1976). Adane et al. (2018) pointed out that rainfall interception rate in dense pine forests was 70% greater than in grassland. Therefore, precipitation reaching the forest floor is strongly reduced relative to grasslands (P7 in Table 2.1). Similarly, rainfall within urban canopies can be intercepted by canopy surfaces, such as roofs and walls of buildings, awnings, balconies, etc. This effect on precipitation patterns at the ground might be less relevant than influences of urban structures on the boundary layer clouds as found by Ferner et al. (2022). Nonetheless, the rainfall intercep-

tion by high-rise buildings should be additionally considered in urban hydrological studies for megacities as mentioned by Yoo et al. (2021). Cho et al. (2020) proposed an empirical equation for estimating the amount of rainfall intercepted by a building, which depends on the rainfall intensity observed at the ground, the width and the height of the building wall, as well as the wind speed.

The evapotranspiration process (W_E) consists of evaporation from soil and plant surfaces and transpiration of water by trees (P8 in Table 2.1). Forests typically have increased evapotranspiration rates compared to grassland (Bonan, 2008) due to deeper roots (Schenk and Jackson, 2003) and higher leaf area index (Henderson-Sellers, 1993). However, Breil et al. (2021) demonstrated that whether forests have higher evapotranspiration rates than grasslands actually depends on the canopy resistance and the saturation deficit between the plant and the atmosphere, which relates to the surface temperature and the input of net radiation. Hence, both increase and decrease in W_E of forests relative to grasslands are possible. Evapotranspiration in cities is lower compared to grassland, as natural surfaces are replaced by plenty of artificial surfaces (roads, pavements, and buildings) (Sterling et al., 2013; Oke et al., 2017). Sterling et al. (2013) analyzed the impact of the global land cover change on the terrestrial water cycle using the GIS method and found that the conversion from grassland to urban landscape leads to a decrease in evapotranspiration by 14% globally.

Surface runoff (W_R) refers to water that moves overland and occurs when there is more water than can be absorbed by the surfaces (P9 in Table 2.1). Runoff in forests usually occurs at ground level. It is well agreed that forests reduce surface runoff rates (Anderson et al., 1976; Alaoui et al., 2011). Cities enhance runoff and reduce infiltration, due to the replacement of natural land cover with impervious cover like roads, bridges and parking lots (Boyd et al., 1994; Armson et al., 2013). Apart from these runoff processes occurring on the ground, runoff on building facades and rooftops also occurs in cities.

Forest soils have higher values of water storage capacity compared to grassland (Alaoui et al. (2011); P10 in Table 2.1). Forest soil structure is characterized by higher values of hydraulic conductivity and the structural porosity, as well as larger water uptake by tree roots, and these characteristics enhance infiltration processes (Alaoui et al., 2011). For urban canopies, horizontal exchange of soil water is impeded by urban infrastructure (e.g. basements, pipes and tunnels), while vertically, infiltration processes for water to enter the soil is declined due to the increased impervious cover (Oke et al., 2017).

Piped water supply (W_I) and water released due to anthropogenic activities (W_A) are very important for the urban canopy surface water balance (Grimmond and Oke, 1991).

Watering of plants or irrigation is used in agricultural areas, as mentioned by Siebert et al. (2007) that approximately 40% of the total area used for agricultural production worldwide is irrigated, however, not much over grasslands and forests. Therefore, NA is added for P11 in Table 2.1.

Canopy effects on air pollution

Air pollution can have influences on human health and well-being, ecosystem health, and climate. We discuss the emissions of eight air pollutants due to the presence of forest and urban canopies: particulate matter (PM), ozone (O_3), nitrogen oxides (NO_x), sulphur dioxide (SO_2), carbon monoxide (CO), anthropogenic volatile organic compounds (AVOCs), biogenic volatile organic compounds (BVOCs) and pollen. These air pollutants are selected because they are the most common pollutants investigated in previous air quality measuring and modeling studies and are most relevant to human and ecosystem health (Seinfeld, 1989; Mayer, 1999; Fenger, 1999; He et al., 2002; D'Amato et al., 2010; Nowak et al., 2014; Eisenman et al., 2019).

Trees in forests can have positive and negative effects on air quality. On the one hand, trees remove gaseous air pollutants (e.g., O_3, SO_2, and NO_x) through uptake via leaf stomata, and capture PM from the atmosphere through interception and resuspension processes on plant surfaces (Nowak et al. (2006, 2014); P17 in Table 2.1). On the other hand, trees emit pollen and BVOCs (P13 in Table 2.1), which contribute to PM2.5 and O_3 formation and reduce air quality (Chameides et al., 1988; Nowak et al., 2014). O_3 is not directly emitted from trees but is formed in the atmosphere when NO_x and BVOCs react in the presence of sunlight. A feedback loop of O_3 production in forests works as follows. BVOCs released by trees result in high O_3 levels, which inhibits tree growth and survival, and further prompts the release of BVOCs and enables more O_3 production (Eisenman et al., 2019). Thus, the influence of trees on O_3 concentrations depends on whether direct O_3 uptake outweighs indirect O_3 production by trees through the emission of BVOCs (Fitzky et al. (2019); Eisenman et al. (2019); P14 in Table 2.1).

Air quality is one of the major concerns in cities. Many cities across the world suffer from serious air pollution caused by anthropogenic activities, including industry, trade, power plants, vehicle traffic, etc. (Mayer, 1999). Urban air pollutants mainly include PM, O_3, NO_x, SO_2, CO, and AVOCs. Five of these pollutants (PM, NO_x, SO_2, CO, AVOCs) are emitted from a variety of direct sources (P12 and P15 in Table 2.1), whereas O_3 is not directly emitted. O_3 in cities is formed when NO_x reacts with AVOCs in the presence of sunlight, but at the same time, O_3 can be degraded by NO. Observational studies show

that O_3 concentrations are higher at suburban or rural sites than at urban sites, as heavy traffic in cities causes higher NO concentrations, which help destroy photochemically produced ozone, and further results in lower O_3 concentrations compared to suburban areas (Klumpp et al. (2006); P14 in Table 2.1). As AVOCs concentrations are higher in cities than in grasslands, a similar photochemical reaction can take place as for BVOCs from forests, thus, an increase of O_3 formation in cities is also possible. Moreover, similar to forests, air pollutant uptakes can also occur in cities (P17 in Table 2.1), such as dry deposition of NO_x and SO_2 gaseous pollutants on building surfaces (Haneef et al., 1992; Grøntoft and Raychaudhuri, 2004).

Vertical and horizontal distribution of air pollutants within and above canopies are highly dependent on meteorological factors including atmospheric stability, wind speed and direction, surface friction, etc. (Baumbach and Vogt, 2003; Velasco et al., 2008). For instance, Baumbach and Vogt (2003) reported that a surface-based temperature inversion limited the vertical dispersion of ozone and emitted pollutants were kept beneath this inversion. Cichowicz et al. (2017) found that dispersion of atmospheric air pollution in summer and winter time, which have different meteorological patterns, were different. Air pollution was reduced during the summer season with high temperature and low wind speed and humidity; the opposite situation occurred in winter time (Cichowicz et al., 2017). Moreover, canopy structures such as canyon configurations, roof shapes, distribution of trees also play important roles in the dispersion of air pollutants (Oke, 1988a; Yazid et al., 2014). In addition, all chemical reactions that include reactions with gas phase, gas to particle, particle reactions, and photochemical reactions are relevant and need to be considered in forest and urban canopies (P16 in Table 2.1).

2.2.3. Relevant canopy processes for a forested urban canopy

The parameters and processes that are relevant for a forest canopy and an urban canopy are also relevant for a forested urban canopy. As shown in Table 2.1, there are three important parameters, namely roughness length (PA), albedo (PB) and heat storage (PC). The relevant processes are P1, P2 (aerodynamic processes); P3-P6 (thermodynamic processes, as illustrated in Figure 2.2); P7-P11 (hydrological processes, as illustrated in Figure 2.3); and P12-P17 (processes related to air quality). Note that P1-P11 are usually considered in a parameterization for forested urban canopies, while P12-P17 are usually represented in emission models (Section 2.3.2).

We found that there are similarities and differences between forest canopy effects and

urban canopy effects (Table 2.1). On the one side, forest canopies and urban canopies have the same following effects on the atmosphere:

- P1 wind speed reductions at the three vertical levels (at the ground, within canopies, and at the top of canopies)
- P2 reduced turbulence intensity within canopies and enhanced turbulence intensity at the top of canopies, if the same stability is assumed;
- P3 enhanced sensible heat flux at the three vertical levels;
- P4 enhanced absorption and thus reduced incoming shortwave radiation by the ground and obstacles within canopies also resulting in reduced outgoing shortwave radiation;
- P4 enhanced reflection of shortwave radiation by the ground and obstacles' surfaces within and at the top of canopies;
- P4 shadowing induced by obstacles;
- P5 enhanced absorption and emission of the longwave radiation by obstacles within canopies;
- P7 enhanced precipitation interception induced by obstacles within canopies leading to reduced precipitation at the ground;
- P17 enhanced pollutant uptakes within canopies and at the top of canopies;
- PA increased roughness length;
- PB reduced albedo;

On the other side, the following effects induced by forest and urban canopies go in opposite directions, and they require a more detailed consideration if represented for a forested urban canopy.

- P9 surface runoff: reduced in forest canopies but increased in urban canopies;
- P10 infiltration and soil water storage: increased in forest canopies but reduced in urban canopies;

In addition, anthropogenic heat (P6) and anthropogenic water (P11) as well as AVOC emissions (P15) only occur in urban canopies, while photosynthesis (P8) and BVOC emissions (P13) are typical forest-related processes, but all should be included in a forested urban canopy parameterization.

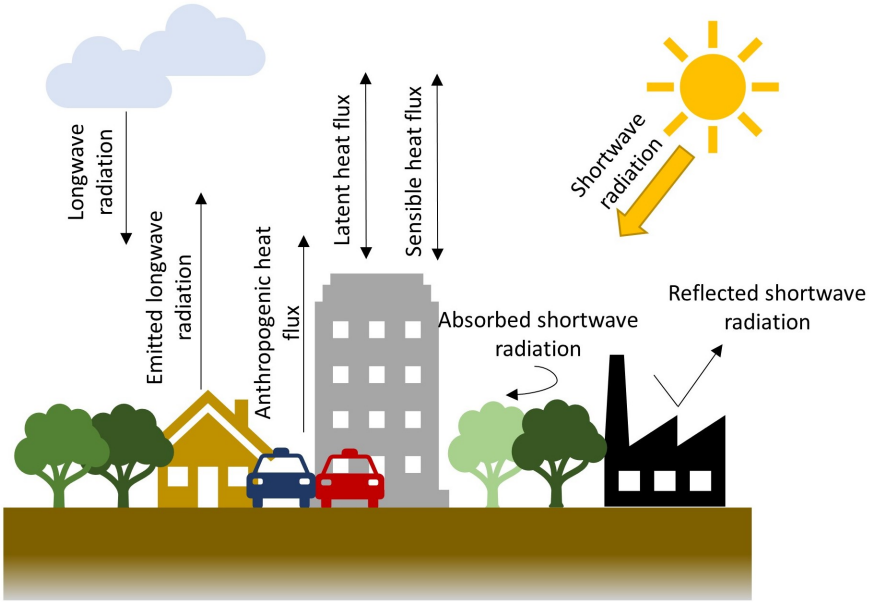

Figure 2.2.: Processes relevant in the surface energy balance of a forested urban canopy that all may occur in one model grid cell.

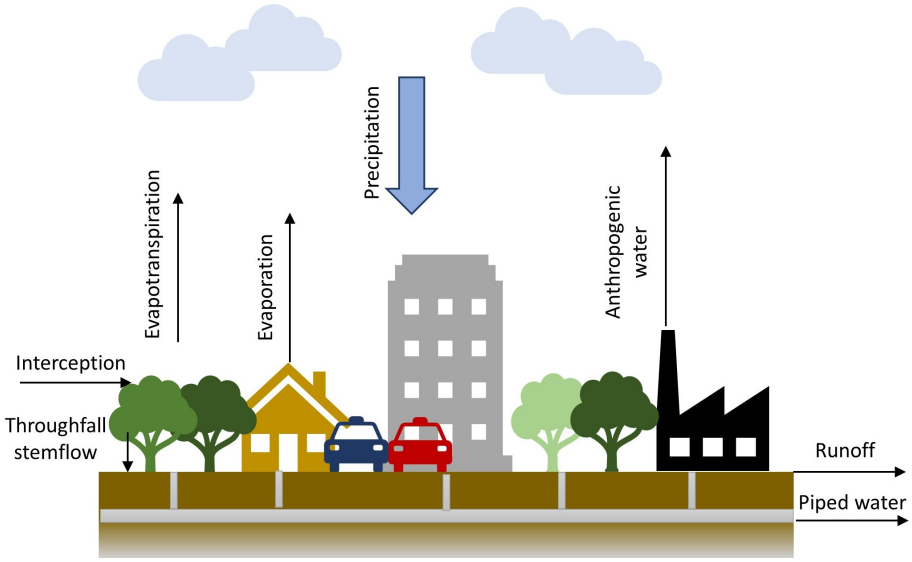

Figure 2.3.: Same as Figure 2.3 but for the water balance.

2.3. Analyses of canopy parameterizations

The canopy processes mentioned in Section 2.2.3 cannot be resolved explicitly in the atmospheric models with a typical horizontal resolution of ˜1 km, and thus they need

to be parameterized. In the past five decades, a wide range of canopy parameterizations has been developed. We analyzed 28 canopy parameterizations including eight forest canopy parameterizations (FCPs), sixteen urban canopy parameterizations (UCPs), and four forested urban canopy parameterizations (FUCPs) (Table 2.2). For each, an acronym of the parameterization name is given that is used hereafter to describe it.

As mentioned in the introduction, canopy parameterizations can be categorized into three types in terms of their representation of the surface: slab parameterization (SB), single-layer parameterization (SL), and multi-layer parameterization (ML).

Slab parameterization is the most traditional and simple method among the three approaches. It treats forest or urban areas as a flat surface and does not consider canopy geometry. Surface physical properties such as roughness length, albedo, thermal conductivity represent the characteristics of the whole forests or urban areas.

Single-layer urban canopy parameterizations (e.g. Mills, 1997; Masson, 2000; Kusaka et al., 2001) were firstly developed based on single-layer forest canopy parameterizations (Deardorff, 1978; Dickinson et al., 1986; Sellers et al., 1986; Walko et al., 2000). SL has one atmospheric layer in the canopy and calculates meteorological variables and fluxes on several surfaces of canopy obstacles differently. Compared to SB, geometry is more realistic in a SL, especially in terms of energy and momentum transfer between different surfaces and the atmosphere (Kusaka et al., 2001). Thus, SL simulates successfully some features of urban canopies such as UHI, radiative trapping, and turbulent exchange (Masson, 2000; Kusaka et al., 2001).

Multi-layer parameterizations (e.g. Martilli et al., 2002; Brown, 2000; Otte et al., 2004; Kanda et al., 2005; Bonan et al., 2018) calculate variables and fluxes at several vertical layers within the canopy. Even though SL can already parameterize shadowing, reflections, and trapping of the radiation (e.g. Kusaka et al., 2001), these radiation interactions are simplified (Masson, 2006). ML better represents the aerodynamic and thermodynamic processes occurring within the urban canyon (Garuma, 2018). However, because ML has higher resolution than SB and SL approaches, ML is computationally more demanding. For both urban and forest canopies, ML parameterizations need as input the vertical distribution of obstacle structures.

Table 2.2.: Summary of the canopy parameterizations. Types, publications, names, and acronyms are listed. Table is divided into three blocks based on the parameterization type, namely forest canopy parameterization (FCP), urban canopy parameterization (UCP), and forested urban canopy parameterization (FUCP). Each block in chronological order.

Type	**Reference**	**parameterization**	**acronyms**
FCP	Deardorff (1978)	Single layer vegetation parameterization	SLVP
FCP	Yamada (1982)	Forest canopy model	FCM
FCP	Dickinson et al. (1986)	Biosphere-Atmosphere Transfer Scheme	BATS
FCP	Sellers et al. (1996)	Simple Biosphere Model 2	SiB2
FCP	Walko et al. (2000)	The Land Ecosystem–Atmosphere Feedback model	LEAF-2
FCP	Ronda et al. (2001)	Surface Energy Budget for Low Vegetation	SEBLV
FCP	Gustafsson et al. (2003)	VB95, Tiled ECMWF Surface Scheme for Exchange processes over Land	VB95, TESSEL
FCP	Bonan et al. (2018)	Community Land Model multilayer canopy model	CLM-ml
UCP	Mills (1997)	Urban Canopy Layer Model	UCLM
UCP	Masson (2000)	Town Energy Balance	TEB
UCP	Brown (2000)	Urban Parameterization	UP
UCP	Kusaka et al. (2001)	Single-layer Urban Canopy Model	SLUCM
UCP	Martilli et al. (2002)	Building Effect parametrization	BEP
UCP	Dupont et al. (2004)	Soil Model for Submesoscales, urbanized version	DA-SM2U
UCP	Otte et al. (2004)	Urban Canopy Parameterization	UCPM

Type	**Reference**	**parameterization**	**acronyms**
UCP	Kanda et al. (2005)	Simple urban energy balance model for mesoscale simulations	SUMM
UCP	Chin et al. (2005)	Urban Parameterization 05	UP05
UCP	Hamdi and Masson (2008)	Town Energy Balance 08	TEB08
UCP	Oleson et al. (2008)	Community Land Model – Urban	CLMU
UCP	Ryu et al. (2011)	New Single-Layer Urban Canopy Model	NSLUCM
UCP	Salamanca et al. (2011)	Building Effect Parameterization - Building Energy Model	BEP-BEM
UCP	Wang et al. (2013)	Arizona State University Single-Layer Urban Canopy Model	ASLUM v2
UCP	Alexander et al. (2015)	Surface Urban Energy and Water Balance model	SUEWS
UCP	Wouters et al. (2016)	Semi-empirical URban canopY parametrization	SURY
FUCP	Lee and Park (2008)	Vegetated Urban Canopy Model	VUCM
FUCP	Krayenhoff et al. (2020)	Building Effect Parameterization with trees	BEP-Tree
FUCP	Redon et al. (2020)	Town Energy Balance with trees	TEB-Tree
FUCP	Wang et al. (2021)	Arizona State University Single-Layer Urban Canopy Model	ASLUM v3.1

2.3.1. Parametrizing aerodynamic effects

As explained in Section 2.2.2, both forest and urban canopies have similar aerodynamic effects on flows: reduced mean wind speeds within canopies and enhanced turbulence intensity at the top of canopies. Therefore, it is reasonable to use the same approach to represent these effects for forest and urban canopies. In previous studies, two approaches are commonly used: the roughness-length approach and the drag-force approach.

The roughness-length approach uses a roughness length $z0$ and a displacement height d to calculate wind velocity and turbulent fluxes at the ground surface (Equation 2.2.1). This approach is principally based on the Monin-Obukhov similarity theory, assuming stationary conditions and horizontal homogeneity. The main advantage of the roughness length approach is that it is easy to implement, thus commonly applied in models. However, this approach cannot capture the flow dynamics within the canopy (Brown, 2000).

The drag-force approach was first used for the forest canopy (Yamada, 1982) and then extended to the urban canopy (Brown, 2000; Martilli et al., 2002; Otte et al., 2004; Santiago and Martilli, 2010; Nazarian et al., 2020). In this approach a pressure force and viscous drag force are added in the momentum equation to represent the momentum loss, while a source term is added in the turbulent kinetic energy (TKE) equation to represent the production of TKE of canopies. The drag term considers the height dependence of the obstacles' density and thus blocking effect.

Otte et al. (2004) mentioned that the drag approach is better than the roughness length approach in terms of simulating wind and temperature fields within and above canopies. However, there are two disadvantages to both approaches. First, there is difficulty in determining the values of roughness length and drag coefficient (Masson, 2000; Brown, 2000). Secondly, canopy morphology diversity is not well represented. For example, wind flows in west-east and south-north directions behave differently due to the asymmetrical shapes and structures of street canyons. However, these effects are neither in drag-force approach nor in roughness-length approach calculated, since the values of building area density (or leaf area density) and roughness length for one specific grid cell in both approaches do not change according to the wind directions.

2.3.2. Parametrizing thermodynamic and hydrodynamic effects and air pollutant effects

Both FCP and UCP represent thermodynamic and hydrologic effects by modifying the surfaces energy and water balance equations. Depending on the complexity of representing canopy obstacles, equation modifications can be implemented at a slab surface or a single-layer or multiple layers.

The main difference between FCP and UCP lies in the representation of specific canopy processes such as photosynthesis processes for forests and anthropogenic heat and water emissions for cities. FCPs generally (e.g. Ronda et al., 2001; Bonan et al., 2018) consider photosynthesis processes (water, CO_2 uptake and release) and consider time-varying properties related to forest phenology, which are excluded in UCPs. For urban canopies, anthropogenic heat fluxes are parameterized by heat released directly into air (Brown, 2000; Masson, 2000), or being added into the surface energy budget (Arnfield, 2003). Besides, some FCPs (e.g. Deardorff, 1978; Noilhan and Planton, 1989) consider foliage interception reservoirs, while UCPs (e.g. Oke, 1988b; Masson, 2000) consider liquid or solid precipitation intercepted by urban surfaces and urban dew.

Some FCPs (e.g. Walko et al., 2000; Gustafsson et al., 2003) consider canopy properties and processes influenced by snow. The change of surface snow cover properties, freezing and thawing of soil, as well as local runoff of heavy precipitation and snowmelt, are parameterized (Walko et al., 2000). Several UCPs (e.g. Kusaka et al., 2001; Ryu et al., 2011; Wouters et al., 2016) take the change of solar azimuth angle into account for calculating radiation reflection and shading effects within canyons, however, this factor is often neglected in FCPs.

The impact of canopies on air quality mainly depends on the flow field (advection and diffusion of pollutants), which is considered in the parameterizations for the canopy effects on aerodynamics. A second influence of canopies is on chemical reactions as a result of changes in radiation and humidity; these are considered in parameterizations for the canopy effects on thermodynamics and hydrodynamics. A remaining influence of canopies on air quality is that canopies as pollutant sources influence chemical reactions. These are accounted for in the emissions models. The sources are frequently attributed to their actual height. Last not least, a very important influence of forest canopies and vegetation in general is photosynthesis and thereby CO_2 uptake and evapotranspiration. In summary, the canopy effects are considered without additional parameterizations by using the correct emission heights and parameterization types and approaches for dynamic,

thermodynamic and, hydrodynamic effects.

2.3.3. Assessment of canopy parameterizations

We assess in Table 2.3 the 28 parameterizations listed in Table 2.2 to investigate how detailed existing canopy parameterizations represent canopy-relevant processes, which are given as P1-P11 in Section 2.2.2.

Aerodynamic processes are considered in most FCPs (6 of 8 parameterizations) and UCPs (14 of 16 parameterizations), and in all four FUCPs. It can also be noticed that all multi-layer parameterizations (Type ML) employ the drag force approach (DA) for representing the aerodynamic processes. The roughness length approach (RA) is used in slab model (SB) and single-layer (SL) parameterizations.

All the 28 parameterizations partially or totally take account of thermodynamic processes including radiation transfer and heat transport. Although all FCPs consider the effects of long- and shortwave radiation attenuation, trapping, and emissions due to trees, only some of them (BATS, FCM, and CLM-ml) account for the shadowing effects (P4). Compared to the FCPs, the majority of UCPs consider the shadowing effects except for SUEWS, SURY, and UP. Most UCPs and FUCPs take account of anthropogenic heat emissions (P6). All FUCPs consider all relevant aerodynamic and thermodynamic processes (P1-P6). They differ in the complexity of hydrological processes, e.g. infiltration and soil water storage (P10) is only considered by ASLUM v3.1, which treats evapotranspiration (P8) somewhat less complex. Regarding the evapotranspiration, TEB-Tree is more complete, but it currently neglects infiltration. Hydrological processes are partially considered in all FCPs, but only half of the UCPs.

Table 2.3 also shows that the parameterization type (SB, SL, ML) does not play a role in the number and the complexity of the represented processes. For example, CLMU, ASLUM v2 and v3.1, which are single-layer parameterizations, consider almost all the relevant processes except photosynthesis. However, multi-layer parameterizations such as UP, BEP, and UCLM only consider aerodynamic and thermodynamic processes.

Table 2.3.: Canopy parameterizations with canopy-relevant processes (P1-P11; see section 2.2.3). parameterization types include slab model parameterization (SB), single layer parameterization (SL), and multi-layer parameterization (ML). Aerodynamic parameterization approaches include roughness-length approach (RA) and drag-force approach (DA). Acronyms see Table 2.2. Y means the process is represented, P means the process is partially represented. Table 2.3 is divided into three blocks, forest canopy parameterizations, urban canopy parameterizations and forested urban canopy parameterizations (see Table 2.2). Note that each block is sorted by parameterization type.

Parametrization	**Representation of processes**											**Type**	**Approach**
	Aerodynamic		**Thermodynamic**				**Hydrological**						
	P1	**P2**	**P3**	**P4**	**P5**	**P6**	**P7**	**P8**	**P9**	**P10**	**P11**		
SEBLV			Y	P	Y			P				SB	
SLVP	Y	Y	Y	P	Y		Y	Y	Y			SL	RA
BATS	Y		Y	Y	Y		Y	Y	Y	Y		SL	RA
SiB2	Y	Y	Y	P	Y		Y	Y	Y	Y		SL	RA
LEAF-2	Y	Y	Y	P	Y		Y	Y	Y	Y		SL	RA
VB95			Y	P	Y		Y	Y				SL	
TESSEL			Y	P	Y		Y	Y				SL	
FCM	Y	Y	Y	Y	Y			Y				ML	DA
CLM-ml	Y	Y	Y	Y	Y			Y				ML	DA
SUEWS			Y	P	Y	Y	Y	P	Y	Y	Y	SB	
SURY	Y	Y	Y	P	Y							SB	RA
UCLM	Y	Y	Y	Y	Y							SL	RA
TEB	Y	Y	Y	Y	Y	Y	Y	P	Y		Y	SL	RA

Parametrization	**Representation of processes**											**Type**	**Approach**
	Aerodynamic		**Thermodynamic**				**Hydrological**						
	P1	**P2**	**P3**	**P4**	**P5**	**P6**	**P7**	**P8**	**P9**	**P10**	**P11**		
SLUCM	Y	Y	Y	Y	Y	Y						SL	RA
CLMU	Y	Y	Y	Y	Y	Y	Y	P	Y	Y	Y	SL	RA
NSLUCM	Y	Y	Y	Y	Y	Y	Y					SL	RA
ASLUM v2	Y	Y	Y	Y	Y	Y	Y	P	Y	Y	Y	SL	RA
UP	Y	Y	Y	P	Y	Y						ML	DA
BEP	Y	Y	Y	Y	Y	Y						ML	DA
DA-SM2U	Y	Y	Y	Y	Y	Y	Y	P	Y	Y		ML	DA
UCPM	Y	Y	Y	Y	Y	Y						ML	DA
SUMM			Y	Y	Y							ML	
UP05	Y	Y	Y	Y	Y	Y						ML	DA
TEB08	Y	Y	Y	Y	Y	Y	Y	P	Y		Y	ML	DA
BEP-BEM	Y	Y	Y	Y	Y							ML	DA
ASLUM v3.1	Y	Y	Y	Y	Y	Y	Y	P	Y	Y	Y	SL	RA
VUCM	Y	Y	Y	Y	Y	Y	Y	P				SL	DA
TEB-Tree	Y	Y	Y	Y	Y	Y	Y	Y	Y		Y	SL	DA
BEP-Tree	Y	Y	Y	Y	Y	Y		Y				ML	DA

2.4. Conceptual model for a Generalized Canopy parameterization (GeCap)

Based on that a) the concepts of the forest canopy and the urban canopy are similar (Section 2.2.1); b) there are similarities between forest and urban canopy effects, and similarities between relevant processes within both types of canopies (Section 2.2.3); c) existing forest canopy parameterizations and urban canopy parameterizations use identical approaches to represent for example aerodynamic processes occurring in forest and urban canopies (Section 2.3), we conclude that it is possible to develop a generalized canopy parameterization for forest, urban, as well as forested urban canopies. We name this parameterization as GeCap parameterization. This section introduces the conceptual model of GeCap and discusses its possibilities.

2.4.1. Basic architecture of the conceptual model

The basic architecture of the GeCap parameterization consists of three parts, namely atmosphere, canopy, and soil (Figure 2.4). The three parts are connected with each other, and the canopy layer is acting as an interface between the atmosphere and the soil system. By introducing this concept, the canopy layer includes not only large obstacles like trees and buildings, but also uncovered soils. In practice, canopy parameterizations are usually coupled with atmospheric models and soil models, and these models provide e.g. meteorological information to the parameterizations (e.g., background wind, temperature, humidity, etc.), and force the parameterizations which in turn influence the atmospheric and soil variables. Therefore, atmosphere and soil as the external systems play important roles in affecting the whole canopy system.

As GeCap aims to represent forest and urban canopy effects in atmospheric models, the conceptual end-point is the canopy effects on the meteorological fields. Canopy effects are related to three main factors, namely canopy characteristics, processes occurring within canopies, and fluxes (Figure 2.5). Each factor has its function in the GeCap parameterization. Canopy characteristics serve as input data for GeCap, while fluxes serve as output. Processes represented in GeCap can be considered in atmospheric models by modifying the fluxes in the basic governing equations (e.g., conservation equation of momentum, surface energy balance, surface water balance, etc.), which is the main focus of GeCap. The thin arrows in Figure 2.5 indicate relations between factors. Canopy characteristics directly influence the processes. The processes taking place within canopies result in the

changes of meteorological fluxes, which indicate canopy effects and are considered in the equations of the atmospheric or the soil model.

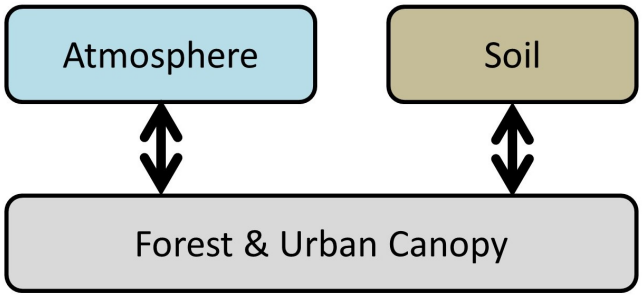

Figure 2.4.: The basic architecture of the conceptual model for GeCap parameterization. Arrows indicate relations between the canopy system and the external atmosphere and soil system.

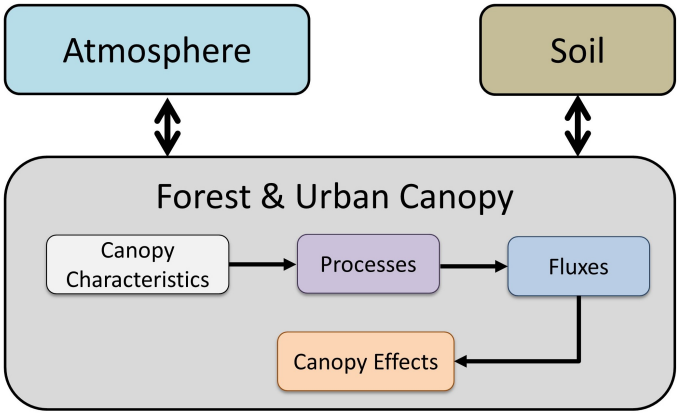

Figure 2.5.: As Figure 2.4, but with details within the canopy system. The thin arrows indicate relationship between the main four factors. The thick arrows indicate relationship between the canopy system and the external atmosphere and soil system.

2.4.2. Elements and relations in the conceptual model

Each factor in Figure 2.5 consists of a set of parameters or variables that are detailed in Figure 2.6.

To represent the diversity and heterogeneity of forests, forest canopy characteristics parameters are categorized into four groups: forest structure, forest type, forest phenology, and forest function. The parameters in each category commonly used in FCPs are summarized in Table 2.4. Different to the invariant parameters for urban canopies, many forest canopy characteristics parameters are time-varying parameters (e.g. leaf area index, albedo, canopy greenness fraction) due to forest phenology. For forest functions, GeCap mainly considers air pollutant emissions (BVOCs and pollen) and the carbon storage-sink function, which are associated with photosynthesis and stomatal parameters.

The heterogeneity of urban canopy structures demands a large number of input parameters for the canopy parameterizations (Grimmond et al., 2009; Schlünzen et al., 2011). By reviewing previous studies, the parameters that describe urban canopy characteristics can be categorized into four groups: urban geometry, surface cover, materials, and urban functions (Table 2.4). Urban morphology parameters consist of basic canyon or building information parameters (e.g. height, width, and canyon orientation) and the derived parameters (e.g. canyon aspect ratio and plan area index). Surface cover and materials of canopy elements are related to thermal parameters (e.g. thermal conductivity) and radiative parameters (e.g. albedo, emissivity), which contribute to modifying the surface energy balance at ground and building walls. Urban function parameters like anthropogenic heat emission can directly be used as direct input or be captured by specifying fixed internal temperatures and traffic counts (Grimmond et al., 2009).

For the forested urban canopy parameterization the forest/urban canopy characteristics should all be considered. It needs to be ensured that they are georeferenced so that the trees and buildings are placed correctly within the urban areas and to each other. This is important for the simulation of all the relevant processes. In addition, canopy characteristics serving as input should be combined and consistently given to the parameterization. It is challenging to use multiple data sources, e.g. with different types, resolutions, years, etc. GeCap should include the P1-P11 processes discussed in Section 2.2.3. After representing the relevant processes by modifying the fluxes in the governing equations, GeCap should predict several types of canopy layer influenced fluxes (e.g. momentum flux, radiative flux, heat flux, etc.). Note that using fluxes in models can better ensure mass and energy conservation than using just variables.

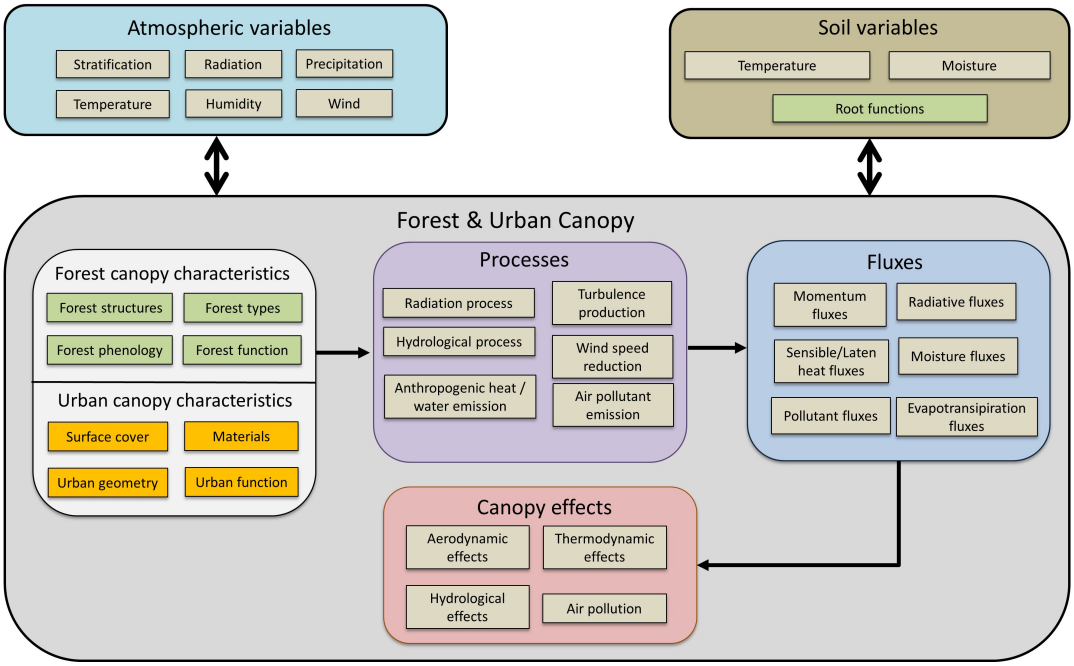

Figure 2.6.: Conceptual model for GeCap parameterization. Elements in the green and yellow boxes refer to the parameters specific for forest and urban canopies, respectively.

Table 2.4.: Summary of the parameters commonly used in previous forest canopy parameterization and urban canopy parameterization studies. G, R, and W refer to grounds, roofs, and walls, respectively.

Parameters in FCPs	**Parameters in UCPs**
Morphology	Morphology
- Leaf area index	- Plan area index
- Canopy (top & bottom) height	- Building /canyon height
- Leaf angle distribution	- Canyon orientation/ street direction
- Roughness length	- Roughness length
- Displacement height	- Displacement height
- Canopy cover fraction	- Frontal area index
	- Wall-plan area ratio
	- Building / canyon aspect ratio
	- Roof /canyon /building width
	- Sky view factor
Material	Surface cover and Material
- Albedo	- Albedo (G, R, W)
- Emissivity	- Emissivity (G, R, W)
- Leaf heat capacity	- Heat capacity (G, R, W)
	- Thermal conductivity (G, R, W)
	- Thickness (G, R, W)
Function	Function
- Photosynthesis parameters	- Anthropogenic heat emission
- Stomatal parameters	- Anthropogenic water emission
- Root parameters	- Storage capacity of pipes

2.4.3. Possibilities of GeCap parameterization

The conceptual model of GeCap systematizes canopy characteristics, relevant canopy processes and canopy effects, and gives an overview of those factors and parameters which are relevant for developing the parameterization. In this subsection, we discuss the possibilities of GeCap.

First, GeCap can serve as criteria for the parameterization assessment. GeCap helps to define which canopy processes and effects are required to be represented by a parameterization and helps to analyze if the fluxes are simulated consistently (e.g. evapotranspiration flux and latent heat flux). For instance, all four FUCPs mentioned in Section 3 (VUCM, TEB-Tree, ASLUM v3.1, and BEP-Tree) consider aerodynamic, thermodynamic, and hydrological processes, as well as the related effects. Theoretically, evapotranspiration can be calculated from latent heat by dividing by latent heat of vaporization, thus the values of these two fluxes should be consistent. GeCap should be able to check if the modified latent heat flux is consistent with the modified evapotranspiration flux due to the presence of canopies.

Secondly, GeCap can serve as a guideline for the design of canopy parameterizations. As its name indicates, the Generalized Canopy parameterization (GeCap) is designated to be suitable for forest, urban and forested urban canopies. In practice, forest- and urban-specific surfaces (e.g. roofs, walls, windows, roads, leaves, branches, and soil) should be first defined. The values for the relevant surface parameters (e.g. fractions, albedo, roughness length, thermal diffusivity, heat capacity etc.) should be determined. Then one could modify and solve the surface energy budget equation and water balance on different surface types. To represent radiation attenuation, multiple reflections, and trapping effects, GeCap should use a multi-layer shortwave and longwave radiation exchange scheme (P4 and P5 in Table 2.1). To represent aerodynamic effects induced by trees and buildings, and to capture vertical wind and TKE profiles within canopies (P1 and P2 in Table 2.1), the drag-force approach can be used in GeCap. The 3D values for drag coefficient, leaf (building) area density, and frontal area index can be supplied as input.

GeCap should be able to represent common effects of forest and urban canopies described in Section 2.2.3 for atmospheric models. Once realized and implemented, GeCap should help to answer concrete questions. For example, how much cooler cities will be in the summertime if more trees and vegetation are planted, or how much the power output of a wind turbine in urban or suburban areas will be reduced due to the modification of the urban area, or how urban forms implemented for future' sustainable cities affect local

meteorology.

The utility of GeCap will depend on the model and the used model physics, so some of the parameterization approaches will not be applicable. For example, using the drag-force approach to parameterize TKE production is not suitable for a prognostic mesoscale model that uses empirical equations for the eddy diffusivity (Brown, 2000). As GeCap aims to incorporate forest and urban canopy effects into one parameterization scheme, representation of the effects induced by urban and forest canopies that go in opposite directions should be considered as discussed in Section 2.2.3.

Moreover, one of the main differences between GeCap and existing FUCPs is that GeCap is suitable to be used in global scale models, as GeCap considers forests, cities, and forested cities at the same time. On local to global scales, forests and cities strongly affect the land-atmosphere interaction by modifying fluxes of water, energy, momentum, and greenhouse gases (Jackson et al., 2010; Boysen et al., 2020). For better understanding potential effects of deforestation and urbanization on climates of varying scales, deforestation and urbanization should be included in global scale models (Jackson et al., 2010; Boysen et al., 2020). However, existing canopy parameterizations are generally only coupled with regional-scale models, such as WRF (Lee et al., 2016b) and COSMO (Wouters et al., 2016). In this context, GeCap provides the framework for developing an advanced version of the current parameterizations that aims at including forest, urban and forested urban effects in global scale models at the same time. Practically, there are global scale forest and urban data sets available that can serve as input for GeCap, such as global Local Climate Zone map (Demuzere et al., 2022), global LAI map (Liu et al., 2012), and global anthropogenic heat flux map (Dong et al., 2017).

2.5. Conclusions

Forest canopies and urban canopies play critical roles in affecting boundary layer processes. The study investigates the most important effects of these two types of canopies on the atmosphere and highlights the importance of including canopies in the atmospheric models with a typical resolution of ˜1 km.

It was found that although forest canopies and urban canopies differ in terms of morphology, structure, and function, they share many of the same effects on aerodynamics and thermodynamics. Shadowing and radiation trapping effects should be considered for both types of canopies. In addition, wind speeds are reduced within canopies and turbulence intensity is enhanced above canopies. The different and opposing effects of forest

canopies and urban canopies are related to hydrological processes and air quality relevant processes. It is recommended that the similarities and differences between forest canopy effects and urban canopy effects should be taken more into account when including tree processes in urban canopies or developing forested urban canopy parameterizations for atmospheric models.

By reviewing previous canopy parameterization studies, we find that few parameterizations have incorporated all important processes in canopies. Thermodynamic processes are considered in most parameterizations but hydrological processes are usually neglected or only partially parameterized, especially in UCPs and FUCPs.

With increased model resolution, global-scale atmospheric models should be able to represent the averaged overall canopy effects by employing canopy parameterizations (WMO, 2023). In this context, a generalized canopy parameterization (GeCap) applicable to the forest, urban, and forested urban canopies is useful. The conceptual model for GeCap helps to better understand the relationship between canopy characteristics, processes, fluxes, and effects. In addition, GeCap can serve as a design outline for a parameterization to be used in atmospheric models of the forested urban canopy and enables a more general and abstract consideration of modelling future forested cities. It was beyond the scope of this paper to apply GeCap to mathematical quantitative models, providing instead a simple overview. Future work must be devoted to realizing the conceptual model numerically.

3. Realisation of GeCap by using a nudging method

This chapter has been published as:

Cheng, G., Schlünzen, K. H., Grawe, D., Voss, V., Thatcher, M., and Rayner, P. (2023) Parameterizing building effects on airflows within the urban canopy layer for high-resolution models using a nudging approach. *Quarterly Journal of the Royal Meteorological Society*, 149(755), 2617–2633. https://doi.org/10.1002/qj.4524

This chapter includes the full manuscript of the published paper. The original title of the paper has been modified for the chapter name. Layout and numbering of the paper have been adapted to this thesis document. The references and acknowledgements have been combined at the end of this thesis.

K. Heinke Schlünzen has contributed to the conceptualization. K. Heinke Schlünzen, David Grave, Marcus Thatcher, Peter Rayner have contributed to the discussion of results. Vivien Voss has contributed to the preparation of the microscale model data used for comparison.

Abstract

In this study, a new multi-layer urban canopy parameterization for high-resolution (˜1 km) atmospheric models using the nudging approach to represent the impacts of urban canopies on airflow is presented. In our parameterization, a nudging term is added in the momentum equations and a source term to the turbulent kinetic energy equation to account for building effects. The challenge of this parameterization lies in defining appropriate values for the nudging coefficient and the weighting function used to reflect the canopy effects. Values of both are derived and the developed parameterization is implemented and tested for idealized cases in the mesoscale atmospheric model METRAS. Comparison data are taken from obstacle resolving microscale model results. Results show that the parameterization using the nudging approach can well simulate aerodynamic effects induced within the canopy by obstacles there, in terms of reduction of wind speeds and production of additional turbulent kinetic energy. Thus, models with existing nudging can use this approach as an efficient and effective method to parameterize dynamic urban canopy effects.

3.1. Introduction

Information of flow characteristics within and above urban canopies is required in various urban studies, including urban air pollution modelling, urban wind energy, urban planning, building design, etc. The impacts of urban canopies on local climate include drag induced by buildings with consequent loss of momentum, enhancement of the conversion of mean kinetic energy into turbulence kinetic energy, and modification of the heat fluxes due to shadowing and radiation trapping effects (Roth, 2000; Martilli et al., 2002; Garuma, 2018; Cheng and Schlünzen, 2023). These impacts may be different at different vertical levels in the canopy. For instance, due to the presence of obstacles, shadowing effects within canopies are enhanced and more shortwave radiation is reflected within canopies than above canopies. In contrast, the aerodynamic effects of urban canopies might be similar at different heights, e.g. the reduction in wind speed and turbulence intensity occurs at ground level and within canopies (Table 1 in Cheng and Schlünzen, 2023). However, the intensity depends on density of the buildings and their height.

To reproduce the aerodynamic effects of urban canopies in high-resolution (˜1 km resolution) atmospheric models, two approaches are commonly used. The first approach is the roughness approach, which uses a gridded roughness length and a displacement height

to represent the impacts of surface obstacles on the mean airflow. The roughness length approach is based on the Monin-Obukhov similarity theory, which assumes stationary conditions and horizontal homogeneity. This approach is only implemented for the lowest atmospheric model layer. The second approach is the drag-force approach (Brown, 2000; Dupont et al., 2004). In this approach, a term is added to the momentum and turbulence kinetic energy (TKE) equations of the atmospheric models to account for obstacle drag. The approach allows representation of the urban canopy effects down to the surface and up to the height of the highest obstacle (Masson, 2006).

Both the roughness length and drag-force approaches have advantages, for instance, the roughness length approach is easy to implement and is generally used in atmospheric models while the drag-force approach can capture the flow dynamics within canopies, and the drag term considers the height dependence of the obstacles' density. However, the different approaches also have drawbacks. The main drawback of the roughness length approach is that it assumes a horizontal surface homogeneity within the roughness sub-layer using the constant-flux layer theory, and this simplicity sacrifices the realistic representation of atmospheric phenomena in urban canopies. The roughness approach can be satisfactory for modelling overall urban impacts on the atmosphere, but not be sufficient for generating more detailed meteorological fields, such as reproducing maximum observed TKE at the top of the urban canopy or reproducing the roughness sublayer over urban surfaces (Martilli et al., 2002; Otte et al., 2004; Garuma, 2018). The main disadvantage of the drag-force approach is that there is difficulty in determining the values of the drag coefficient, especially for the urban areas with highly complex surface geometries (Brown, 2000; Masson, 2000). In addition, this approach requires more computational time and more detailed information of urban morphology (Grimmond et al., 2009).

To overcome the drawbacks of the roughness length and drag-force approaches, a novel approach based on the nudging concept is developed in this study. The adjusted nudging approach is designed to simply and efficiently represent the aerodynamic effects of the urban surfaces on airflow at multi-levels within and above canopies and accounts for horizontal surface heterogeneity within the roughness sub-layer. Nudging or Newtonian Relaxation is a common method used in downscaling and data assimilation that dynamically adjusts the model toward forcing data, frequently to observations. The basic idea of nudging is to insert a non-physical linear diffusion term (the nudging term) that is proportional to the model-observation difference in the governing model equations so that the model is "nudged" toward the observations (Hoke and Anthes, 1976). Numerous studies have been presented describing the benefits of using nudging to constrain the evolution

of a numerical model, but no studies have explored the ability of nudging to be served as a canopy parameterization.

The main advantage of using nudging as an urban canopy parameterization is that this approach is easy to implement and there is low computational demand. Besides, nudging as a downscaling and data assimilation approach has already been implemented in many mesoscale models, e.g. COSMO (Bollmeyer et al., 2015; Schraff et al., 2016), METRAS (Dierer et al., 2005a; Dierer and Schlünzen, 2005b; Ries et al., 2010), MM5 (Nielsen-Gammon et al., 2007; Vinodkumar et al., 2008; Choi et al., 2009; Park et al., 2011; Solman and Pessacg, 2012), and WRF (Srinivas et al., 2010; Liu et al., 2013; Bullock et al., 2014; Wang et al., 2018) as well as global models, e.g. CAM6 (Kruse et al., 2022), ECHAM (Bauer and Wulfmeyer, 2009), and ICON (Zängl et al., 2022). This means that no additional effort is required to develop the approach itself, efforts are only required to determine the value of the nudging term, with which canopy effects are represented in models.

This chapter is organized as follows: Section 3.2 describes the nudging approach and the numerical model used. In Section 3.2.3 the new canopy parameterization based on the nudging approach is introduced. Section 3.3 describes the model setup for the test simulations, the comparison datasets for evaluation, and the parameter adjustment. In Section 3.4, simulation results of METRAS are compared with an obstacle resolving microscale model data set, in particular with respect to mean wind speeds and turbulence kinetic energy. Finally, the conclusions are drawn in Section 3.5.

3.2. Methods

3.2.1. Nudging

Let $\psi(\mathbf{x}, t)$ be a prognostic variable to be nudged. Nudging introduces an artificial tendency term, the so-called nudging term, into the tendency equations for the prognostic variable. The general form for the predictive equation of variable $\psi(\mathbf{x}, t)$ being nudged is written as follows:

$$\frac{\partial}{\partial t}\psi\left(\mathbf{x}, t\right) = F\left(\psi, \mathbf{x}, t\right) \underbrace{-\mathcal{W}\left(\mathbf{x}\right) \cdot \delta \cdot \left[\psi\left(\mathbf{x}, t\right) - \psi^{F}\left(\mathbf{x}, t\right)\right]}_{\text{Nudging term}}, \tag{3.2.1}$$

where $\psi(\mathbf{x}, t)$ is the predicted value computed by the model, $\mathbf{x}$ is the time independent spatial variables, t is the time, $F(\psi, \mathbf{x}, t)$ denotes the model's physical forcing terms (e.g.

pressure gradient force, Coriolis force, advection, etc.), $\mathcal{W}(\mathbf{x})$ is the weighting function (non-dimensional), δ is the nudging coefficient (s^{-1}) and $\psi^{F}(\mathbf{x}, t)$ the forcing data. The second term on the right side of the equation denotes the nudging term, proportional to the difference between the model state and the forcing data.

The nudging term is a non-physical linear diffusion term. Zou et al. (1992) mentioned that the nudging term should be large enough to impact simulations, but still be small enough so that it will not completely dominate the time tendency in the governing equation. According to Stensrud and Bao (1992), the nudging term is roughly an order of magnitude less than the other terms in the governing equations. Bollmeyer et al. (2015) stated that the nudging term remains smaller than the largest term of the original model forcing.

Simulation results are highly dependent on the product of nudging coefficient δ and weighting function $\mathcal{W}(\mathbf{x})$. If the model physical forcing terms $F(\psi, \mathbf{x}, t)$ are neglected and the weighting function $\mathcal{W}(\mathbf{x})$ equal to 1 is assumed, then the prognostic variable state $\psi(\mathbf{x}, t)$ relaxes exponentially towards the forcing data $\psi^{F}(\mathbf{x}, t)$ with an e-folding decay rate of $1/\delta$. The decay rate describes how much time the model needs until $\psi(\mathbf{x}, t)$ is adjusted by a factor of e to $\psi^{F}(\mathbf{x}, t)$. Relatively small values of δ induce more gradual modification, which helps limit dynamic imbalances that could cause an unstable solution. As the numerical stability criterion must be satisfied δ should follow: $\delta\Delta t \leq 1$, where Δt is the time step (Stauffer et al., 1991). Previous studies showed that typical values of δ are 10^{-4} to 10^{-3} s^{-1} for meteorological systems (Stauffer et al., 1991; Choi et al., 2009; Korsholm et al., 2015). For example, the default value for nudging coefficient in MM5 and WRF models is set to $3x10^{-4}$ s^{-1}. The values vary depending on the nudged variables, i.e. wind component, temperature, surface pressure, vorticity, etc.

The weighting function $\mathcal{W}(\mathbf{x})$ has a value between 0 and 1. Often nudging is only performed at the model boundaries, however, the data (e.g. measurements) might also be distributed unevenly in space (Koopmans et al., 2023). $\mathcal{W}(\mathbf{x})$ can be a spatial function, usually with a maximum amplitude of unity at where the distance between the forcing data and nudging grid point is the smallest and decreases to zero at other grid points (Brill et al., 1991). For nesting the values of $\mathcal{W}(\mathbf{x})$ may be larger at the lateral boundaries than in the inner of the model domain (Källberg, 1977; Ries et al., 2010) and for initialization be higher reducing in time (Dierer et al., 2005a). Moreover, the value of $\mathcal{W}(\mathbf{x})$ can also depend on time, the quality, character as well as accuracy of the forcing data (Hoke and Anthes, 1976; Stauffer et al., 1991; Brill et al., 1991).

The forcing data $\psi^{F}(\mathbf{x}, t)$ are external data sources that are used to drive the numer-

ical model. The forcing data variables are consistent with the nudged variables, such as wind component, temperature, pressure, humidity, precipitation, concentrations, soil moisture, velocity divergence, vorticity, etc. Depending on various applications, nudging has been developed to include different types of synoptic data as forcing data into numerical weather prediction systems, such as in-situ observations (e.g. Choi et al., 2009), radiosondes, radar, wind profiler, satellite and aircraft measurements (e.g. Schraff, 1997; Nielsen-Gammon et al., 2007; Vinodkumar et al., 2008; Srinivas et al., 2010; Liu et al., 2013), model results (e.g. Dierer et al., 2005a) or reanalysis data (e.g. Dierer et al., 2005a; Bauer and Wulfmeyer, 2009; Ries et al., 2010; Park et al., 2011; Peings et al., 2012).

Nudging is commonly used in operational numerical weather prediction because of its easy implementation and low computational demands, however, the method has its disadvantages. First, there is difficulty in determining the nudging coefficient and weighting function. Usually, they are adjusted empirically in sensitivity experiments and cannot be determined by using a theoretically optimal solution to the analysis problem through a mathematic formalism (Bollmeyer et al., 2015). Secondly, correlations between observation and model errors are not explicitly employed for this approach (Bauer and Wulfmeyer, 2009). Thirdly, nudging does not conserve energy. As a non-physical linear diffusion term is added to the governing equation, energy is lost at each time step due to nudging. Keeping the difficulties in mind, nudging may be employed for parameterizing building effects (Section 3.2.3).

3.2.2. METRAS model description

For the present study, nudging is extended to become the new canopy parameterization (Section 3.2.3) implemented in the mesoscale transport and stream model METRAS (Schlünzen, 1990). METRAS is a three-dimensional, non-hydrostatic model on surface fitted grids based on the conservation equations for momentum, mass and energy, simplified by using Boussinesq approximation, anelastic assumption, and may use a domain-constant Coriolis parameter for a small model domain (Schlünzen et al., 2018). METRAS solves the prognostic equations for horizontal and vertical wind components, temperature, specific humidity, cloud water and rainwater content as well as concentrations in flux form, density and pressure are derived from diagnostic equations. The model state variables are staggered using an Arakawa-C grid (Arakawa and Lamb, 1977). Subgrid-scale land-use representation and surface subgrid-scale characteristics are considered in the model via flux aggregation (von Salzen et al., 1996; Schlünzen and Katzfey, 2003). Urban influences are considered using a slab model (roughness approach) that shows similar results as the

complex canopy parameterization BEP (Grawe et al., 2013b).

The subgrid-scale turbulent fluxes are parameterized by a first-order closure which employs exchange coefficients. The exchange coefficient below $z = 10$ m (the lowest layer in METRAS) are calculated based on the Monin-Obukhov surface layer similarity theory with the near-surface turbulent fluxes calculated by flux averaging method using the concept of blending height (von Salzen et al., 1996). To determine the exchange coefficient above $z = 10$ m, a Prandtl-Kolmogorov closure is used in the present applications, which uses a mixing length and solves a prognostic equation for the sub-grid scale turbulence kinetic energy.

As mentioned in Section 3.2.1, there are no specific criteria on determining the value of nudging coefficient δ, the proper values are usually found empirically through sensitivity tests. For a standard nudging in METRAS to observations with a resolution of 1-5 km, δ is set to 10^{-3} s^{-1} (Davies, 1976; Källberg, 1977) which is equivalent to a forcing time scale of approximately 30 minutes at the boundaries. For an intensified nudging during initialization, the value is increased to 10^{-2} s^{-1} (Ries et al., 2010) resulting in a characteristic time of about 2 minutes at boundaries. For nesting METRAS into ECMWF reanalyses data, a decrease of $\mathcal{W}(\mathbf{x})$ from values of one at the open boundaries to values zero in the inner part of the model domain is implemented so that METRAS results are consistent with the reanalyses data at the boundaries (Ries et al., 2010).

3.2.3. Canopy parameterization by using the nudging approach

In the current study, we focus on parameterizing aerodynamic effects, i.e. representing the reduction of mean wind speeds and production of TKE due to the presence of obstacles in urban areas. We assume that there are no winds within buildings, which reflects the reality, and set the forcing field $\psi^{\mathrm{F}}(\mathbf{x}, t)$ in Eq. 3.2.1 to zero. Note that this is different from obstacle-resolving models, which typically use a building mask concept and directly set the prognostic variable $\psi(\mathbf{x}, t)$ of the building-covered grid cells to zero (Salim et al., 2018). Eq. 3.2.1 is rewritten for horizontal wind fields $U(\mathbf{x}, t)$ as follows:

$$\frac{\partial}{\partial t}U(\mathbf{x},t) = F\left(U, \mathbf{x},\ t\right) - \underbrace{\mathcal{W}\left(\mathbf{x}\right) \cdot \delta \cdot U\left(\mathbf{x},t\right)}_{\text{Nudging term}} \tag{3.2.2}$$

METRAS is based on the Reynolds averaged Navier-Stokes equations for describing the flow evolution. Employing Eq. 3.2.2 the prognostic equations of horizontal wind components $\overline{u}$ and $\overline{v}$ are calculated as follows in flux form (Schlünzen et al., 2018) neglecting

the coordinate transformation for simplicity:

$$\frac{\partial \rho_0 \alpha^* \bar{u}}{\partial t} = \underbrace{-\frac{\partial}{\partial x}\left(\bar{u}\rho_0\alpha^*\bar{u}\right) - \frac{\partial}{\partial y}\left(\bar{v}\rho_0\alpha^*\bar{u}\right) - \frac{\partial}{\partial z}\left(\bar{w}\rho_0\alpha^*\bar{u}\right)}_{\text{Advection}}$$
$$\underbrace{-\alpha^*\left(\frac{\partial \widetilde{p}}{\partial x}\right)}_{\text{Pressure-gradient force}} \quad \underbrace{+f\rho_0\alpha^*\left(\bar{v} - V_g\right) - f'\rho_0\alpha^*\bar{w}}_{\text{Coriolis force}}$$
$$\underbrace{+\frac{\partial}{\partial x}\left(2\rho_0\alpha^* K_{hm}\frac{\partial \bar{u}}{\partial x}\right) + \frac{\partial}{\partial y}\left[\rho_0\alpha^* K_{hm}\left(\frac{\partial \bar{u}}{\partial y} + \frac{\partial \bar{v}}{\partial x}\right)\right] + \frac{\partial}{\partial z}\left[\rho_0\alpha^* K_{vm}\left(\frac{\partial \bar{u}}{\partial z} + \frac{\partial \bar{w}}{\partial x}\right)\right]}_{\text{Force by turbulent fluxes}}$$
$$\underbrace{-\mathcal{W}\left(x,y,z\right)\delta\rho_0\alpha^*\bar{u}}_{\text{Nudging term}} \tag{3.2.3a}$$

$$\frac{\partial \rho_0 \alpha^* \bar{v}}{\partial t} = \underbrace{-\frac{\partial}{\partial x}\left(\bar{u}\rho_0\alpha^*\bar{v}\right) - \frac{\partial}{\partial y}\left(\bar{v}\rho_0\alpha^*\bar{v}\right) - \frac{\partial}{\partial z}\left(\bar{w}\rho_0\alpha^*\bar{v}\right)}_{\text{Advection}}$$
$$\underbrace{-\alpha^*\left(\frac{\partial \widetilde{p}}{\partial y}\right)}_{\text{Pressure-gradient force}} \quad \underbrace{-f\rho_0\alpha^*\left(\bar{u} - U_g\right)}_{\text{Coriolis force}}$$
$$\underbrace{+\frac{\partial}{\partial x}\left[\rho_0\alpha^* K_{hm}\left(\frac{\partial \bar{u}}{\partial y} + \frac{\partial \bar{v}}{\partial x}\right)\right] + \frac{\partial}{\partial y}\left(2\rho_0\alpha^* K_{hm}\frac{\partial \bar{v}}{\partial y}\right) + \frac{\partial}{\partial z}\left[\rho_0\alpha^* K_{vm}\left(\frac{\partial \bar{v}}{\partial z} + \frac{\partial \bar{w}}{\partial y}\right)\right]}_{\text{Force by turbulent fluxes}}$$
$$\underbrace{-\mathcal{W}\left(x,y,z\right)\delta\rho_0\alpha^*\bar{v}}_{\text{Nudging term}} \tag{3.2.3b}$$

Here $\overline{u}$, $\overline{v}$, and $\overline{w}$ are the Reynolds-averaged wind velocity components in the Cartesian coordinates, ρ_0 is basic state part of density, α^* is the grid volume, $\widetilde{p}$ is the pressure deviation, U_g and V_g are the horizontal components of geostrophic wind, which results from the balance between the Coriolis force and the large scale pressure gradient. The Coriolis parameters $f = 2\Omega\sin\varphi$ and $f' = 2\Omega\cos\varphi$ are calculated according to the local geographic latitude φ and the angular velocity of the Earth's rotation Ω. K_{hm} and K_{vm} denote the horizontal and vertical exchange coefficient, respectively. The last term on the right side of the equation is the nudging term with a negative sign representing the momentum sink.

In this study, δ in the nudging term is set to $5\text{x}10^{-3}$ s^{-1}, which is empirically determined

(Section 3.3.4). The corresponding time is similar to the value found for flow adjustment from obstacle resolving microscale model results, which was determined to "a few minutes" by Schlünzen et al. (2011). With the nudging coefficient $5x10^{-3}$ s^{-1}, wind speeds at obstacles are reduced, but the nudging effects are not too strong and additionally depend on the weighting function.

For the weighting function, we used two urban canopy parameters: building surface fraction and building height. Building surface fraction (bsf) is defined as the ratio of the building plan area to total plan area. In the current study, bsf of each grid refers to the fraction of subgrid-scale building within a grid volume. bsf is a three-dimensional array and the values are between 0 and 1, varying with space. The value of bsf for one grid column changes with height and reaches zero above the height of the tallest building. This means this approach is considered up to the height of the highest obstacle at a grid cell at place (x, y) starting from the surface. Then the weighting function is defined as

$$\mathcal{W}(x, y, z) = bsf(x, y, z) \tag{3.2.4}$$

$bsf(x, y, z)$ is zero without any buildings in the corresponding grid volume (x, y, z). With the parameter bsf, nudging is only active for the grid cell whose subgrid-scale land cover class belongs to urban classes, and the grid cell is partially or totally covered by obstacles.

The nudging approach is similar to the drag-force approach which also adds a diffusion term to the right-hand side of the conservation of momentum equation (Brown, 2000; Martilli et al., 2002). As the diffusion terms in both the nudging approach and in the drag-force approach contain height-dependent weighting functions, both approaches are height-dependent, from the ground up to the highest building, and proportional to the fractional area of the buildings. The difference between these two approaches is that the former is a purely mathematical linear diffusion term while the latter is a non-linear term ($\tilde{U}^2$) and has physical meaning.

One challenge to overcome is that nudging does not conserve energy, i.e. kinetic energy is lost at each time step by nudging winds. To overcome this problem, the lost kinetic energy is firstly tracked and then added back to the right-hand side of the subgrid-scale TKE equation as a source term at each time step and each model level.

At the lowest atmospheric model level ($z = 10$ m), the subgrid-scale TKE at time step

$n+1$, $\bar{e}^{n+1}$, is calculated in differential form as

$$\bar{e}^{n+1} = \frac{\left(u_*{}^{n+1}\right)^2}{{c_1}^2} \underbrace{+G^{n+1}}_{\text{Energy from nudging terms}}, \tag{3.2.5a}$$

$$G^{n+1} = \frac{1}{2}\rho_0\alpha^* \left\{ \left[\left(\bar{u}^{n+1}\right)^2 + \left(\bar{v}^{n+1}\right)^2 + \left(\bar{w}^{n+1}\right)^2 \right] - \left[\left(\bar{u}^{n}\right)^2 + \left(\bar{v}^{n}\right)^2 + \left(\bar{w}^{n}\right)^2 \right] \right\}, \tag{3.2.5b}$$

where $u_*{}^{n+1}$ is the friction velocity at time step $n+1$, and $c_1$is the proportionality constant. $\bar{u}^{n+1}$, $\bar{v}^{n+1}$, $\bar{w}^{n+1}$ and $\bar{u}^{n}$, $\bar{v}^{n}$, $\bar{w}^{n}$ are the Reynolds-averaged wind velocity components at time step $n+1$ and n, respectively. The original equation $\bar{e}^{n+1} = (u_*{}^{n+1})^2/{c_1}^2$ ensures continuous fluxes (Schlünzen et al., 2018). The additional G^{n+1} term is the energy resulting from the nudging terms, calculated by Eq. 3.2.5b, at the time step $n+1$, which is the kinetic energy change between the time step $n+1$ and n. It is added to the TKE equation, thus the G term represents the energy conversion of mean kinetic energy into turbulence kinetic energy $\bar{e}$ generated by the interactions between buildings and the airflow.

Above $z = 10$ m, where the first model level is located, the G term is added to the prognostic equation of the subgrid-scale TKE as follows

$$\begin{aligned} \frac{\partial \rho_0\alpha^*\bar{e}}{\partial t} = & \underbrace{-\frac{\partial \bar{u}_j \rho_0 \alpha^* \bar{e}}{\partial x_j}}_{\text{Advection}} + \underbrace{\rho_0\alpha^*\left(K_{ij}2S_{ij} - \frac{2}{3}\delta_{ij}\bar{e}\right)\frac{\partial \bar{u}_j}{\partial x_j} - \frac{\partial}{\partial x_j}\left(\rho_0\alpha^* K_{j,\chi}\frac{\partial \bar{e}}{\partial x_j}\right)}_{\text{Transport term}} \\ & \underbrace{-\rho_0\alpha^*\frac{g}{\theta_0}K_{3,\chi}\left(\frac{\partial \bar{\theta}}{\partial z} - \Gamma_\theta\right) - \rho_0\alpha^* g \cdot 0.61 K_{3,\chi}\left(\frac{\partial \bar{q}}{\partial z} - \Gamma_q\right)}_{\text{Temperature and humidity-related production}} \\ & \underbrace{-\rho_0\alpha^*\varepsilon}_{\text{Dissipation}} \underbrace{+G}_{\text{Energy from nudging terms}} \end{aligned} \tag{3.2.6}$$

Here $\bar{e} = 0.5\overline{\sum_{i=1}^{3} u_i' u_i'}$ is the mean TKE, i and j are indices taking values of 1, 2, and 3 for the three Cartesian coordinates (x, y, z), respectively; K_{ij} is the turbulent exchange coefficient for momentum in x_j direction; $S_{ij} = \frac{\partial \bar{u}_i}{\partial \bar{x}_j} + \frac{\partial \bar{u}_j}{\partial \bar{x}_i}$; δ_{ij} denotes the Kronecker delta; $K_{3,\chi}$ is the vertical exchange coefficient for the scalar variable χ. $K_{3,\chi}$ depends on the mixing length, the Richardson number and TKE. Γ_q and Γ_θ are the potential temperature counter gradient and humidity counter gradient terms, respectively, active for convective atmospheric conditions (Lüpkes and Schlünzen, 1996). The term G is representing the canopy-induced TKE source.

Thus, the parameterization using a nudging approach consists of three main steps (1) nudge winds; (2) track the lost kinetic energy due to wind-nudging; (3) add the lost

kinetic energy as a source term to the turbulence kinetic energy equation. A workflow is provided in the Fig. A.1 in the Appendix A.

3.3. Comparison data and model set-up

3.3.1. Meteorological microscale comparison data

To evaluate the urban canopy parameterization effects, observation data from meteorological stations are usually used, e.g. the Basel Urban Boundary Layer Experiment (BUBBLE) microclimate field campaign conducted in the city of Basel (Christen and Vogt, 2004; Rotach et al., 2005; Moradi et al., 2021). However, for the current assessment spatial average profiles over different types of canopies were needed. In this context, the data of a Reynolds-averaged Navier-Stokes (RANS) based obstacle resolving microscale model, which well captures the detailed characteristics of urban winds and turbulent flows at multi-levels above and within urban canopies, is an optimal choice to be used as the validation datasets. In addition, previous studies showed that RANS models can accurately simulate urban flow fields and are commonly used for microscale applications (Hertwig et al., 2012; Grawe et al., 2013a). Thus, in the current study, the published simulation result of the microscale transport and stream model MITRAS are used for model evaluation.

MITRAS is METRAS' sister model, it is a three-dimensional, non-hydrostatic, prognostic, numerical model for wind, temperature and humidity (Schlünzen et al., 2003; Grawe et al., 2013a; Salim et al., 2018). Obstacles (buildings, trees, etc.) are resolved explicitly in MITRAS using the building mask concept. MITRAS has been developed based on METRAS, and both models share many properties and parameterizations. For example, Monin–Obukhov similarity theory is assumed at the lowest model layer, and exchange coefficients above the lowest model layer are calculated using Prandtl-Kolmogorov closure.

The simulated microscale domain is described in Section 3.3.2. Vertically, the microscale model domain has 91 levels reaching 8587 m above ground with the lowest model level at 2.5 m above ground. The vertical resolution increases above 150 m non-equidistantly from 5 m to 200 m at the top of the model domain . Horizontal wind, vertical wind and TKE are calculated as influenced by the obstacles. Results are stored for all grid cells every 5 minutes (Voss, 2023) and are analysed as given in the Section 3.4.

3.3.2. Building data for the parameterization

The parameterization is tested for the central urban area of Hamburg (Germany). The 3D-city model LoD2 Hamburg, which contains building information, serves as input data. A microscale model domain covering 2.88 km^2 in the city centre of Hamburg is used. This domain includes different urban complexity, in terms of building height variability, elements of urban composition (e.g. Elbe River, Inner Alster Lake), and street patterns (Salim et al., 2015). It has 730 x 730 grid cells with a horizontal resolution of 2.5 m. Buildings in the domain are between 10 m (about 2.0% of all buildings) to 140 m high, and the average value of the building height, Hr, is 35.24 m.

To better understand the spatial distribution of building coverage over the model domain, we separated the centre area of the model domain (hereafter *Di*, note that *Di* has 600 x 600 grid cells) into nine equally sized subdomains (hereafter *Di1-Di9*), each has 200 x 200 grid cells and covers an area of 0.25 km^2 (Fig. 3.1). We then calculated building surface fraction for each subdomain and at different height intervals: 0-20 m, 20-40 m, 40-60 m, 60-80 m. These four height intervals correspond to the first four vertical layers in METRAS (lower to upper level of the corresponding layer). As the building surface fraction, information of *Di* is used to determine the weighting function for the nudging simulation in METRAS.

The distributions of building heights and building surface fractions in the nine subdomains show both clear differences and similarities (Fig. 3.2). For example, *Di8* which is mostly covered by Inner Alster Lake (Fig. 3.1), has the lowest building coverage (Fig. 3.2). The *Di4-Di7* are covered by higher and denser buildings compared to other subdomains. The average building heights of the nine subdomains are in the range of 31.6 m (*Di1*) to 41.2 m (*Di6*). The highest building with 140 m is located in the *Di2*. Note that orography is neglected for the present study.

The simulations were carried out for idealized meteorological conditions (Voss, 2023) summarized in Table 3.1 (column MITRAS). A diurnal cycle was not simulated, only the dynamic effect of the buildings is studied. Wind fields and turbulence kinetic energy values were analysed for the evaluation (Section 3.4) which are available at a 2.5 m horizontal and a 5 m vertical resolution within the canopy layer.

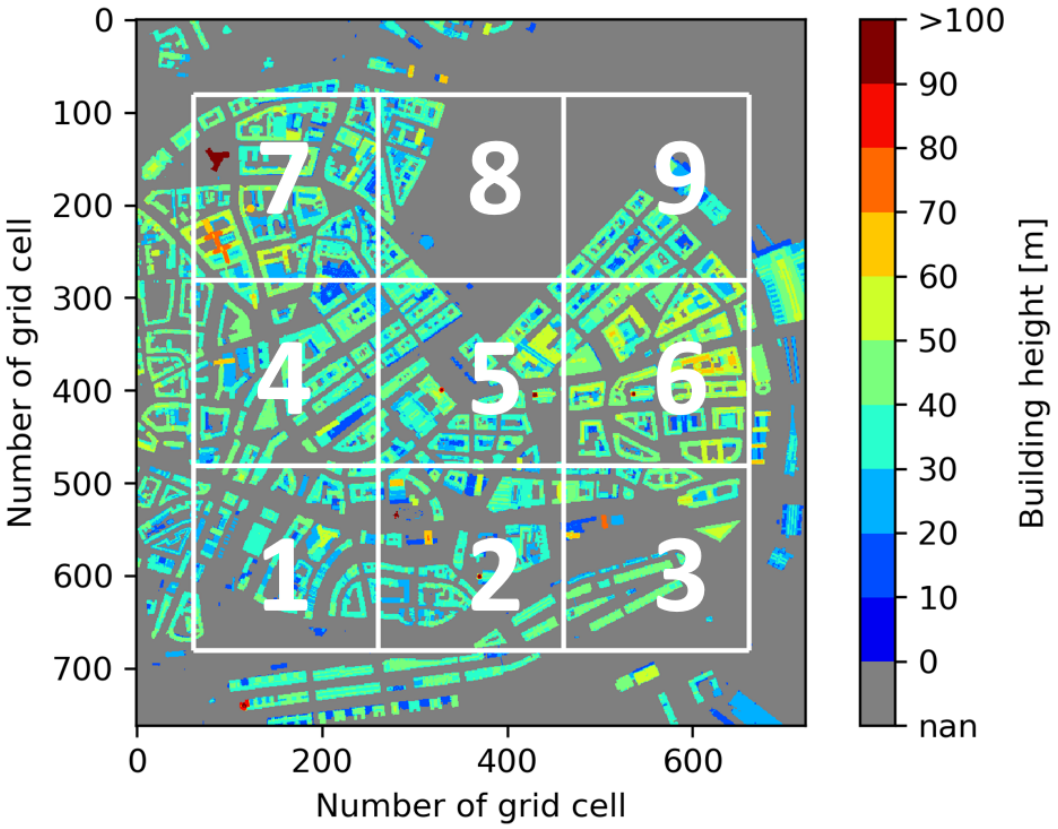

Figure 3.1.: Spatial distribution of building heights in the microscale model domain and schematic illustration of centre area (*Di*) division into nine subdomains (*Di1–Di9*). The whole domain *Di* has a 2.5 m horizontal resolution and covers 2.88 km^2. Each subdomain has 200 x 200 grids and covers 0.25 km^2. Grey spaces denote water, sealed or other open areas that are not covered by obstacles

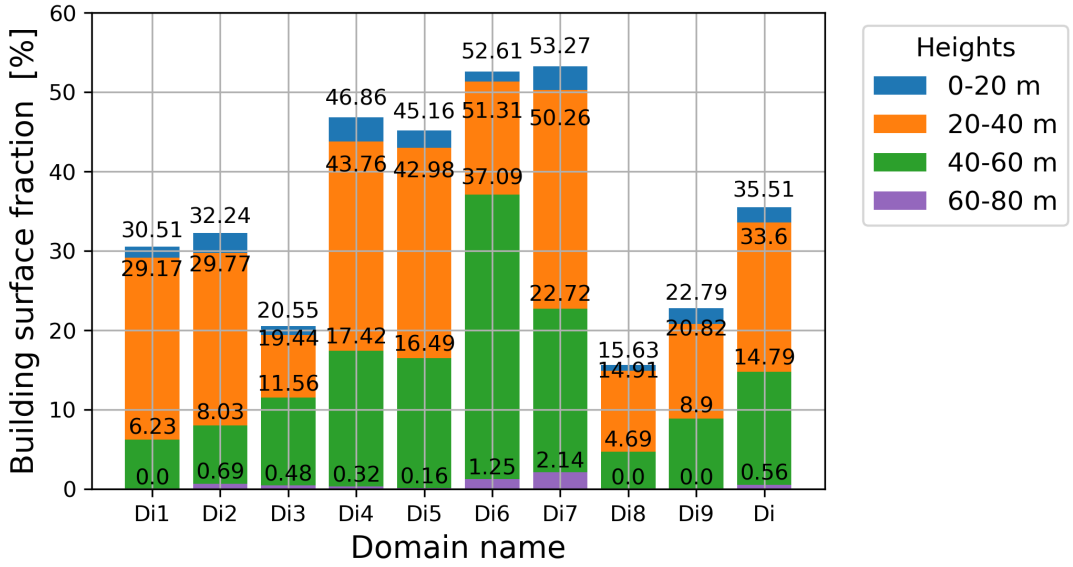

Figure 3.2.: Stacked bar chart of building surface fraction at different height levels for each subdomain *Di1-Di9* and for the microscale model domain *Di*. Choice of height level is based on the vertical layers in mesoscale model METRAS

Table 3.1.: Input parameters for this study, meteorological conditions in MITRAS and METRAS simulations

Variables	**MITRAS**	**METRAS**
Simulation time	From 4:00 am LST to 5:10 am LST	From 4:00 am LST to 10 am LST next day
Undisturbed wind speed from west at the model top	3.0 m/s	
Temperature at the surface	283 K	
Potential temperature gradient	0.005 K/m	
Surface pressure	1013 hPa	
Diurnal cycle	No	

3.3.3. Mesoscale model set up

Based on the microscale model domain *Di*, we developed a mesoscale model domain (hereafter *De*) for the model METRAS. The domain *De* covers 15 x 15 km^2 with 30 x 30 grid cells and has a horizontal resolution of 500 m. The nine grid cells (*De1-De9*) located in the domain centre represent the nine subdomains *Di1-Di9* (Fig. 3.3). The vertical resolution is 20 m near the surface with the lowest model level at 10 m, and increases above 80 m from 20 m to 1000 m vertical resolution at the top of the model domain at 12 km height. "Grass" fully covers the whole domain, except for the nine urbanized centre grid cells. As subgrid-scale land cover is allowed in METRAS, the nine centre grid cells are partially covered by the "compact sealed urban" and by the "grass" surface land cover class. The subgrid-scale surface cover fraction for the urban class is determined using the bsf values from 0 to 20 m (Fig. 3.2). The values for weighting functions in the nudging term for each urban grid cell at each vertical level in the *De* are identified using bsf calculated from *Di* (Fig. 3.3). The urbanized part in the model domain is admittedly very small. This size was deliberately chosen to assess, if the present nudging approach influences the model results sufficiently towards a more realistic simulation of the wind field within the urban canopy even if the model grid size is coarse compared to the extension of the urban area.

As the MITRAS simulation was carried out for idealized conditions (Voss, 2023) the METRAS simulations are carried out for the same idealized meteorological conditions. The values of input parameters are listed in Table 3.1. The ambient temperature is set to 283 K at the surface and it changes with height according to the potential temperature gradient of 0.005 K/m, which represents a stable atmospheric stratification. The diurnal cycle for temperature is not taken into account to purely study aerodynamic effects and their changes induced by nudging. Both simulations start for 4:00 am local standard time (LST), MITRAS is integrated for 70 minutes, while METRAS is integrated for 30 hours to assess possible longer term influences of the nudging. For comparison analysis, only the outputs from 4:00 to 4:45 LST are presented, since results change very little in the remaining time (not shown).

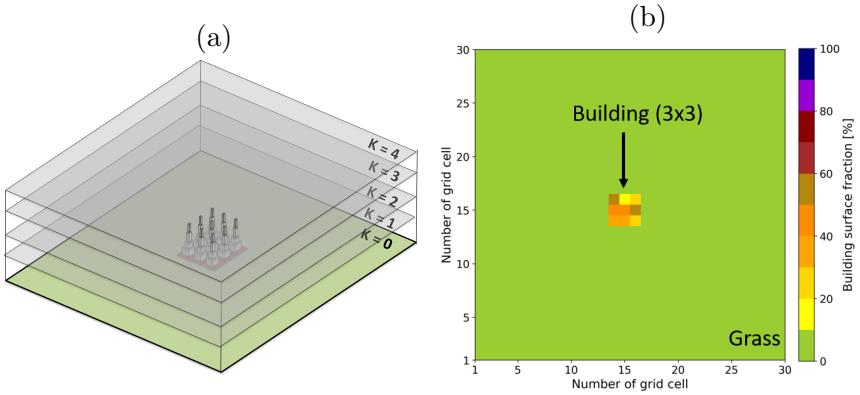

Figure 3.3.: (a) 3D illustration and (b) horizontal cross-section of the mesoscale model domain *De*. The building area covers 3x3 grid cells, grass covers 30 x 30 grid cells

3.3.4. Sensitivity study on nudging coefficient δ

Values of the nudging coefficient δ usually have to be selected empirically. We have conducted sensitivity experiments to assess how sensitive simulation results are to the changes of the nudging coefficient. δ was set to 5x10^{-1} s^{-1}, 5x10^{-2} s^{-1}, 5x10^{-3} s^{-1}, and 5x10^{-4} s^{-1}. Considering the average value of bsf over the nine urban grid cells from 0 to 20 m of 0.3551 (Fig. 3.2, column Di), the characteristic time $1/(\delta \cdot bsf)$ at the urban grid cells for each case is about 5 seconds for δ = 5x10^{-1} s^{-1}, 1 minute for δ = 5x10^{-2} s^{-1}, 10 minutes for δ = 5x10^{-3} s^{-1} and 100 minutes for δ = 5x10^{-4} s^{-1}.

Fig. 3.4 shows results for the temporal development of the spatially averaged wind profiles over the nine urban grid cells (*De1*-*De9*) in METRAS. For δ = 5x10^{-1} s^{-1} and 5x10^{-2} s^{-1}, in less than 5 minutes, wind profiles are close to steady state, however, there is almost no wind in the urban canopy layer which indicates that the nudging effects are too strong (Fig. 3.4a and 3.4b). Considering the average bsf of below 36%, light winds are to be expected in the canopy. For δ = 5x10^{-3} s^{-1}, the wind profiles are relatively steady within about 10 minutes as expected, and the nudging effects are neither too strong nor too weak (Fig. 3.4c). In addition, the value 5x10^{-3} s^{-1} also reflects the adjustment time of about 4 minutes obtained in the obstacle resolving micro-scale model for the wind (and temperature) profiles, as shown in the Fig. 4 by Schlünzen et al. (2011). For δ = 5x10^{-4} s^{-1}, the wind profile after 45 minutes is still almost the same as the basic state which means nudging has nearly no impact on wind velocities (Fig. 3.4d). Thus, δ is set to 5x10^{-3} s^{-1}.

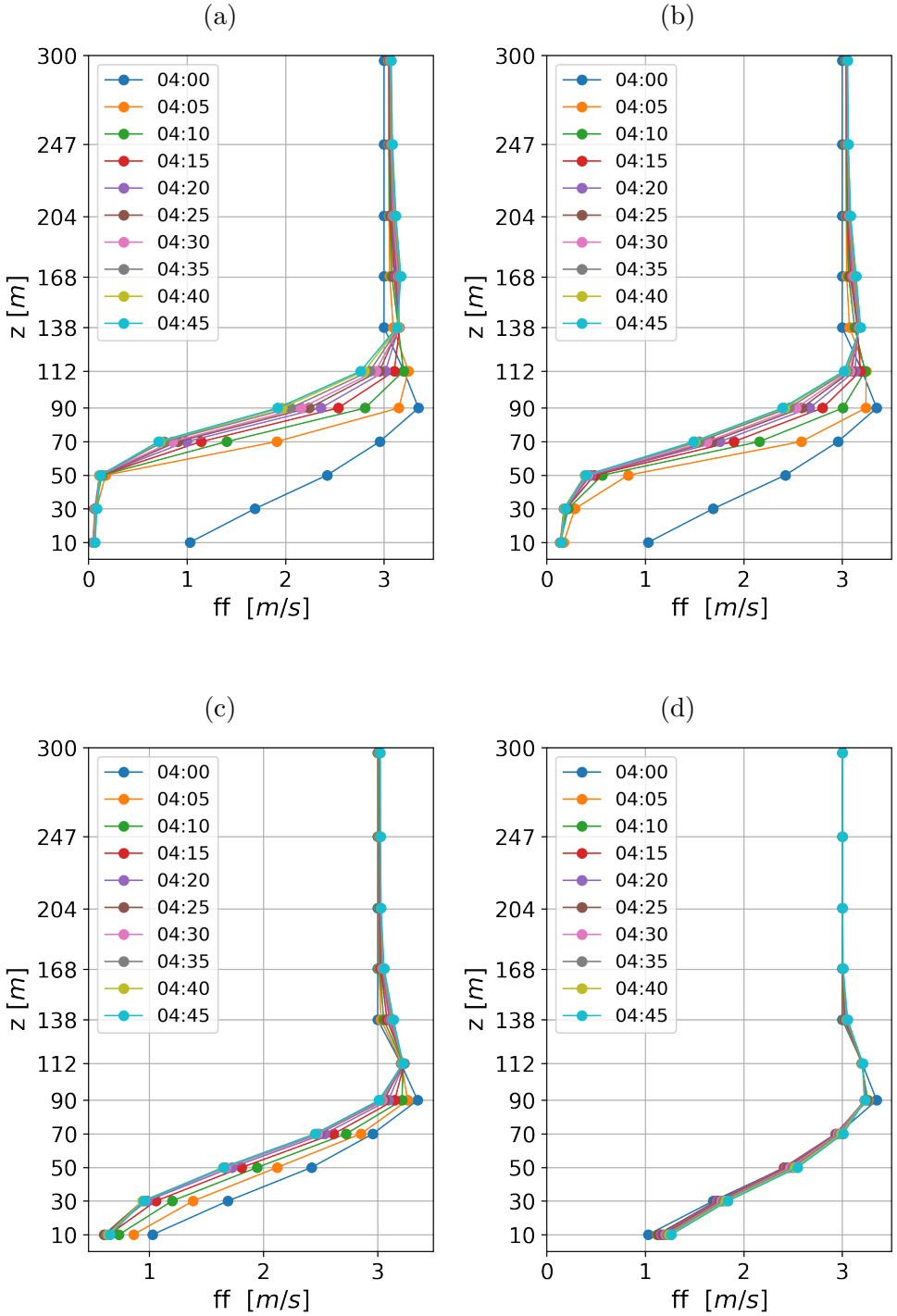

Figure 3.4.: Temporal development of spatially-averaged wind profiles over the nine urban grids (*De1-De9*) using METRAS for an integration starting 4:00 am LST (basic state) and the following 45 minutes. Simulations are carried out for the same initial meteorological conditions but with different values of the nudging coefficient: (a) δ = 5x10^{-1} s-1, (b) δ = 5x10^{-2} s^{-1}, (c) δ = 5x10^{-3} s^{-1}, and (d) δ = 5x10^{-4} s^{-1}

3.4. Comparison between METRAS and MITRAS data

In this section, a comparison between METRAS model results (with and without nudging) and MITRAS data is made for wind speeds and turbulence kinetic energy. We first compare results for the whole urban area (*De* and *Di*), then we go into details for each urban sub-domain (*De1*-*De9* and *Di1*-*Di9*).

3.4.1. Results over the whole urban area

Figure 3.5a presents a comparison between the vertical profiles of horizontally averaged wind speeds over the nine urban grid cells obtained from the METRAS run with nudging (METRAS-nud) and the average profile over the nine subdomains obtained from the MITRAS run (MITRAS). Results of the METRAS run but without using the nudging approach (METRAS-nonud) are added for comparison. Note that even though there are more vertical levels in the MITRAS model domain than in the METRAS model domain, MITRAS simulation results are chosen only at the mesoscale vertical layers for this comparison analysis, i.e., 10 m, 30 m, 50 m, 70 m, 90 m, 112 m, 138 m, 168 m, 204 m, 247 m, 300 m. If the microscale vertical level is not consistent with the mesoscale vertical level, the nearest-neighbour interpolation is used.

Figure 3.5a shows that both wind profiles obtained from METRAS-nud and METRAS-nonud peak at 90 m high. From 10 m to 70 m high, wind speeds of METRAS-nud and MITRAS show good agreement, suggesting that the nudging approach performs well in representing wind blocking effects in the canopy layers if appropriate values are used for the forcing field (here: zero wind speed) and the weighting function. Compared to METRAS-nonud, wind speeds of METRAS-nud and MITRAS are approximately 30 % lower.

At the levels above 90 m (z>2.5Hr, note that Hr is the average building height), both vertical profiles of METRAS-nud and METRAS-nonud runs overlap almost completely, indicating that the influences of obstacles on the mean flow are only up to the level $z \approx 2.5Hr$ and the airflow is fully adjusted to the underlying surface above this height. This is consistent with a previous study that horizontal homogeneity of the urban canopy flow is achieved at 2 to 5 times the average building height (Raupach et al., 1991). However, these two vertical profiles above 90 m are quite different from the MITRAS run, i.e. wind speeds of METRAS-nud and METRAS-nonud are lower than MITRAS. The reason for this is that buildings are explicitly resolved in the microscale model MITRAS and vortices caused by buildings are stronger in MITRAS than METRAS. Moreover, besides

horizontal transport, a large momentum transport from lower to upper levels and vice versa occurs in the MITRAS. i.e. updraft and downdraft vertical velocities are higher in MITRAS than METRAS-nud and METRAS-nonud (Fig. B.1 in Appendix B).

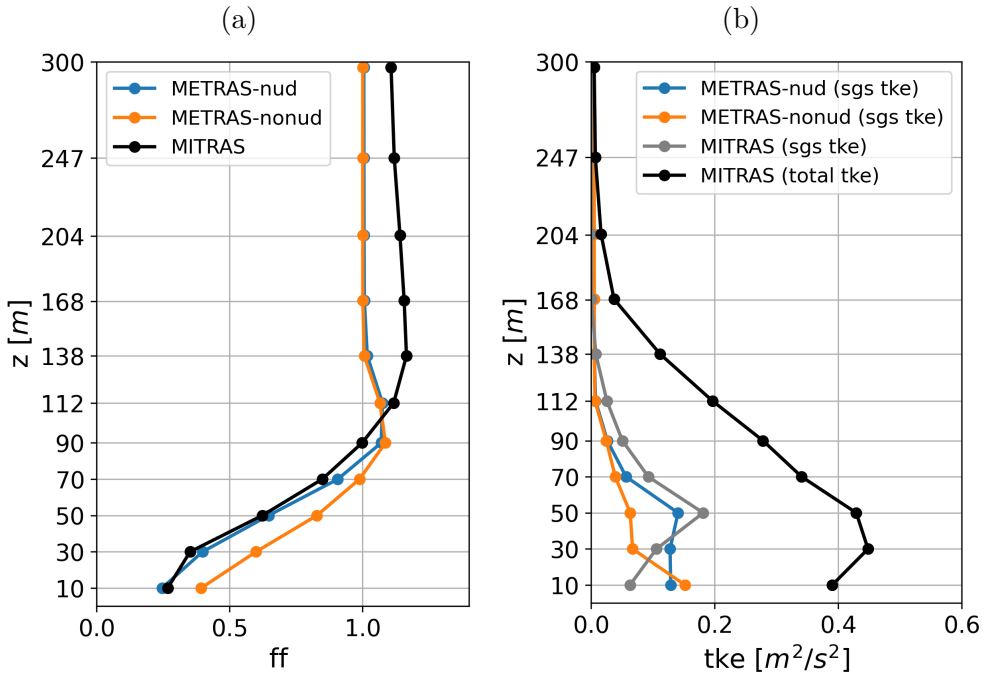

Figure 3.5.: Vertical profiles of horizontally averaged (a) horizontal wind velocity ff and (b) subgrid-scale TKE (tket). ff is normalized by the undisturbed wind speed (Table 3.1). The blue line represents the METRAS simulation with nudging (METRAS-nud), the yellow line the METRAS simulation without nudging (METRAS-nonud), and the black line the MITRAS simulation. For TKE the black line represents the total TKE obtained from the MITRAS simulation result (MITRAS (total tke)), the grey line subgrid-scale TKE obtained from MITRAS simulation result (MITRAS (sgs tke)).

For comparing TKE from METRAS and MITRAS, two terms are distinguished: the resolved TKE and the subgrid-scale TKE. The resolved TKE (TKE_{RES}) is calculated from the output velocity fields at each microscale model grid point i, given by Eq. 3.4.1:

$$\begin{aligned} TKE_{RES}(t) &= \frac{1}{n}\sum_{i=1}^{n}\frac{\hat{u}_i(t)^2+\hat{v}_i(t)^2+\hat{w}_i(t)^2}{2} \\ &= \frac{1}{n}\sum_{i=1}^{n}\frac{(\bar{u}_i(t)-\langle\bar{u}(t)\rangle)^2+(\bar{v}_i(t)-\langle\bar{v}(t)\rangle)^2+(\bar{w}_i(t)-\langle\bar{w}(t)\rangle)^2}{2}, \end{aligned} \tag{3.4.1}$$

where the resolved velocity deviations $\hat{u}_i(t)$, $\hat{v}_i(t)$, $\hat{w}_i(t)$, are calculated at each grid point

i as the differences between the instantaneous velocities at this grid point, $\bar{u}_i(t)$, $\bar{v}_i(t)$, $\bar{w}_i(t)$ (note that the over bars here refer to the Reynolds averaging as in Eqs. 3.2.3, 3.2.5, 3.2.6), and the horizontally averaged velocities, $\langle\bar{u}_i(t)\rangle$, $\langle\bar{v}_i(t)\rangle$, $\langle\bar{w}_i(t)\rangle$, respectively.

The parameterized subgrid-scale TKE (TKE_{SGS}) is directly calculated by the corresponding model. As mentioned above, for the current study the Prandtl-Kolmogorov closure solving a prognostic equation for the (TKE_{SGS}) is employed in both METRAS and MITRAS models. The sum of the (TKE_{RES}) and the (TKE_{SGS}) is the total TKE (TKE_{TOT}):

$$TKE_{TOT} = TKE_{RES} + TKE_{SGS} \tag{3.4.2}$$

Figure 3.6 illustrates the relationship between the TKE for a mesoscale grid and the TKE for a microscale grid system. For a single mesoscale grid (Fig. 3.6a), TKE of eddies is smaller than the grid size is the TKE_{SGS} (blue arrows). Assuming that the mesoscale grid consists of 4x4 microscale grid cells (Fig. 3.6b), the amount of the TKE_{SGS} for a single mesoscale grid should be approximately equal to the TKE_{TOT} of the corresponding 4x4 microscale grids, which is the sum of the TKE_{RES} and the averaged TKE_{SGS} over all 4x4 microscale grids. In the present study, the TKE_{SGS} obtained from METRAS and MITRAS are averaged over the domain De and Di, respectively. As the nine urban grid cells in the mesoscale model domain De represent the nine subdomains of Di, the averaged TKE_{SGS} over the nine urban grid cells in De should be approximately equal to the averaged TKE_{TOT} over the whole domain Di (note that for METRAS nine grid cells are in the domain De, while for MITRAS there are 360000 cells in the domain Di).

Figure 3.5b shows vertical profiles of the horizontally averaged TKE_{SGS} obtained from the METRA-nud and METRAS-nonud runs, the TKE_{SGS} and the TKE_{TOT} obtained from the MITRAS run. It was found that simulated TKE_{SGS} in both METRAS-nud and MITRAS run reach their maximum values at 50 m high ($z \approx 1.4Hr$, just above the mean building height) and reach zero at about 138 m high ($z \approx 3.9Hr$). This is similar to the results obtained in a wind tunnel study by Kastner-Klein and Rotach (2004), who modelled and measured turbulence structures within and above a realistic urban canopy with highly variable building heights and shapes and investigated that the maximum values of TKE occurred at 1 to 1.5 times the average roof level.

At 10 m above ground, the TKE_{SGS} of METRAS-nud is slightly lower than METRAS-nonud. The reason for this is that TKE_{SGS} is related to wind speeds, and wind speeds of METRAS-nud at 10 m are reduced due to nudging. At 10 m to 112 m TKE_{SGS} of METRAS-nud is above the values achieved without nudging (METRAS-nonud). Com-

pared to the TKE_{SGS} of the MITRAS run, more TKE_{SGS} is obtained from the METRAS-nud run at 50 m above ground, which indicates that the parameterization induces some of the canopy-induced TKE. However, above 50 m high, the TKE_{SGS} of METRAS-nud is below that of the MITRAS. In addition, when comparing the TKE_{SGS} of METRAS-nud to the TKE_{TOT} obtained from the MITRAS run, the latter has much higher values than the former within and above canopies. This inflects that the nudging parameterization underestimates canopy induced TKE and an extra source of TKE is required. Two main reasons could cause this underestimation. First, the resolved buildings in MITRAS cause more surround-building vertical vortices, thus more TKE is produced. Secondly, the subgrid-scale urban spatial heterogeneity including building height variation and street patterns are not represented in the nudging parameterization used for the mesoscale model domain. The turbulence caused by the complex buildings in the airflow is thus only partly represented by the nudging approach, where the lost kinetic energy by nudging is added to the TKE_{SGS}.

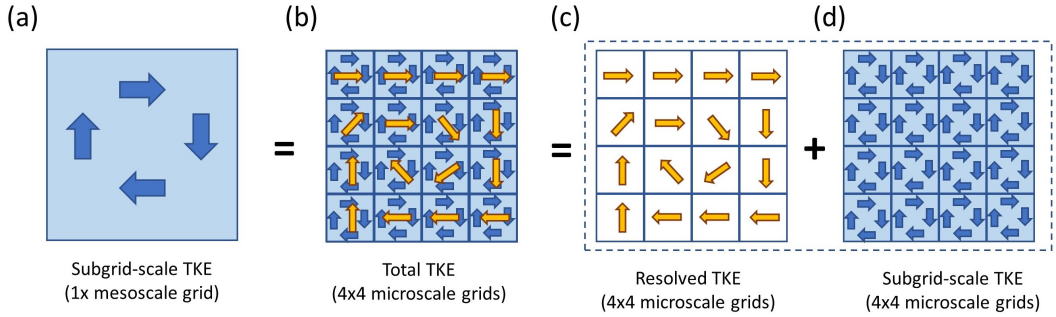

Figure 3.6.: Schematic illustration of the relationship between the subgrid-scale TKE of (a) a mesoscale grid and (b-d) the total TKE of microscale grids assuming that the mesoscale grid consists of 4x4 microscale grid cells. The yellow arrows denote large eddies that can be resolved by the microscale model. The blue arrows in the mesoscale grid and the microscale grids denote small eddies that cannot be directly resolved in mesoscale models and microscale models, respectively

3.4.2. The impacts of building surface fraction on airflow

To better study the effects of building surface fraction on airflow, we categorized the subdomains into three groups based on the values of bsf at the heights of 0-20 m (See Fig. 3.2): *high bsf* (*Di7*, *Di6*, *Di4* and *Di5*), *middle bsf* (*Di2* and *Di1*), and *low bsf* (*Di9*, *Di3* and *Di8*). Fig. 3.7 shows vertical profiles of horizontally averaged wind speeds over each subdomain in *Di* from the MITRAS run (Fig. 3.7a) and for the same domain

from the METRAS-nud run (Fig. 3.7b) at all corresponding grid levels. Results from the MITRAS run show that averaged wind speeds of each subdomain for the lower altitudes below ~ 50 m are related to the building surface fraction, wind speeds of the *high bsf* group (*Di7*, *Di6*, *Di4*, *Di5*) are lower than the *middle* (*Di2* and *Di1*) and *low bsf* (*Di9*, *Di3* and *Di8*) groups. In general, *higher bsf* results in lower wind speeds within the canopy (Fig. 3.7a). However, due to the vertical momentum transport (Fig. B.2 in Appendix B), this signal is not pronounced at the higher latitudes above ~ 50 m. Different from a high spatial variation in wind speeds of the nine subdomains from the microscale model results, Fig. 3.7b shows that wind speeds of the corresponding nine mesoscale urban grids in *De* do not vary greatly. The reason for that might be that all nine urban grid cells are closely located and the effects from neighbouring grids are strong. For example, *Di5* belongs to the *high bsf* group but has the lowest wind speeds due to its location in the centre of the domain. With an urban area of 3x3 grid points the relatively small spatial differences are not surprising, keeping in mind that "... 5-8 grid lengths is the scale of the atmospheric process that is captured by a model" (WMO, 2023). Thus, the effect of flow reduction is represented, but as to be expected, the heterogeneity cannot be reproduced.

Figure 3.8 shows the vertical profiles of the horizontally averaged TKE_{SGS} over the nine subdomains in *Di* and TKE_{SGS} of each corresponding urban grid cell *De*. It is evident that the profiles are influenced by building surface fraction (Fig. 3.8a). *Di6* with the highest bsf (0.51) at 20-40 m above ground has higher TKE_{SGS} compared to other subdomains (Fig. 3.8a and 3.8b). In addition, it is worth noting that the TKE_{SGS} from the MITRAS simulation reaches the maximum between 30 and 50 m (between about 1.0 and 1.5 z/Hr). However, this pattern cannot be seen in Fig. 3.8b due to the coarser vertical resolution in METRAS.

Moreover, the MITRAS result (Fig. 3.7a and Fig. 3.8a) shows that the impacts of urban heterogeneity on the mean flow and turbulence kinetic energy distributions are clearly noticeable up to about 168 m ($z \approx 5Hr$), which is higher than $z \approx 3Hr$ mentioned in the study by Kastner-Klein and Rotach (2004). Above 168 m, the spatial variation in mean velocity and turbulence kinetic energy is less than 15% and 2%, respectively. However, the METRAS-nud result (Fig. 3.7b and Fig. 3.8b) shows that the influences of urban heterogeneity are pronounced only up to 90 m ($z \approx 2.5Hr$).

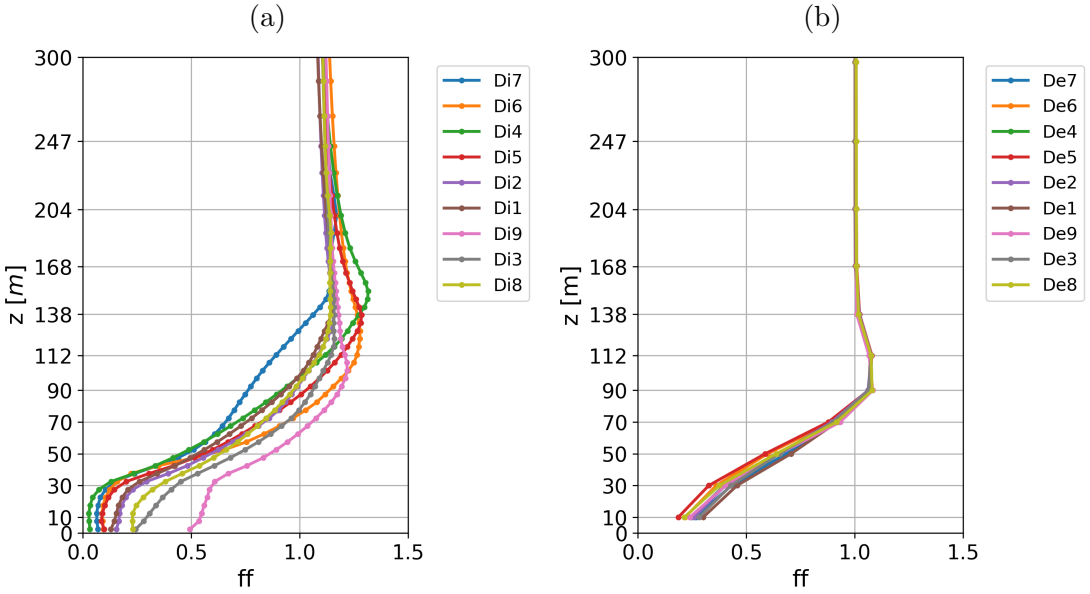

Figure 3.7.: Vertical profiles of horizontally averaged wind velocity ff for each subdomain (a) from MITRAS (Di) and (b) from METRAS (De). ff is normalized by the wind speeds at free atmosphere. Labels are sorted according to the building surface fraction at 0 to 20 m of each subdomain in Di, from highest ($Di7$) to lowest ($Di8$)

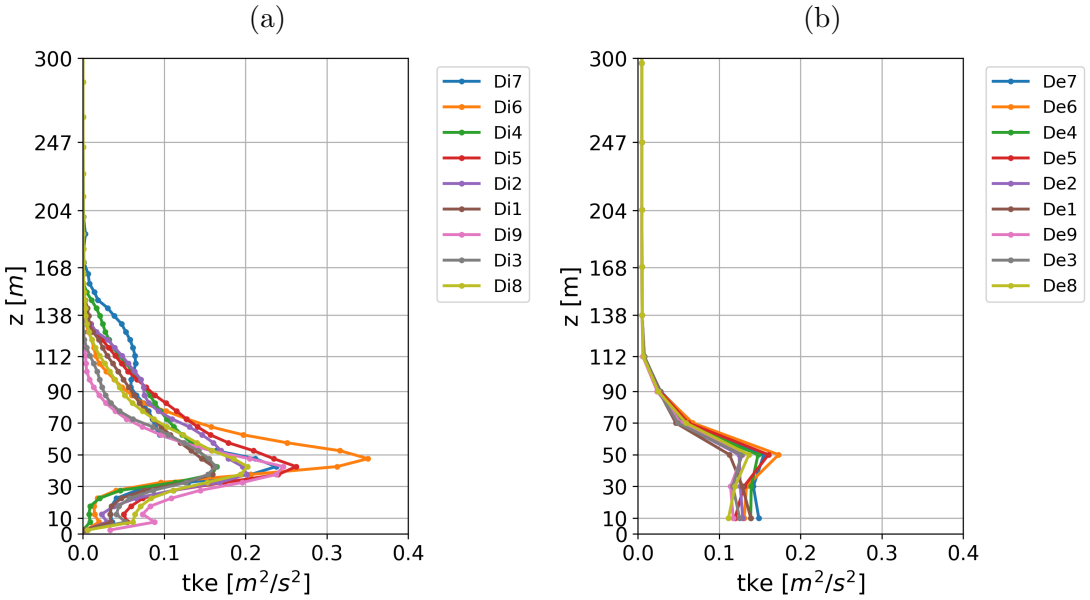

Figure 3.8.: Same as Fig. 3.7 but for subgrid-scale turbulent kinetic energy

3.5. Discussion and Conclusions

It is important to take canopy layer influences on wind and turbulence into account when simulating meteorological fields in urban areas with mesoscale models. The main objective of our study is to show the possibilities and limitations of using the nudging approach as an urban canopy parameterization. The parameterization is novel in terms of its simplicity and efficiency to represent the effects of urban canopies on airflow, i.e. the canopy-induced momentum sink and partly provides a turbulence kinetic energy source. The simplicity of this parameterization allows it to be tested, evaluated and then further implemented in other high-resolution atmospheric models, such as COSMO, WRF, MM5, etc.

To overcome one of the main drawbacks of nudging that it does not conserve energy, we track the lost kinetic energy and add the amount of energy into the TKE equation as a source term. It is shown that TKE productions are represented. However, TKE is still underestimated compared to the model results of the obstacle resolving model MITRAS. This suggests that an explicit obstacle-induced source of TKE should be included in addition to the conversion of mean kinetic energy to TKE, which, however, would leave the concept of a simple nudging parameterization and might make it less attractive for use as a simple canopy parameterization in mesoscale and global scale models. In addition, results also show that the vertical turbulent transport is not well reflected by the parameterization. We suggest that the relevance of enhanced vertical transport needs to be assessed in evaluations for realistic cases (e.g. hindcast of an urban heat island situation for a moderate wind situation and comparison with measurements).

One particular challenge in urban modelling studies is to deal with the relationship between the real complexity of urban morphology and the simplified morphology adopted in the parameterization (Martilli et al., 2015). Two parameters, namely building height and building surface fraction, are used in the current parameterization. Comparison results show that the parameterization using these two parameters can well represent aerodynamic effects. However, the underestimation of the TKE might be related to the simplification of urban morphology. At this point, more parameters may be needed to define the simplified morphology. Ching et al. (2018) have summarized the common urban canopy parameters required for the urban climate modelling, such as building frontal density, vegetation fraction, street orientations, etc. Nowadays there are more high-resolution urban morphological datasets available for many cities in the world. For example, the Urban Atlas data developed by European Environment Agency (EEA) (2018) contains

building height information with 10 m resolution and street tree information in major cities in Europe. In addition, the Local Climate Zone (LCZ) characterizes urban landscapes by a range of urban morphological and physical parameters (Stewart and Oke, 2012). Using the LCZ classification framework, the World Urban Database and Access Portal Tools (WUDAPT) project has characterized many cities around the world in a consistent way and developed the corresponding LCZ maps (Ching et al., 2018). A study by Demuzere et al. (2022) has developed the global LCZ dataset with a resolution of 100 m. It has to be investigated using obstacle resolving models, what influence the class ranges have on spatially averaged microscale model results and if this is comparable with the simplifications inherent to the current simple nudging approach with TKE source.

For further implementations of the parameterization in various models, it might be necessary to verify the characteristic time $1/(\delta \cdot bsf)$ and ensure numerical stability for the time steps the model uses (Section 3.2.1). For most high-resolution models, the model time step has a range of several tens of seconds to several minutes, depending on the horizontal grid resolution. For example, the time step (in seconds) for WRF is usually set to approximately 6 times the horizontal grid resolution (in kilometers); the time step for MM5 is approximately 3 times the grid resolution (Skamarock et al., 2019), and the time step for METRAS is varied but less than one minute. With these time steps, the characteristic time of nudging should be set accordingly to this range, i.e. several minutes. This guarantees that model states are nudged to forcing fields within just a few time steps. Thus, the nudging coefficient $\delta = 5\text{x}10^{-3}$ s^{-1} used in this study (corresponding to a characteristic time of e.g. 3 minutes for a 100% building-covered model domain) can be generally used for different studies on various models. The value of the weighting function, which is the height dependent building surface fraction (bsf), needs to be adjusted to different urban areas.

Future research might consider possible developments of the nudging coefficient. The nudging term in this study is linear to the wind speed itself. Different from that, the traditional drag-force approach (e.g. Brown, 2000; Dupont et al., 2004) parameterizes wind reductions by using the drag term with a form of the square of the wind speed, which is physically more correct. Theoretically, one could also use a nudging coefficient dependent on wind speed. We did not try this approach that demands for time dependent calculation of the coefficient, because it might hinder the nudging implementation as parameterization of urban effects into non-urbanized mesoscale and global-scale models.

From the thermodynamic perspective, cities exert great influences on the local and regional weather and climate, such as urban heat island (UHI) phenomenon, anthropogenic

heat emissions, radiation trapping due to obstacles, etc. It is known that the UHI intensity depends on wind speed and is smaller for larger wind speeds (Schlünzen et al., 2010). In the next step, the influence of the current parameterization on thermodynamic effects of cities e.g. UHI will be investigated in realistic cases including the calculation of temperature, relative humidity, clouds, rain, and diurnal cycles in the simulations. Moreover, further research can investigate if nudging of temperature and humidity might improve modelling results.

4. Application of GeCap with realistic urban morphology

This chapter has been prepared for publication as:

Cheng, G., Schlünzen, K. H., Grawe, D., Thatcher, M., and Rayner, P. (2023). What are the influences of a simple parameterization on the urban heat island? In preparation for *Quarterly Journal of the Royal Meteorological Society*.

This chapter includes the full manuscript of the prepared paper. The original title of the paper has been modified for the chapter name. Instead of citing Cheng et al. (2023) reference is given to the corresponding section of this thesis.

K. Heinke Schlünzen has contributed to the conceptualization. K. Heinke Schlünzen, David Grave, Marcus Thatcher, Peter Rayner have contributed some ideas for analysis.

Abstract

Increasing urbanization requires a better understanding and representation of urban effects and urban canopy processes in weather and climate modelling at various scales. This study investigates how an urban canopy parameterization based on an extended nudging approach can improve the modelling of urban aerodynamic and thermodynamic effects at a 500 m grid spacing in the mesoscale model METRAS. A realistic urban morphology dataset, including building heights and building surface fractions, was used as input for the parameterization. The results demonstrate that the extended nudging approach can accurately simulate the wind reduction effects due to canopy obstacles, with the largest wind reduction being simulated in the city center. In addition, the urban heat island effect simulated using the slab model scheme in METRAS, was enhanced using the urban canopy parameterization, with the highest intensities in the densely built areas. These results, along with the simplicity of the approach, suggest the potential of using this parameterization to represent urban effects in global-scale weather and climate models.

4.1. Introduction

Urban areas only account for less than 3% of the global surface coverage, yet they are home to around 55% of the world's population (UN, 2019). They have considerable influences on meteorology, air quality, and climate change from local to regional, up to global scales (Oke et al., 2017; Baklanov et al., 2018). In modelling studies, urban effects in terms of the urban surface-atmosphere interactions are parameterized in mesoscale and global scale models due to their coarse model resolutions and the limited computational capabilities (Kusaka et al., 2001; Martilli et al., 2002; Masson, 2006; McNorton et al., 2023).

Current urban canopy parameterizations implemented in the mesoscale modelling can be generally categorized into three types: slab model, single layer parameterization, and multi-layer parameterization, depending on the level of detail in representing the vertical structures of urban canopies (Ryu et al., 2011; Cheng and Schlünzen, 2023). To analyze urban impacts on the global weather and climate, these parameterizations can be included in global scale climate models. For example, by including an urban land surface scheme into the Hadley Center Global Climate Model, McCarthy et al. (2010) investigated the impact of urbanization on local climate change and the change in the urban heat island intensity under different scenarios of CO_2 and anthropogenic heat release. Katzfey et al. (2020) introduced a single-layer urban canyon parameterization into the global Conformal

Cubic Atmospheric Model at a resolution of 50 km and showed that local urban effects such as an increase in minimum air temperature, a decrease in surface latent heat flux, and an increase in surface sensible heat flux, were well simulated. McNorton et al. (2023) introduced a single layer urban canopy scheme into the ECMWF Integrated Forecasting System global forecast model at ~ 9 km horizontal resolution and showed that the urban scheme can improve forecasting 2 m temperature and 10 m wind over urban areas.

Urban effects can also be represented in global-scale climate models by including urban parameters in the models, such as urban land cover/land use, urban morphology, thermal and radiative properties of urban surfaces, energy usage, anthropogenic heat release, and greenhouse gas emissions (Katzfey et al., 2020; Zhang et al., 2013; Chen et al., 2016). This requires high-quality data at a global scale as input for models. Nowadays, more and more of these data are available, such as the global-scale Local Climate Zone map by Demuzere et al. (2022), and the global gridded anthropogenic heat flux dataset by Jin et al. (2019). In addition, global scale weather and climate models have also been improved in terms of spatial resolution. For example, Wedi et al. (2020) presented that an average global grid spacing of 1.4 km was used for the ECMWF's hydrostatic Integrated Forecasting System (IFS) in a global, four-month simulation. It is projected that a global weather or climate model with higher model resolution, higher computational capabilities, an efficient urban parameterization, and global-scale urban parameter maps as input, can enable a better representation of urban effects.

Nudging is a traditional data assimilation approach used in regional and global numerical weather and climate models. It can also be used in urban climate modelling to represent some of the urban effects. For example, Cheng et al. (2023) used nudging with idealized urban morphology information in a mesoscale model and demonstrated that nudging was efficient in representing the effects of urban canopies on airflow, including the reduction of wind speeds and the production of turbulent kinetic energy. They also mentioned the temperature nudging to represent thermodynamic urban effects, such as the urban heat island (UHI) phenomenon. Koopmans et al. (2023) applied a temperature nudging approach using personal weather stations and 3D variational data assimilation for the urban environment of Amsterdam at a 100 m grid spacing, and they found that nudging can improve the prediction of the UHI. However, urban morphology information was not used in their study.

This chapter builds on the work of Cheng et al. (2023), and the main objective is to apply the nudging approach with realistic urban morphology and investigate how it improves the representation of urban canopy effects on temperature and wind fields. Special

focus is put on the canopy layer UHI, which is defined as the near-surface air temperature differences between the urban and rural areas at about 1.5 m above ground WMO (2023). It should be noted that, the lowest model level in this study is 10 m above ground level and therefore the canopy UHI refers to the value at this level.

The chapter is organized as follows: In Section 4.2, the methods are described, including a parameterization based on a temperature nudging concept, the preparation of the model domain, and the calculation of the UHI. In Section 4.3, the simulation results are discussed, with a particular focus on the influence of nudging on the wind and temperature fields and on the canopy UHI intensity. Finally, Section 4.4 presents the conclusion.

4.2. Methods

4.2.1. Parameterization method

The study by Cheng et al. (2023) shows that nudging can be used to parameterize relevant effects of buildings on airflows within the urban canopy layer. Following that, in addition to the wind nudging, a temperature nudging approach is used to parameterize urban effects on temperature fields. The parameterization is implemented in the mesoscale model METRAS. For temperature nudging, a nudging term is added to the right-hand side of the prognostic equation for potential temperature as follows:

$$\begin{aligned}\frac{\partial \rho_0 \alpha^* \bar{\theta}}{\partial t} = & \underbrace{-\frac{\partial}{\partial x}\left(\bar{u}\rho_0\alpha^*\bar{\theta}\right) - \frac{\partial}{\partial y}\left(\bar{v}\rho_0\alpha^*\bar{\theta}\right) - \frac{\partial}{\partial z}\left(\bar{w}\rho_0\alpha^*\bar{\theta}\right)}_{\text{Advection}} \\ & \underbrace{+\frac{\partial}{\partial x}\left[\rho_0\alpha^* K_{hm}\left(\frac{\partial\bar{\theta}}{\partial x} - \Gamma_\theta\right)\right] + \frac{\partial}{\partial y}\left[\rho_0\alpha^* K_{hm}\left(\frac{\partial\bar{\theta}}{\partial y} - \Gamma_\theta\right)\right] + \frac{\partial}{\partial z}\left[\rho_0\alpha^* K_{vm}\left(\frac{\partial\bar{\theta}}{\partial z} - \Gamma_\theta\right)\right]}_{\text{Force by turbulent fluxes}} \\ & \underbrace{+\rho_0\alpha^*\bar{Q}}_{\text{Sink/Source related to phase changes}} \\ & \underbrace{-\mathcal{W}(x,y,z)\,\delta\rho_0\alpha^*\left(\bar{\theta} - \bar{\theta_n}\right)}_{\text{Nudging term}}\end{aligned} \tag{4.2.1}$$

where $\bar{\theta}$ is the Reynolds-averaged potential temperature, $\overline{u}$, $\overline{v}$, and $\overline{w}$ are the Reynolds-averaged wind velocity components in the Cartesian coordinates, ρ_0 is basic state part of density, α^* is the grid volume. K_{hm} and K_{vm} are the horizontal and vertical heat

exchange coefficients, respectively. Γ_θ is the potential temperature counter-gradient term. The term $\rho_0 \alpha^* \bar{Q}$ associated with the additional source or sink related to phase changes, specifically latent heat release or absorption due to condensation or evaporation processes. The last term is the nudging term. $\bar{\theta}_n$ is the nudged temperature, $\mathcal{W}(x, y, z)$ is the weighting function (non-dimensional), and δ is the nudging coefficient (s^{-1}). As mentioned in Section 3.2.3, the nudging coefficient δ is an important parameter that affects the nudging efficiency. It should be set within a reasonable range in order to capture the proper urban thermal effect while avoiding too strong nudging. In this chapter, the nudging coefficient is set to $5x10^{-3}$ s^{-1}, corresponding to a time scale of several minutes as seen in the canopy simulations of Schlünzen et al. (2011) (Figure 4). The building surface fraction is set to the weighting function $\mathcal{W}(x, y, z)$ as given in Equation 3.2.4.

The nudging term in Equation 4.2.1 is defined as a sink or source depending on the relationship between the nudged temperature $\bar{\theta}_n$ and the potential temperature $\bar{\theta}$ of the atmosphere. If $\bar{\theta}$ is greater than $\bar{\theta}_n$, the nudging term acts as a sink, and if $\bar{\theta}$ is less than $\bar{\theta}_n$, the nudging term acts as a source.

An indoor temperature T_{indoor} is introduced as forcing data for the nudging parameterization. A relationship between the prescribed indoor temperature T_{indoor} and the corresponding nudged potential temperature $\bar{\theta}_n$ is given as follows:

$$\bar{\theta}_n = T_{indoor} \left(\frac{1000 \cdot 10^2 Pa}{p} \right)^{R/c_p} \tag{4.2.2}$$

where p is the pressure, R is the gas constant of air, and C_P is the specific heat at constant pressure.

In this chapter, wind nudging and temperature nudging are first carried out separately and then combined. Information on the code workflow for the combined wind and temperature nudging approach in METRAS is summarized in Figure A.1 in Appendix A.

4.2.2. Model domain

Study area

The city of Hamburg was chosen for the case study. Hamburg is the second largest city in Germany, with a population of over 1.8 million and an area of approximately 755 km^2. It is located in the northern part of Germany, on the River Elbe, and between the North Sea and the Baltic Sea. Thus, the city has a maritime climate influenced by the Elbe River. The land use in Hamburg is mainly composed of urban areas (residential, commercial, and industrial areas), rural areas (farmland, pastures, green spaces, parks, and forests), and water areas (the Alster and Elbe rivers, as well as numerous canals).

Orography and surface land cover

The model requires information about geographic location, orography, surface cover, as well as building height and building surface fraction for the study region. The model domain of this study covers the state of Hamburg, from about 53.3 °N to 53.7 °N and from about 9.7°E to 10.3°E. It has a dimension of 94 x 80 grid cells with a horizontal resolution of 500 m, corresponding to an area of 47 x 40 km^2. 34 levels are used in the vertical direction, with a top of above 10 km and a lowest atmospheric grid cell of 10 m above ground level. The vertical resolution is 20 m up to a height of 60 m above ground level. Above that level the grid spacing increases with a constant stretching factor of up to 1.175 per grid cell. The maximum resolution is 500 m and is used above 2800 m.

Figure 4.1 (a) shows the spatial variations of terrain height, with the maximum terrain height of 150.1 m located in the south-west of the state and an average terrain height value of 25.73 m. For creating a model grid with subgrid-scale surface cover classes, the LBM-DE2012 dataset (BKG, 2012) was used and processed to fit to the surface covers used in METRAS. A detailed description of the conversion from LBM-DE2012 to the surface cover classes used in METRAS is given in Schlünzen et al. (2019). Figure 4.1 (b) and (c) show the fraction of water and urban land cover distribution of the model domain per grid cell, respectively. Water surfaces include three METRAS surface cover classes: water (no further specification available), stationary fresh water (e.g. lakes), dynamic fresh water (e.g. rivers). Urban surfaces include seven classes: sealed urban, sparse sealed urban, compact sealed urban, asphalt, concrete, brick/pavers, and steel. Values for land cover dependent physical parameters such as thermal diffusivity, thermal conductivity, soil water availability, etc. are given in Schlünzen et al. (2012).

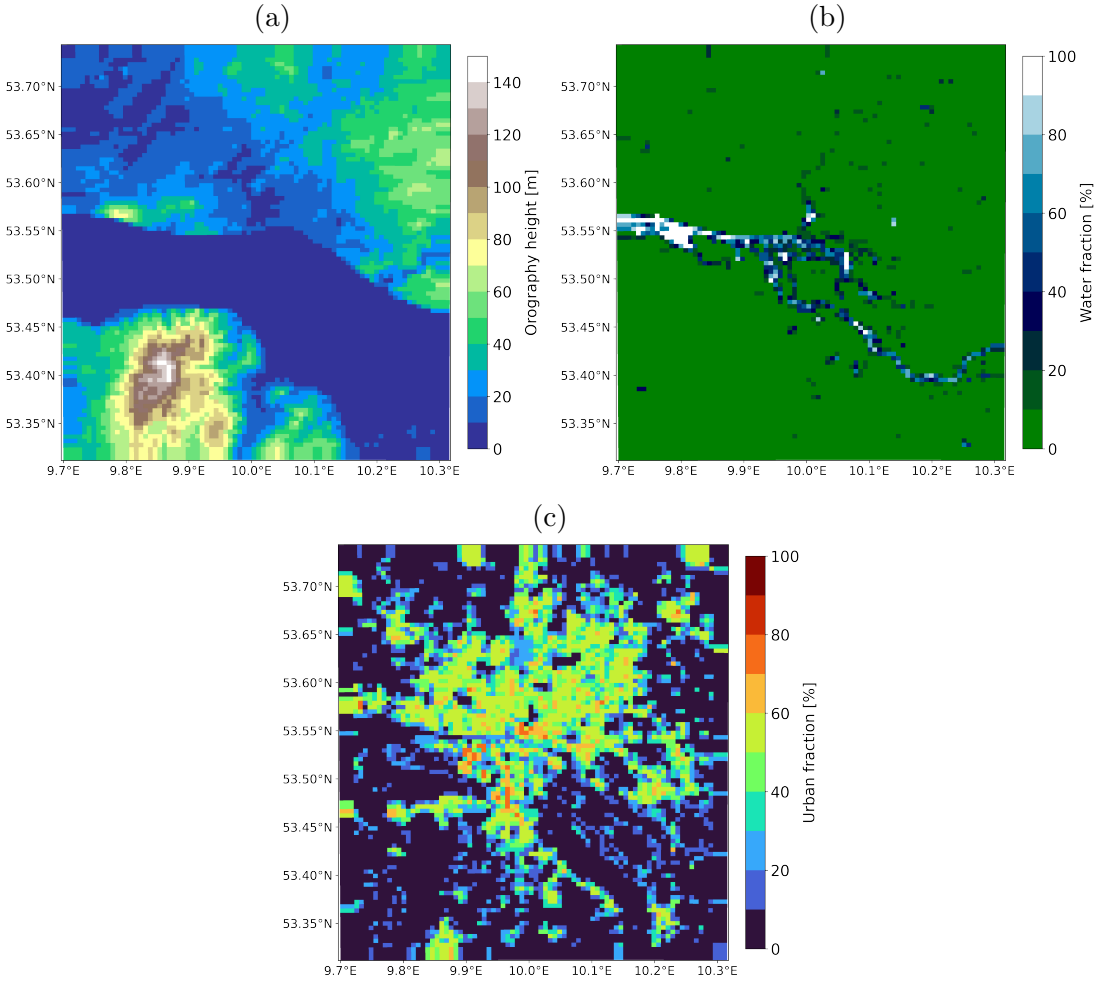

Figure 4.1.: Model domain showing (a) orography, (b) subgrid-scale water fractions within each grid cell, and (c) subgrid-scale urban land cover fractions within each grid cell

Building height and building surface fraction

For implementing the parameterization, building height and building surface fraction for each grid cell are required as the input information. In this case, Level of Detail 1 (LoD1, BKG (2020)) data was used. The LoD1 data is a 3D building model that represents the buildings in a simplified form as blocks, without taking into account the actual shape of roofs. LoD1 was chosen for three main advantages: 1) it covers the entire area of Hamburg (approx. 750 km^2) and contains detailed information about the position, size, and height of around 360,000 buildings inside this area; 2) it has a resolution of 1 m and a height accuracy of 5 m, which are fine enough for the mesoscale modelling; 3) it was newly updated in 2021, thus representing the actual building pattern for Hamburg.

LoD1 is first converted into a standard ASCII grid format using the software Saga-GIS (Conrad et al., 2015) and the pre-processor Gritop (Grawe and Schlünzen, 2018; Schlünzen and Grawe, 2018) is used to import the output data. A workflow for the data processing is shown in Figure C.1 in the Appendix C. Gritop is used to calculate the average building height and building surface fraction for each grid cell. The algorithms used to calculate the average building height are similar to those used to calculate the average terrain height in Gritop. Assuming that each grid cell consists of $M \times M$ subgrid cells with building height values (Figure 4.2), the average building height can be calculated by summing the building heights of all subgrid cells and dividing by the total number of subgrid cells $M \times M$. To avoid the influence of extremely tall buildings (e.g. TV towers, church steeples) on the average building values for some grid cells, subgrid cells with a building height value of zero are also included in the average calculation.

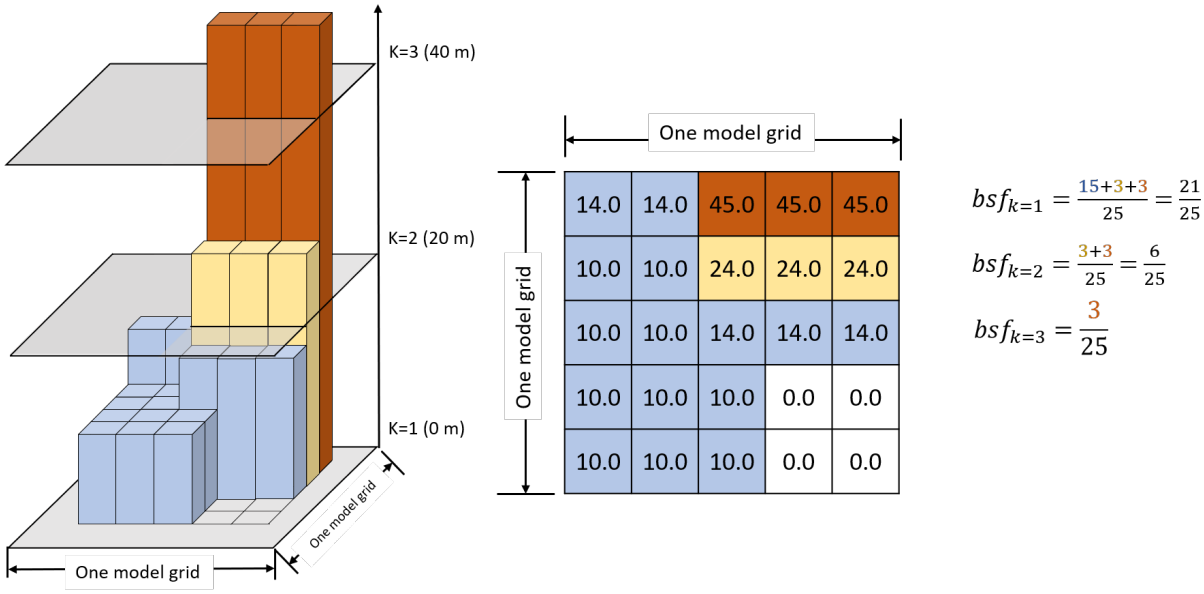

Figure 4.2.: An example of calculating the building surface fraction of a model grid. The model grid is composed of 5x5 subgrid cells, each of which has a building height value listed in the matrix. The calculation of the building surface fraction (bsf) at each model level (k=1, 2, 3) is shown on the right-hand side of the figure

The building surface fraction (bsf) of a model grid cell is calculated by dividing the number of subgrid cells with a building height value greater than the model vertical level height by the total number of subgrid cells $M \times M$. For example, the second model level has a height between 20 m and 40 m, so the subgrid cells with building heights greater than 20 m are counted to calculate the bsf at the second model level ($bsf_{k=2}$). An example

of calculating bsf for a model grid is shown in Figure 4.2.

Figure 4.3 shows the spatial pattern of the averaged building height and building surface fraction of each grid cell at the first level for the model domain (the bsf patterns at the second and third model levels are shown in Figure C.2 in Appendix C). It can be seen that tall and dense buildings are located in the city center, surrounding the Alster Lake. In the city center, the averaged building height and building surface fraction can reach up to 11.93 m and 41%, respectively.

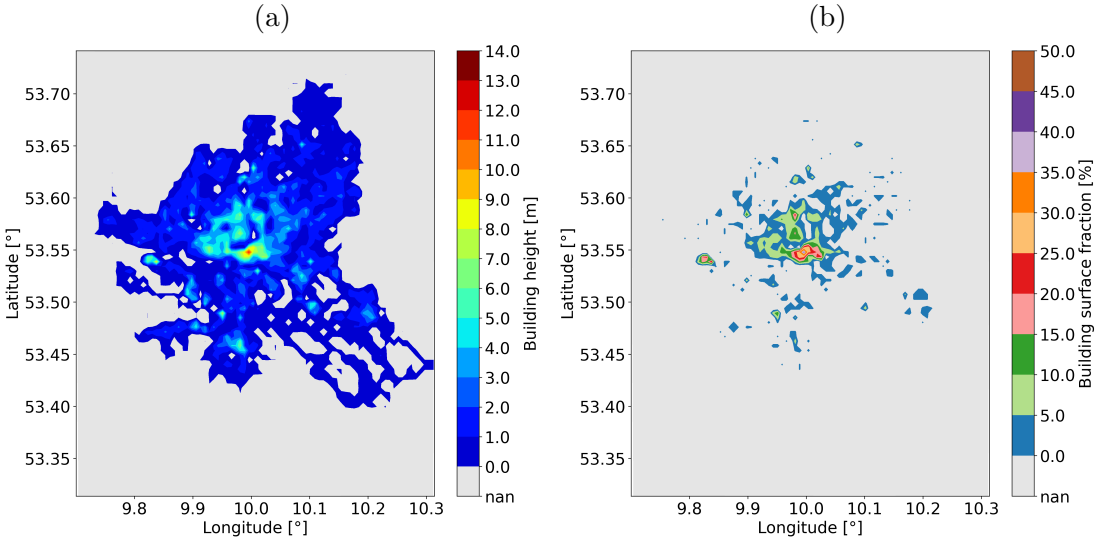

Figure 4.3.: Model domain showing (a) building height and (b) building surface fraction for each grid cell

4.2.3. Model set-up and meteorological conditions

The effects of wind nudging and temperature nudging on the wind and temperature fields are investigated for different meteorological conditions. The input values for meteorological parameters are listed in Table 4.1. The simulations start at 23:50 Local Standard Time (LST) on 15 July 2022, and the date represents for an average summer. The observed daily-averaged soil temperature at 50 cm depth for the summer of 2022 for the state of Hamburg is used to set the input ambient temperature at the surface, the soil temperature, as well as the water temperature. To largely prevent cloud formation or rain development in the beginning phase of simulations, the following model adjustments have been made: i) relative humidity at the surface is set to 50 %; ii) stratification is set to neutral below 1000 m and stable above 1000 m; iii) the number of rainless days is set to 7.

Table 4.1.: Values of input parameters for the simulations

Parameter	**Values**
Ambient temperature at the surface	18.8 °C
Ambient potential temperature gradient	0.0 K/m (from 0 to 1000 m) 0.0035 K/m (above 1000 m)
Wind direction	270°
Wind speed at 10 m above ground level	1.5 m/s, 3.0 m/s, 4.5 m/s, and 6 m/s
Water and soil temperature	18.8 °C
Relative humidity at the surface	50 %

For the wind nudging simulations, four values of wind speeds at 10 m above ground level (AGL) were set in order to investigate the nudging effects under different ambient wind conditions (Table 4.1). These wind speeds are part of the case names used in the following sections:

- wvl: wind nudging with a very low wind speed of 1.5 m/s at 10 m AGL
- wlm: wind nudging with a low middle wind speed of 3.0 m/s at 10 m AGL
- wmh: wind nudging with a middle high wind speed of 4.5 m/s at 10 m AGL
- wvh: wind nudging with a very high wind speed of 6.0 m/s at 10 m AGL

Three groups of runs were conducted with wind nudging (Table 4.2). The *a*- group (*awvl*, *awlm*, *awmh*, *awvh*) only used wind nudging and did not calculate temperature, relative humidity, cloud or rain, thus it can be used to analyze pure aerodynamic effects. For the *b*- group (*bwvl*, *bwlm*, *bwmh*, *bwvh*) all the parameters mentioned above were calculated, but without diurnal cycles. The *c*- group (*cwvl*, *cwlm*, *cwmh*, *cwvh*) calculated all the parameters with diurnal cycles. For each experiment run within the *a*-, *b*- and *c*- groups, a corresponding reference run was conducted with the same model set-up and meteorological conditions, but without nudging.

For the temperature nudging simulations, indoor temperatures were set at 18 °C, 20 °C, 22 °C, and 24 °C to investigate the relationship between indoor temperature and UHI. The wind speeds in all cases were set to 3.0 m/s (*lm*). For the *at*- group (*t* for temperature nudging, *atlm18*, *atlm20*, *atlm22*, *atlm24*), only temperature nudging was performed. For the *ab*- group (*b* for both nudging, *ablm18*, *ablm20*, *ablm22*, *ablm24*), both wind and temperature were nudged (Table 4.2). For both *at*- and *ab*- groups, all parameters were calculated with diurnal cycle. Each case was also simulated with and without the nudging (Table 4.2).

Table 4.2.: Model set-up for each simulation. ff_{10m} for the ambient wind speeds at 10 m above ground level. T_{indoor} for the indoor temperature, which is also the nudged temperature. ntemp, nqv, nqlc, and nqlr for calculation of temperature, relative humidity, cloud, and rain

No.	**Case ID**	**Wind nudging**	**Temp nudging**	ff_{10m} **[m/s]**	T_{indoor} **[°C]**	**ntemp, nqv nqlc, nqlr**	**Diurnal cycle**
1	awvl	Yes	No	1.5	No	No	No
2	awlm	Yes	No	3.0	No	No	No
3	awmh	Yes	No	4.5	No	No	No
4	awvh	Yes	No	6.0	No	No	No
5	bwvl	Yes	No	1.5	No	Yes	No
6	bwlm	Yes	No	3.0	No	Yes	No
7	bwmh	Yes	No	4.5	No	Yes	No
8	bwvh	Yes	No	6.0	No	Yes	No
9	cwvl	Yes	No	1.5	No	Yes	Yes
10	cwlm	Yes	No	3.0	No	Yes	Yes
11	cwmh	Yes	No	4.5	No	Yes	Yes
12	cwvh	Yes	No	6.0	No	Yes	Yes
13	atlm18	No	Yes	3.0	18	Yes	Yes
14	atlm20	No	Yes	3.0	20	Yes	Yes
15	atlm22	No	Yes	3.0	22	Yes	Yes
16	atlm24	No	Yes	3.0	24	Yes	Yes
17	ablm18	Yes	Yes	3.0	18	Yes	Yes
18	ablm20	Yes	Yes	3.0	20	Yes	Yes
19	ablm22	Yes	Yes	3.0	22	Yes	Yes
20	ablm24	Yes	Yes	3.0	24	Yes	Yes

4.2.4. Calculation of urban heat island

The urban heat islands (UHI) of a city can be calculated using both observation- and modeling-based approaches. In observation studies, the UHI can be determined by subtracting the rural temperature from the urban temperature (e.g. Schlünzen et al., 2010) or by subtracting the large-scale air temperature from the urban spatial temperature (e.g. Kirsch et al., 2022). Schlünzen et al. (2010) analyzed data from up to 7 sites located throughout the metropolitan area of Hamburg and demonstrated that the UHI intensity is up to 3 K in summer (climate average) and highly dependent on local impacts. They reported that the climate average value for the UHI is 1.1 K in densely populated and green-poor areas, and 0.6 K in less densely populated or river-influenced areas (Schlünzen et al., 2010). Kirsch et al. (2022) investigated the UHI of Hamburg through a sub-mesoscale measurement campaign, involving 103 meteorological ground-based stations that covered both the city center and its rural surroundings. The temporal development and spatial structure of the nocturnal UHI of Hamburg was well captured by this dense network of stations. It was found that the nocturnal UHI of Hamburg in summer (June to August, 2020) had a maximum magnitude of over 3 K, with the highest intensity between 21:00 and 03:00 UTC (Kirsch et al., 2022).

Model studies generally employ two methods to calculate the UHI (Hoffmann et al., 2018). The first is to conduct two simulations - one with urban land use and one without - and subtract the results from each other(Hoffmann et al., 2018). The second approach is to subtract the temperature at rural grid points from the whole temperature field. Following the second approach, Hoffmann et al. (2012) constructed a regression-based statistical model and found that the UHI for Hamburg depends on wind speed, cloud cover and relative humidity.

To investigate UHI effects, this study follows the second modelling approach mentioned above. The UHI intensity ($UHII$) is defined as the temperature difference between urban areas (T_{urban}) and the surrounding rural areas (T_{rural}):

$$UHII = T_{urban} - T_{rural} \tag{4.2.3}$$

To determine T_{urban} and T_{rural}, the mean temperature of all urban grid cells and all rural grid cells are calculated, respectively:

$$UHII = \frac{1}{M}\sum_{i=1}^{M} T_{urban,i} - \frac{1}{N}\sum_{j=1}^{N} T_{rural,j}, \tag{4.2.4}$$

where i and j are the indices for urban and rural grid cell, M and N are the number of urban and rural grid cells, respectively.

For selecting the grid cells that represent urban and rural areas, the criterion defined by Böttcher (2017) has been used. First, to exclude altitude effects, only grid cells with an orography height between 0 and 30 m are considered (Figure 4.1a). Secondly, as water has a damping effect on the temperature development, grid cells that are partially or totally covered by water classes are excluded from the analysis (Figure 4.1b). Thirdly, urban areas are defined as those within a 10-kilometer radius of the Hamburg city center, while areas within a radius of 10-20 kilometers are considered rural. Within the inner ring (radius $\leq$ 10 km), grid cells with a subgrid-scale urban fraction above 50% are defined as urban grids (Figure 4.1c), while rural grids are characterized by areas within the outer ring (10 km $<$ radius $\leq$ 20 km) that has a subgrid-scale urban fraction equal to zero. Figure 4.4 shows the spatial distribution of grid cells representing urban and rural areas within the model domain. Note that many cells in the North West and South East are not included because their altitude is above 30 m (selection criterion 1). Furthermore, grid points close to water bodies are left out (criterion 2).

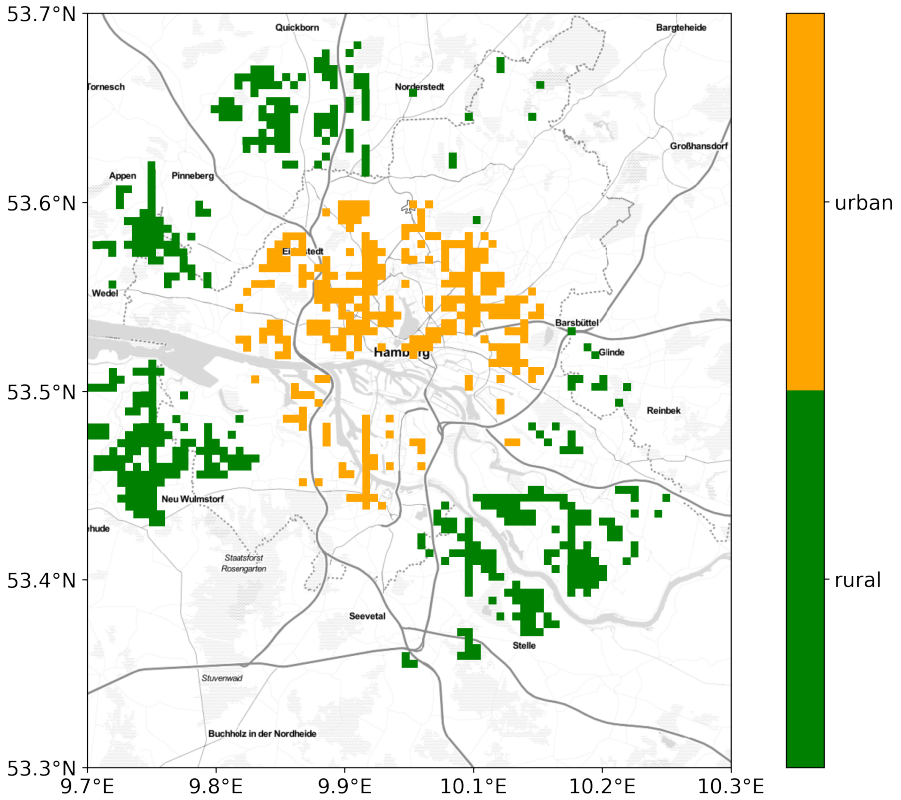

Figure 4.4.: Grid cells represent for urban (yellow) and rural (green) areas.

4.3. Results and discussions

METRAS employs an implicit urban parameterization, which assigns different values to dynamic and thermodynamic properties (e.g. roughness length, albedo, and thermal diffusivity) for various surface cover classes. Previous studies have demonstrated that METRAS with the implicit parameterization well captures the UHI effect (Hoffmann et al., 2018). The focus of this section is to investigate the impact of the additional parameterization using the extended nudging approach on the previously simulated UHI effect, in particular to assess whether the parameterization enhances or diminishes the effect. In addition, possible urban effects on the wind fields are investigated.

The simulations start at 23:50 LST and run for three days. The first nine hours are considered a model spin-up period, so the output from this time period is not used for analysis. To analyze the nudging effects, the differences between the nudging and the reference runs are calculated and then averaged for day- and night-time. The difference is always calculated by subtracting the reference values from the nudging values. As sunrise and sunset on 15 July 2022 are at 04:12 and 20:39, respectively, daytime is defined in this chapter as the period from 09:00 to 17:00 LST on 16 July 2022, while nighttime is defined as the period from 21:00 LST on 16 July 2022 to 04:00 LST on 17 July 2022.

For all cases sooner or later clouds form (Table 4.3 and Figures D.1-D.3 in Appendix D), disturbing the "ideal signal" of changes in the flow and temperature field. This "ideal signal" is normally discussed for cloud-free situations, where surface or canopy induced influences on the wind and temperature field are best visible. Earliest cloud formation begins in the cases discussed here at 16:32:54, 2022-07-16, with rain occurring about four hours later (case *cwvh*). Model output after this time is influenced by cloud effects. Only model outputs for the daytime are hardly influenced by clouds (except case *cwvh* for ~30 minutes). This time interval is defined as "daytime" in the further analyses, later days are not analysed to avoid cloud and rain influences. For the nighttime, after 21:00 LST, all cases except the cases of the *a-* group, *bwvl*, *bwlm*, *bwmh* (including their reference cases), and *cwmh* have cloud influences (Table 4.3). Table 4.3 also shows the percentage of periods with cloud influence over the entire analysis period.

Table 4.3.: Summary of the first time point for rain and cloud formation from the model output, and percentage of "cloudy" time over the entire analysis period. Simulations start on 2022-07-15 23:50:00 LST. CF_day and CF_night denote the cloud fraction for the analyzed daytime period (from 09:00 to 17:00 LST on 2022-07-16) and the analyzed nighttime period (from 21:00 LST on 2022-07-16 to 04:00 LST on 2022-07-17), respectively. Cases that remained cloud-free and rain-free throughout the analysis period are indicated by boldface in their cases names. Cases that were cloud- and rain-free only for the analyzed daytime are indicated in italics.

Case ID	Date and time (LST) for rain formation	Date and time (LST) for cloud formation	CF_day (%)	CF_night (%)
bwvl	none	none	0	0
bwlm	none	none	0	0
bwmh	2022-07-18 13:17:10	2022-07-17 19:19:40	0	0
bwvh	2022-07-16 22:00:06	2022-07-16 20:06:06	0	100
bwvl_ref	none	none	0	0
bwlm_ref	none	none	0	0
bwmh_ref	2022-07-17 23:52:22	2022-07-17 21:58:50	0	0
bwvh_ref	2022-07-16 21:53:22	2022-07-16 20:35:22	0	100
cwvl	2022-07-17 16:17:04	2022-07-16 17:01:40	0	100
cwlm	2022-07-17 01:08:20	2022-07-16 23:24:00	0	68
cwmh	2022-07-18 19:12:50	2022-07-17 14:16:39	0	0
cwvh	2022-07-16 20:44:10	2022-07-16 16:32:54	7	100
cwvl_ref	2022-07-17 14:19:54	2022-07-16 16:58:24	0	100
cwlm_ref	2022-07-17 00:15:50	2022-07-16 20:44:00	0	100
cwmh_ref	2022-07-17 18:35:42	2022-07-17 03:27:36	0	7
cwvh_ref	2022-07-16 20:44:10	2022-07-16 17:49:54	0	100
atlm18	2022-07-17 00:12:20	2022-07-16 20:47:00	0	100
atlm20	2022-07-17 00:24:40	2022-07-16 20:04:36	0	100
atlm22	2022-07-17 00:44:50	2022-07-16 19:39:24	0	100
atlm24	2022-07-17 01:07:00	2022-07-16 19:23:48	0	100
ablm18	2022-07-17 01:01:10	2022-07-16 23:17:00	0	67
ablm20	2022-07-17 01:56:50	2022-07-16 23:13:00	0	68
ablm22	2022-07-17 02:00:50	2022-07-17 00:28:40	0	49
ablm24	2022-07-17 00:46:20	2022-07-16 19:56:37	0	100

4.3.1. Wind nudging effects

To analyze the effect of wind nudging, the wind speed differences between the nudging and reference runs are focused.

Results for the *a* group

The *a* group does not calculate thermodynamic parameters such as temperature, relative humidity, cloud and rainwater, nor take into account the diurnal cycle. This means that *a* cases have idealized meteorological conditions and cannot accurately represent reality, but they can still be used to analyze the pure aerodynamic nudging effects. Figure 4.5 shows the spatial pattern of the wind speed difference between the nudging and reference simulations at 10 m AGL. It is clear that the greatest difference in wind speed between the nudging and reference cases appears in the building coverage area for all cases. Wind speeds within these areas are noticeably reduced, indicating that the wind-blocking effects of buildings are well represented using the nudging approach. And these effects can also be seen from 10 m to 70 m AGL in the model domain (not shown), where buildings extend vertically and nudging was applied.

As mentioned above, METRAS uses an implicit urban parameterization and thus urban areas, which are characterised by higher roughness length values compared to other land cover classes, experience a greater reduction in wind speed. Figure 4.6 shows the spatial pattern of these wind speed reductions due to the implicit urban parameterization for the references cases in the *a* group. The reduction was calculated by subtracting the ambient wind speed at 10 m AGL from the wind speeds at each grid point. Results indicate that higher ambient wind speeds lead to stronger wind reductions in urban areas for the city of Hamburg, except for the grid points located in the city centre which are covered by water bodies (with low roughness length values) such as the Binnenalster (Figure 4.6). For example, the urban grid cells (excluding water covered grids) for the *awvh* case with an ambient wind speed of 6.0 m/s experience a wind speed reduction of about 2.4 m/s (Figure 4.6d), while this reduction reaches only about 0.5 m/s for the urban grids for the *awvl* case with an ambient wind speed of 1.5 m/s (Figure 4.6a).

However, the additional nudging effect analyzed in this study is hardly dependent on the ambient wind speed at the surface, but is in addition to the implicit parameterization effects by roughness changes. Table 4.4 presents the maximum wind speed reduction due to the nudging effect at different vertical model levels. It can be seen that the maximum wind speed reduction hardly depends on the ambient wind speed; higher ambient wind

speeds result in slightly larger wind speed reductions. In addition, the wind reduction effects become weaker with increasing height. This is because there are fewer buildings and thus the value for the weighting function in the nudging term decreases with height. As diurnal cycles are not considered in this group of simulations, there are no differences between the day and night, as shown for cases *awvl* and *awlm* (Figure 4.5a-d). For cases *awmh* and *awvh*, gravity waves occur at upper model levels and wave energy propagates from upper to lower levels, causing variations in wind speeds and turbulence.

Results for the *b* group

The model simulations of the *b* groups calculate thermodynamic related parameters, such as temperature, relative humidity, cloud, and rain, in addition to wind, as done in the *a* group cases. Results in the *b* group also show the wind speeds reduction due to nudging, especially in building-covered areas (Figure 4.7). Since the diurnal cycle is not considered, there is little difference in wind speeds between the day- and night-time pattern for *bwvl* and *bwlm* cases (Figure 4.7a–d). Similar to cases *awmh* and *awvh*, the wind patterns for cases *bwmh* and *bwvh* are influenced by gravity waves. In addition, cloud and rain start to form for *bwvh* during nighttime (Table 4.3), which causes strong turbulence and intense vertical mixing. Similar to the *a* group cases, the wind speed reduction in the building covered areas due to nudging does not depend on the ambient wind speed (Table 4.4).

Results for the *c* group

The *c* group simulations consider thermodynamic-related parameters and diurnal cycle. Great differences between day- and night-time pattern can be seen in Figure 4.8. During the day, nudging effects can be clearly seen for all cases (Figure 4.8a, c, e, g). However, during the night, the nudging effects are strongly influenced by the presence of clouds and rain (Figure 4.8b, d, f, h). Rain formation occurs during the night in case *cwlm* and at around sunset in case *cwvh* cases, while cloud formation is seen in all *c*- cases except *cwmh* (Table 4.3). These cloud and rain formations have a notable impact on the results as they modify the incoming and outgoing radiative fluxes and influence vertical turbulent mixing, thereby affecting the wind and temperature fields.

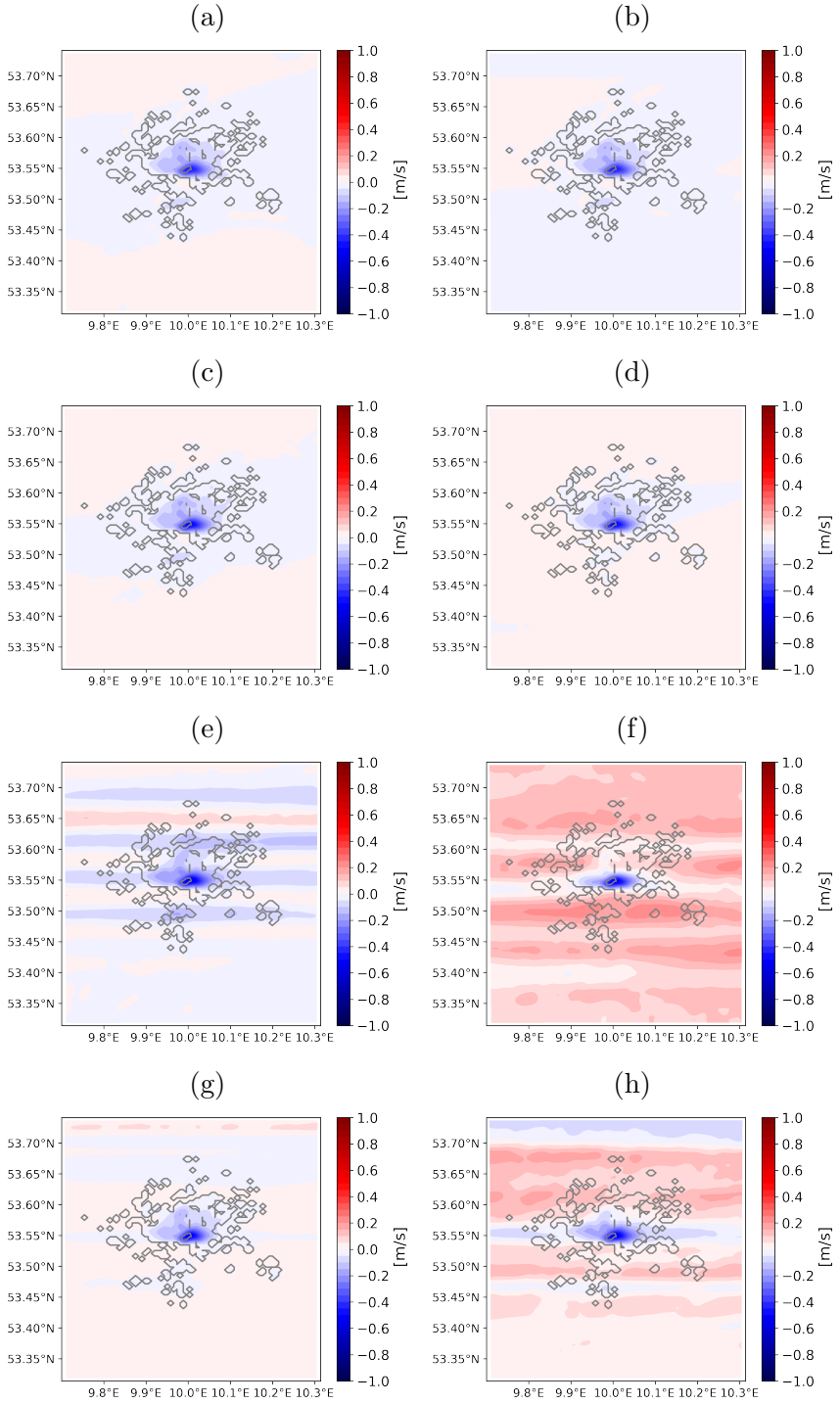

Figure 4.5.: The spatial pattern of the wind speed differences between the nudging and reference simulations at 10 m AGL for cases (a, b) *awvl*, (c, d) *awlm*, (e, f) *awmh* and (g, h) *awvh*. The left column shows the daytime averaged value and while the right column shows the nighttime averaged value. The building areas are marked with a grey contour line

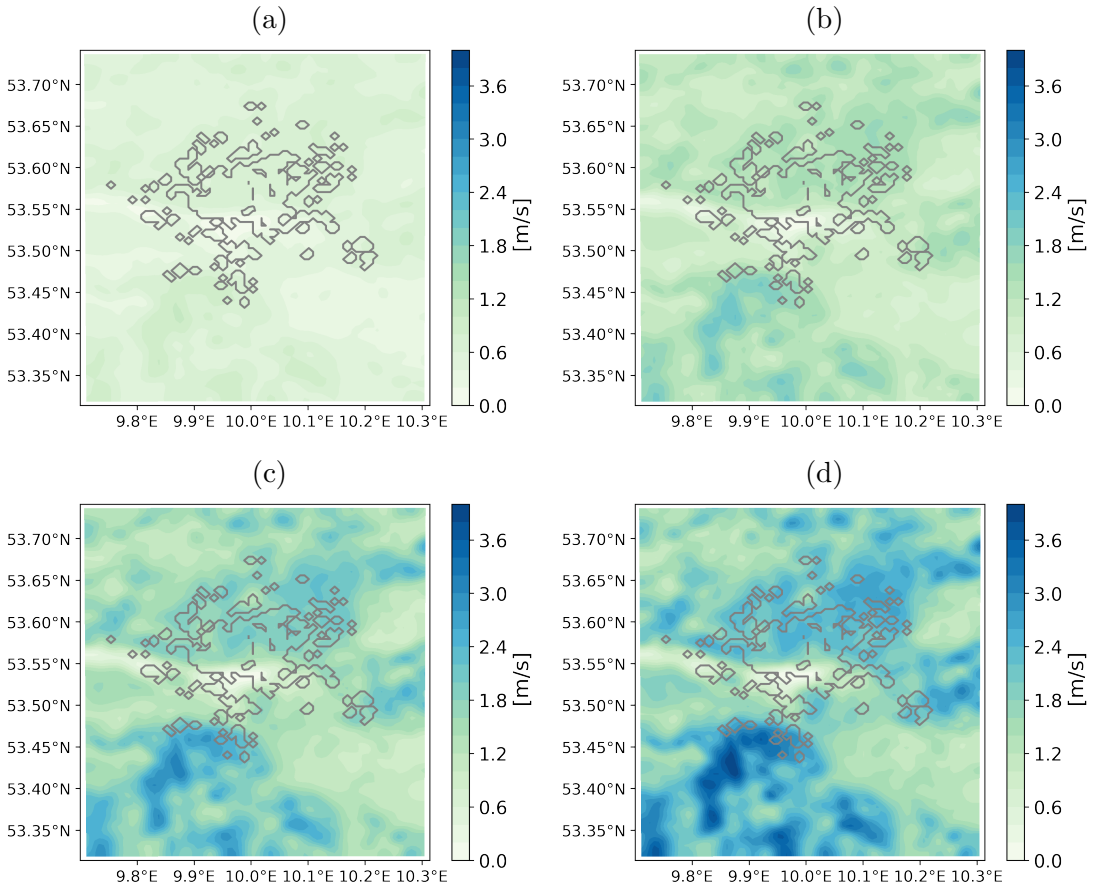

Figure 4.6.: The spatial pattern of the wind speed reductions at 10 m AGL for reference cases in *a* the group (a) *awvl*, (b) *awlm*, (c) *awmh*, and (d) *awvh*. The reduction was calculated by subtracting the ambient wind speed at 10 m AGL from the wind speeds at each grid points. Absolute values are averaged for the daytime. The building areas are marked with a grey contour line

Table 4.4.: The maximum magnitude of the wind speed difference between the nudging and reference simulation for wind nudging cases within the analyzed period from 9:00 to 21:00 LST. ff_{10m}, ff_{30m}, ff_{50m} and ff_{70m} indicate the value at 10 m high, 30 m high, 50 m high and 70 m above ground level, respectively.

Case ID	ff_{10m} [m/s]	ff_{30m} [m/s]	ff_{50m} [m/s]	ff_{70m} [m/s]
awvl	-0.46	-0.25	-0.19	-0.15
awlm	-0.52	-0.28	-0.21	-0.17
awmh	-0.56	-0.33	-0.26	-0.22
awvh	-0.49	-0.25	-0.17	-0.13
bwvl	-0.43	-0.22	-0.15	-0.11
bwlm	-0.52	-0.29	-0.22	-0.18
bwmh	-0.47	-0.20	-0.13	-0.07
bwvh	-0.56	-0.33	-0.27	-0.23
cwvl	-0.51	-0.18	-0.13	-0.07
cwlm	-0.52	-0.28	-0.30	-0.25
cwmh	-0.53	-0.36	-0.41	-0.45
cwvh	-0.47	-0.27	-0.24	-0.21

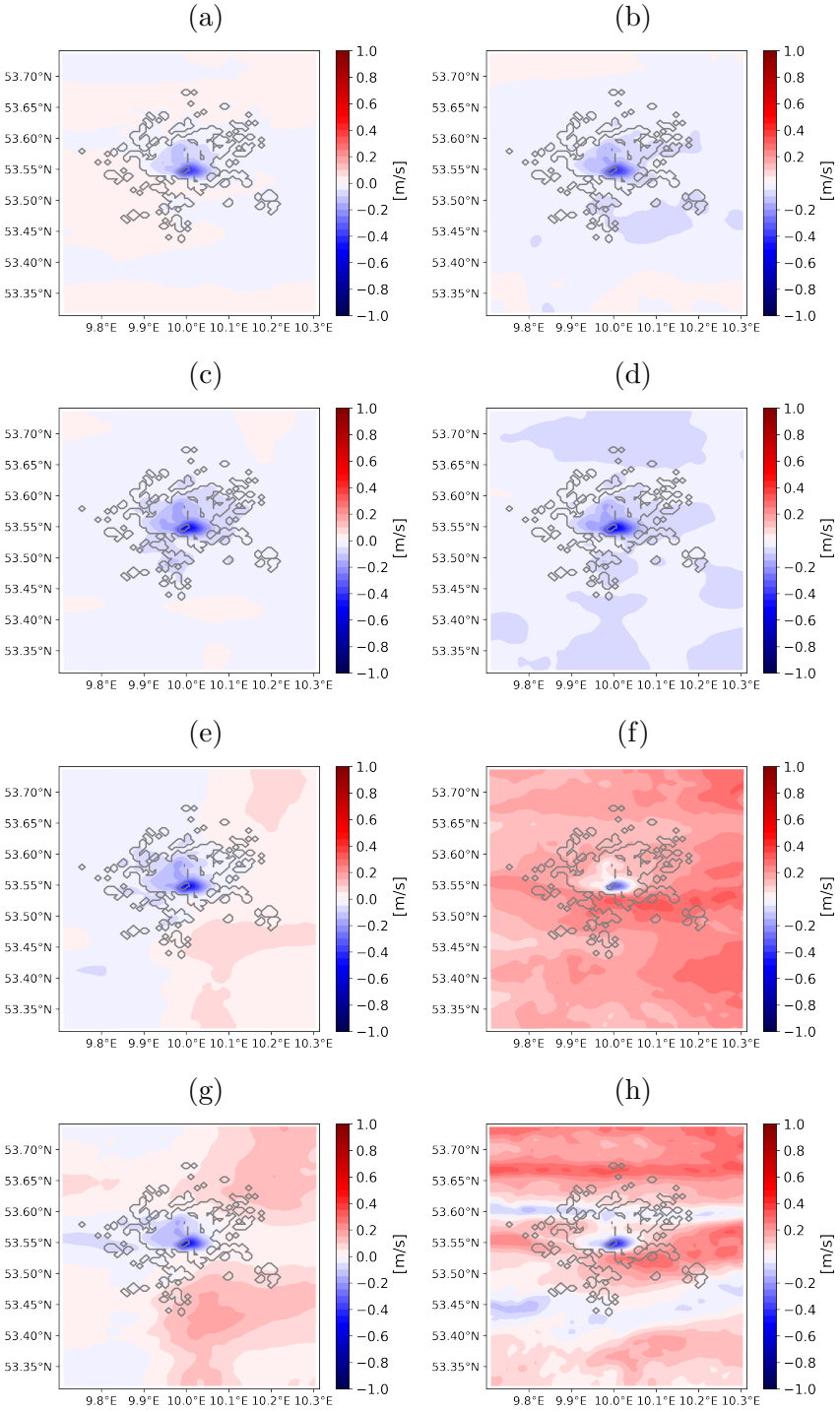

Figure 4.7.: Same as Figure 4.5, but for the *b* group cases (a, b) *bwvl*, (c, d) *bwlm*, (e, f) *bwmh* and (g, h) *bwvh*

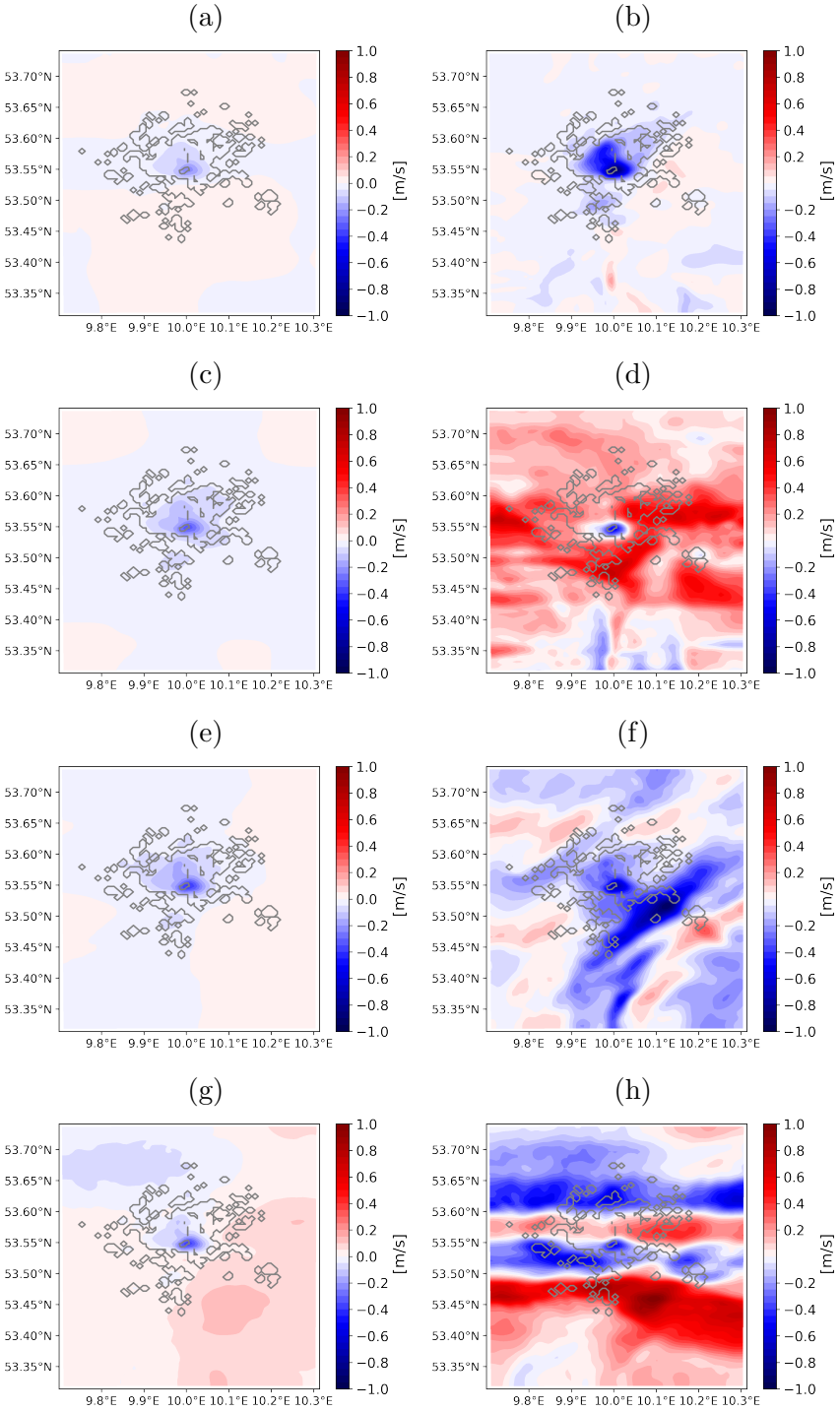

Figure 4.8.: Same as Figure 4.5, but for the *c* group cases(a, b) *cwvl*, (c, d) *cwlm*, (e, f) *cwmh* and (g, h) *cwvh*

4.3.2. Temperature nudging effects

For analyzing the effects of temperature nudging, the air temperature differences between the nudging runs and the reference run were calculated. The ambient wind speeds of all temperature nudging cases are 3.0 m/s, thus the case *cwlm_ref* was chosen as the reference run. Figure 4.9a and b show the day- and night-time mean spatial patterns of air temperature at 10 m AGL for the reference run *cwlm_ref*, and Figure 4.9c shows the diurnal cycle for the air temperature at 10 m AGL in urban and rural areas as defined in the Section 4.2.4. During the day, the air temperature follows an orography-based pattern, with higher-altitude locations being colder than lower-altitude areas closer (Figure 4.9a). During the night, the UHI effect is more pronounced than the orography effect, with air temperatures in urban areas being higher than in rural areas (Figure 4.9b and c).

Figure 4.10a and b show the spatial pattern of air temperature at 10 m AGL and the air temperature difference between the nudging and reference runs, respectively. During the day, cases *atlm22* and *atlm24* have higher indoor temperatures (T_{indoor}) than model air temperatures, resulting in a warming of the lower atmosphere, particularly in areas with high building coverage. This warming effect is also noticeable in the north-eastern parts of Hamburg, where heat is transferred by the westerly ambient winds. The strength of this effect depends on the difference between T_{indoor} and the model temperature T_{air}; greater differences result in stronger nudging and atmospheric heating effects. For example, a temperature increase in the city center for case *atlm24* reaches up to 0.46 K (Figure 4.11f), while for case *atlm22*, the magnitude is 0.25 K (Figure 4.11h). Conversely, case *atlm18* has higher T_{air} than T_{indoor}, resulting in a cooling effect with the maximum values of -0.18 K (Figure 4.11b). A slightly smaller increase was seen for case *atlm20* due to the smaller difference between T_{indoor} and T_{air} (Figure 4.11d). The nudging effects exist from the first to the third level, where buildings vertically extend (not shown).

During the night, compared to the reference case $cwlm\_ref$, an additional UHI phenomenon can be seen for cases *atlm20*, *atlm22*, and *atlm24* (Figure 4.11c, e, g). Compared to the daytime, the nudging has a stronger warming effect on the building-covered areas, as the difference between T_{indoor} and T_{air} further increases during the night (Figure 4.11d, f, h). However, for case *atlm18* the heat island was declined by the temperature nudging, i.e. the temperature nudging has a cooling effect on the atmosphere, resulting in a maximum temperature decrease of -0.57 K (Figure 4.11b). Figure 4.9b shows that the temperature difference between urban and rural areas for the reference case $cwlm\_ref$ is up to 1 K (greater than 0.57 K), thus an UHI remains for case *atlm18*, but the intensity is reduced.

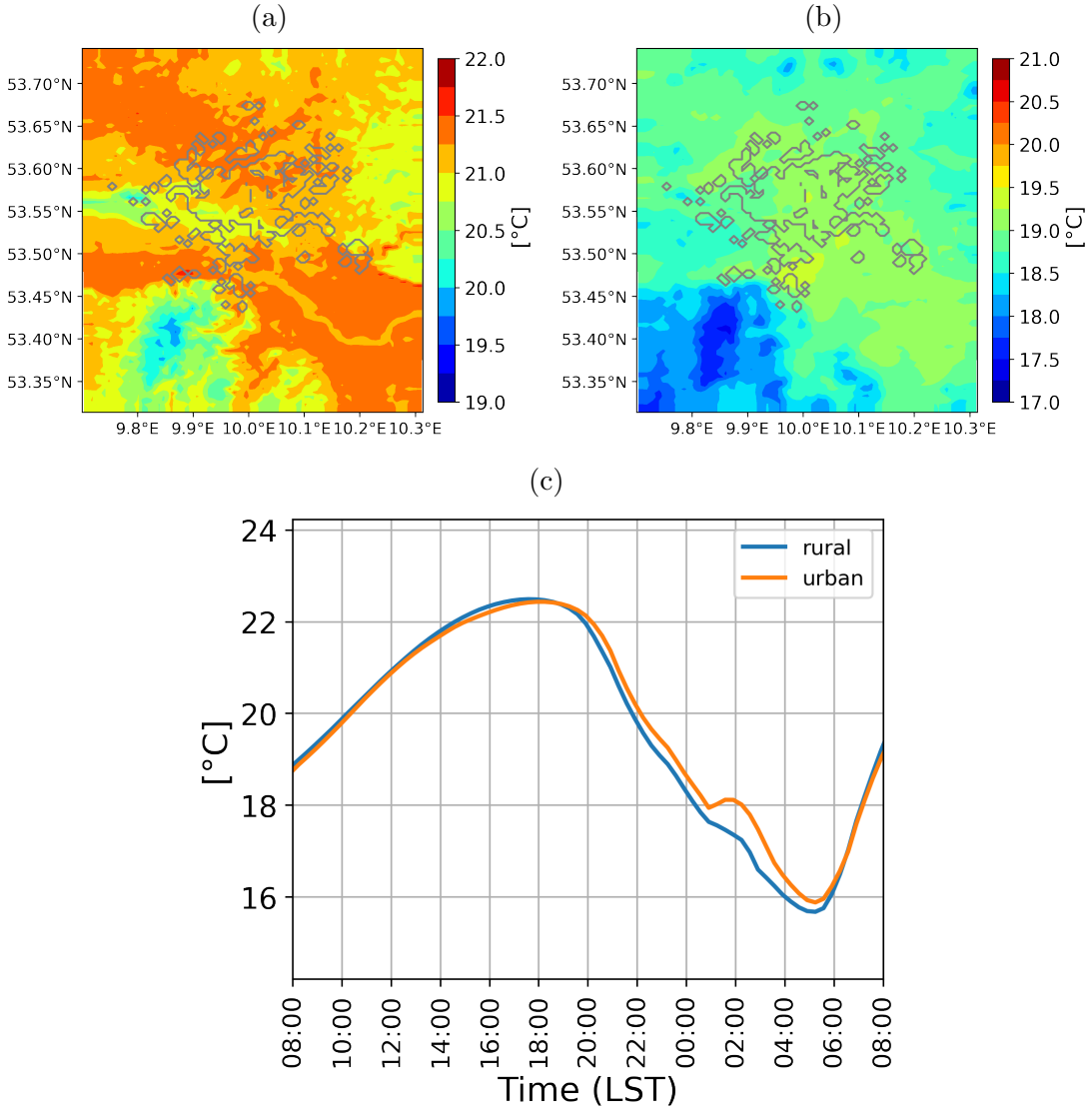

Figure 4.9.: (a) Daytime (09:00 to 17:00 LST), (b) nighttime (21:00 to 04:00 LST) mean spatial pattern of air temperature at 10 m AGL, and (c) time series of the mean air temperature at 10 m AGL in urban and rural areas for the reference case *cwlm_ref*. Note the different scalings for day- and night-time.

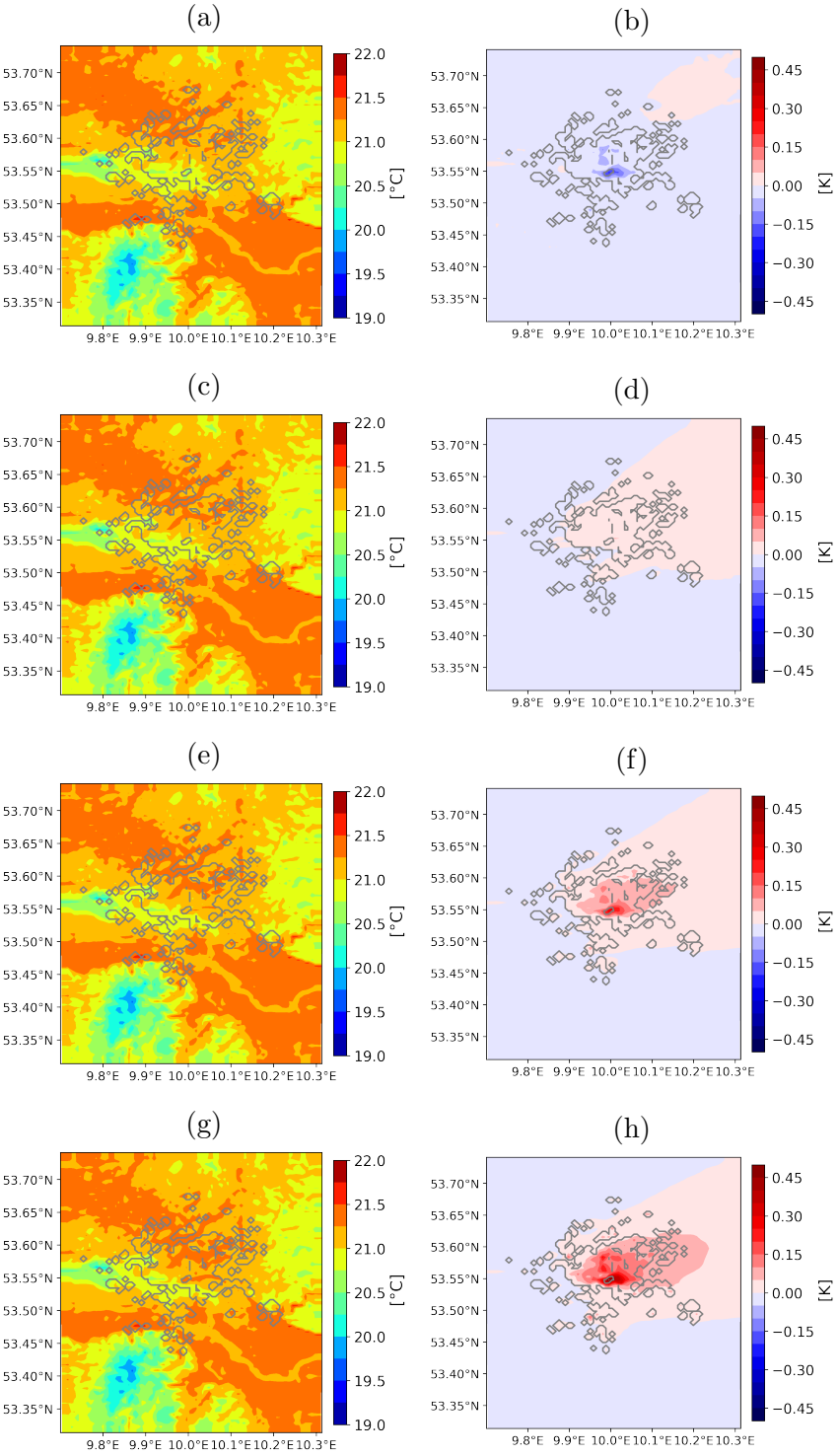

Figure 4.10.: Daytime (09:00 to 17:00 LST) mean spatial pattern of air temperature at 10 m AGL. The left column shows the air temperature for the temperature nudging case (a) *atlm18*, (c) *atlm20*, (e) *atlm22* and (g) *atlm24*. The right column shows the air temperature difference between the nudging and the reference run for the corresponding case (b) *atlm18*, (d) *atlm20*, (f) *atlm22* and (h) *atlm24*

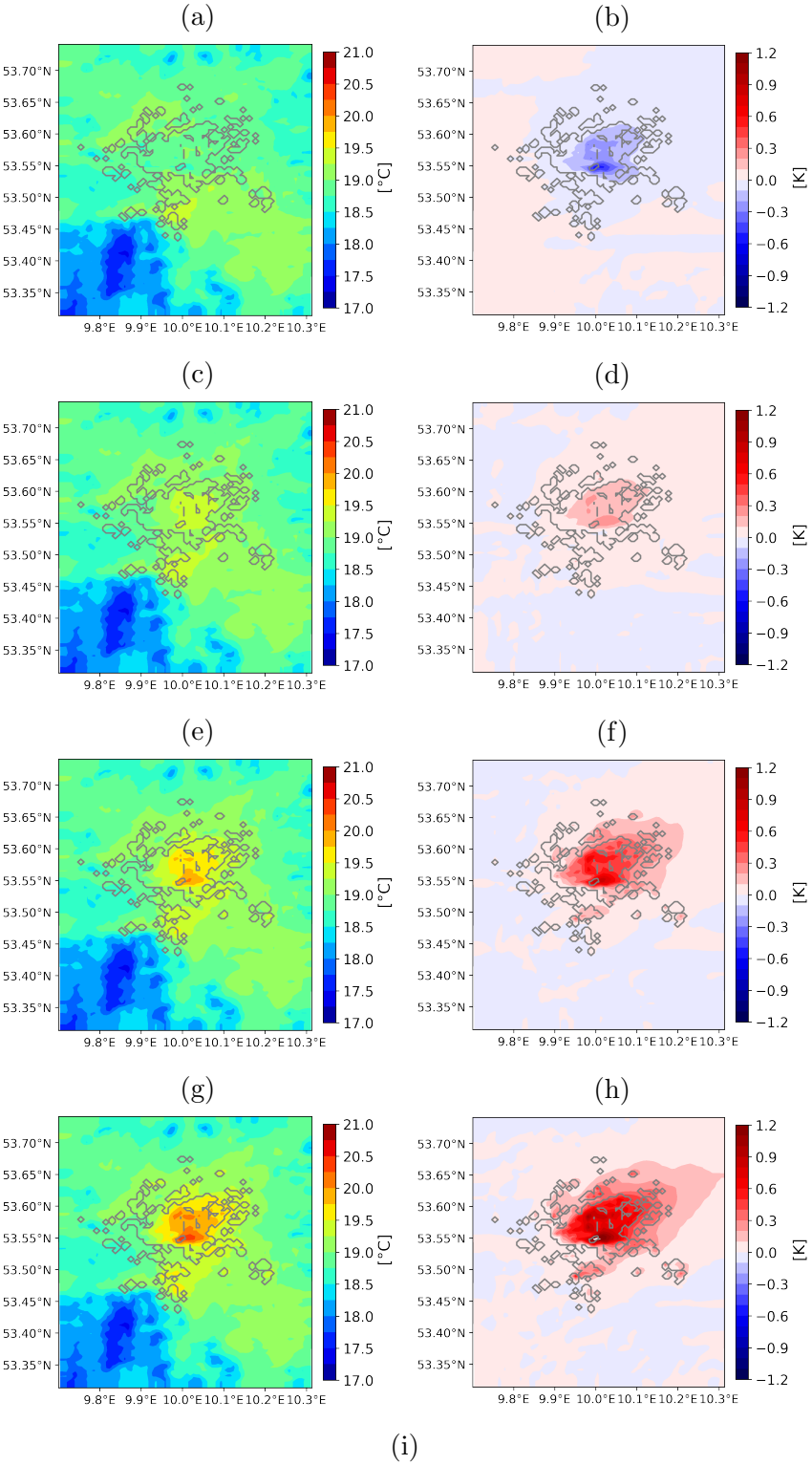

Figure 4.11.: Same as Figure 4.10 but for nighttime (21:00 to 04:00 LST).

4.3.3. Urban heat island intensity with wind and temperature nudging

The urban heat island intensity (UHII) is defined as the difference in mean air temperature at 10 m AGL between urban and rural areas (Section 4.2.4). Figure 4.12 shows the time series of UHII for all *c* cases, including nudging and reference simulations. The maximum value of UHII and its occurrence time for each case are listed in Table 4.5. It can be seen that all simulations show positive UHII from late afternoon to early morning of the next day, and UHII in most cases has a maximum between 00:15 and 02:55 LST, about three to five hours after sunset (Table 4.5). Negative values of the UHII were simulated after 06:00 LST in the morning (Figure 4.12), as suggested by Oke (1987) that an urban cool island can develop in the morning hours.

Compared to the reference cases, all wind nudging cases except the *cwvh* have higher UHII maximum values, implying that the wind nudging enhances the UHI effect (Table 4.5). This is because the reduced wind speed due to nudging alters the vertical heat fluxes and more heat remains near the surface, leading to a higher UHII. Conversely, higher wind speeds help to disperse the heat stored in the materials used in urban structures and increase vertical exchange as well as urban-rural mixing, thus restricting the development of UHI. Case *cwvh* has lower a UHII than $cwvh\_ref$, a reason for this could be that more cloud water content was simulated in *cwvh* than $cwvh\_ref$ (Figure D.1 in Appendix D), and UHII is influenced by cloud and rain formation, as suggested by Morris et al. (2001); Hoffmann et al. (2012). An increase in the amount of cloud cover can result in a reduction in the UHI magnitude. In addition, cloud distribution also plays an important role in the development of the UHI, as the incoming radiation during the day and the outgoing radiation at the nighttime over urban areas are affected by cloud cover.

Figure 4.13 shows that higher indoor temperatures result in stronger UHII and the temperature nudging effects on the UHII depend on the difference between T_air and T_indoor, as explained in Section 4.3.2. In addition, all *ab-* cases (both wind and temperature nudging implemented) have higher UHII values than *at-* cases (only temperature nudging implemented), which also indicates that wind nudging helps to enhance the UHI intensity.

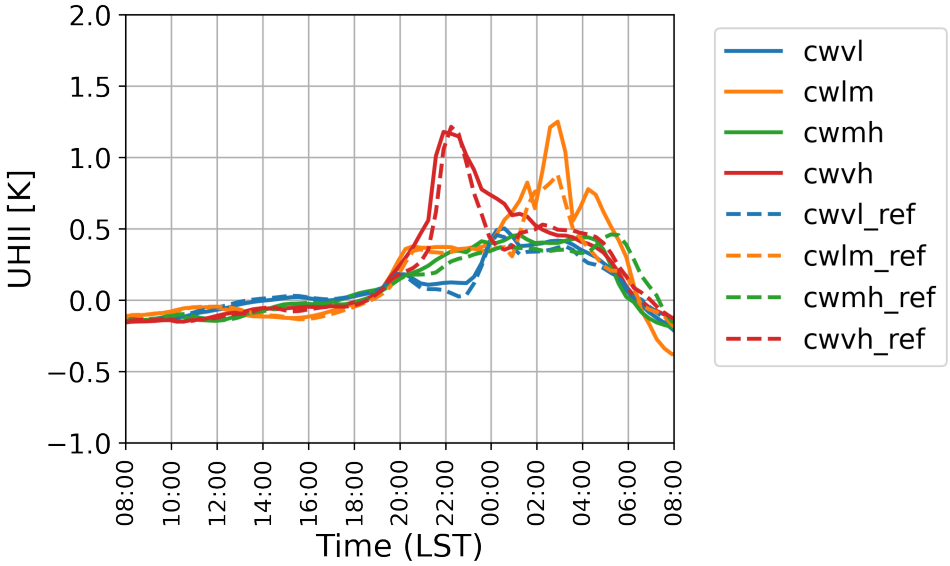

Figure 4.12.: Time series of the urban heat island intensity of the wind nudging c group cases and reference cases ($\_ref$)

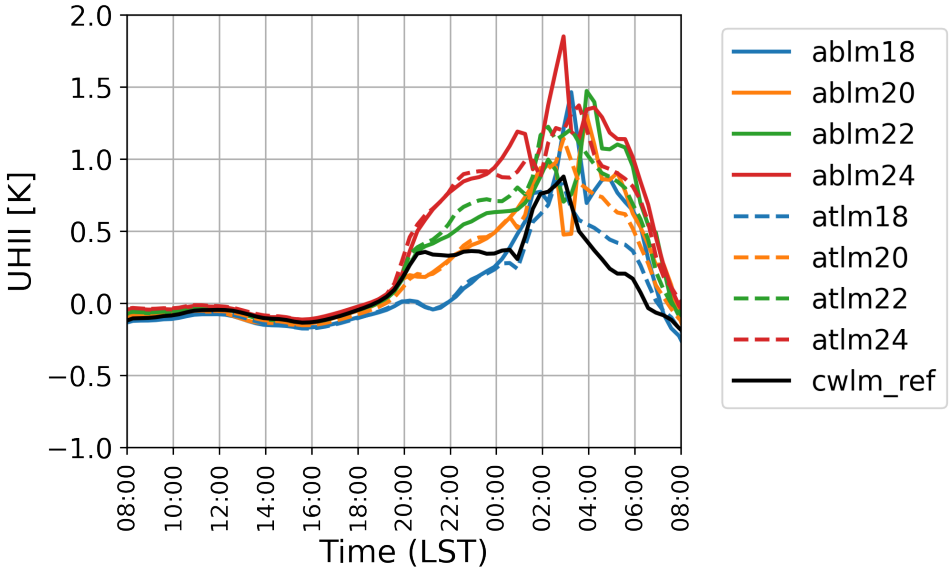

Figure 4.13.: Time series of the urban heat island intensity of the temperature nudging (at-), both wind and temperature nudging (ab-) group cases and the reference case ($cwlm\_ref$)

Table 4.5.: Summary of the maximum urban heat island intensity ($UHII_{max}$) and its occurrence time for each case in the *c* wind nudging group, the *at* temperature nudging group, and the *ab* group with both wind and temperature nudging

Case ID	**UHII$_{max}$ [K]**	**Time (LST)**	**Case ID**	**UHII$_{max}$ [K]**	**Time (LST)**
cwvl	0.50	Day2 00:35:00	cwvl_ref	0.45	Day2 00:15:00
cwlm	1.24	Day2 02:55:00	cwlm_ref	0.88	Day2 02:55:00
cwmh	0.46	Day2 01:15:00	cwmh_ref	0.46	Day2 05:15:00
cwvh	1.18	Day1 21:55:00	cwvh_ref	1.21	Day1 22:15:00
ablm18	1.46	Day2 03:15:00	atlm18	0.84	Day2 02:35:00
ablm20	1.30	Day2 03:55:00	atlm20	1.14	Day2 02:55:00
ablm22	1.47	Day2 03:55:00	atlm22	1.22	Day2 02:15:00
ablm24	1.85	Day2 02:55:00	atlm24	1.37	Day2 03:35:00

4.4. Conclusions

In this study, we investigated how the nudging approach can improve the representation of urban effects on the wind and temperature fields of Hamburg at a 500 m grid spacing. The results show that nudging is a useful tool to model wind reduction effects and urban heat island development, which are both important components in understanding the urban environment. Additionally, nudging is an approach that is relatively easy to implement and can be applied to a variety of urban scenarios, demonstrating the potential of applying the nudging approach to better represent urban effects in global-scale weather and climate models.

A few key take-away points are summarized here regarding using the nudging approach:

1. Wind nudging experiments show that nudging can well represent the wind speed reduction within and above urban canopies. The greatest wind reduction was simulated in the city center of Hamburg, where the tall and dense buildings are located. The implicit urban parameterization used in METRAS can also result in a wind speed reduction in urban areas that depends on the ambient wind speed. In contrast, the nudging effect, which acts as an additional effect to the implicit parameterization, is hardly dependent on the ambient wind speed.

   It is important to note that the surface wind fields are strongly affected by the gravity waves. The waves are induced by surface influences, generated at the inversion layer,

and propagate the wave energy downwards. In addition, the formation of clouds and rain, initiated e.g. by gravity waves and updrafts and downdrafts, also contributes to the complexity of the model results.

2. Different from the traditional temperature nudging approach, which uses observation datasets as forcing data, this study uses indoor temperature. Temperature nudging experiments show that the UHI effect previously simulated by the implicit parameterization in METRAS was enhanced by the nudging approach, with the highest UHI was simulated in the city center. The temperature nudging effects are related with the difference between the model air temperature and the indoor temperature.

3. The results of this study demonstrate that lower wind speeds result in a higher UHI intensity, which is consistent with previous investigations (e.g. Schlünzen et al., 2010; Hoffmann et al., 2012)

However, there are some limitations of the study. First, only building surface fraction and building height are used as urban morphology input data for the nudging approach. This is based on the assumption that buildings within a grid cell extend to the top of each cell, i.e. a building height that is located between two model levels is attributed to the higher level. However, building height heterogeneity at the subgrid scale plays an important role in the development of vortexes, turbulence, and the urban surface temperature (Abd Razak et al., 2013; Yang and Li, 2015), and should therefore be considered in the parameterization, which might increase the complexity of the parameterization itself.

The meteorological situations used in this study are idealized, thus model results can not be accurately evaluated against observed datasets. The dense observation data for the city of Hamburg by Kirsch et al. (2022) can be used in future work.

As mentioned by Koopmans et al. (2023), the heat storage change in the canopy was not realized with the nudging approach. Another limitation of the temperature nudging approach is that heat transfer processes between the indoor and outdoor via walls or windows are only roughly considered. However, to consider these physical processes in detail is resources consuming and might be a second step in global scale modelling, with the first step to consider wind speed reduction also in the vertical using the simple nudging approach.

This study shows that the proposed parameterization based on the nudging concept can help climate researchers to better consider the impact of urban canopies on the atmo-

sphere in models, especially with limited computational resources. The extended nudging approach presents the advantage that renders it well-suited for integration into global-scale weather and climate models, specifically when investigating the impact of urban canopies on a larger scale.

5. Conclusions

5.1. Summary

Rather than including various parameterizations representing different types of canopies and effects, which is computationally time consuming and increases the difficulty of implementation, it would be more efficient to use a generalized canopy parameterization (GeCap) to represent the most important canopy effects in atmospheric models. The main objective of this thesis is to develop such a canopy parameterization. The GeCap should be simple enough to be fluently implemented in the models with various scales, yet complex enough to represent the impacts of forest canopies (FCs), urban canopies (UCs) and forested urban canopies (FUCs) on the atmosphere. Working on this goal started with conceptualization and then transitioned to numerical developed from Chapter 2 to Chapter 4. The three research questions stated in Section 1.2 are answered in this section, based on the findings contained in this thesis.

Q1: Is it possible to develop a generalized canopy parameterization (GeCap) applicable to forest, urban, and forested urban canopies?

The theoretical precondition for developing GeCap is that FCs, UCs, and FUCs have impacts on the atmosphere that result from similar changes in the physical processes, even though the three types of canopies differ greatly in terms of morphology, structure and functions. Thus, the influences of FCs, UCs, and FUCs on the atmosphere were comprehensively analyzed from four main aspects: aerodynamics, thermodynamics, hydrology, and air quality (Section 2.2). It was found that there are strong similarities between the FCs, UCs and FUCs in terms of their effects on wind and turbulence (aerodynamics), and on the energy balance (thermodynamics); the main differences lie in their impacts on the water balance (hydrology) and air quality. Due to the presence of obstacles such as buildings and trees, all types of canopies share the following identical effects: wind speed reduction throughout the canopy layer; reduced turbulence intensity within canopies but enhanced at the top of canopies; enhanced absorption and reflection of shortwave radiation; shadowing effects; enhanced absorption and emission of longwave radiation; as well

as precipitation interception. Thus, the answer to the this research question is yes, it should be possible to develop a generalized canopy parameterization.

However, FCs and UCs have some opposite behavior related to obstacle surface materials (impervious or pervious), such as surface runoff (decreased in FCs but increased in UCs), infiltration and soil water storage (increased in FCs and decreased in UCs). Moreover, some processes are only specific for UCs, such as anthropogenic heat release, AVOC and GHGs emissions; on the other hand, BVOC emissions and photosynthesis only exist in FCs.

For designing a GeCap, two external systems, namely, the atmosphere and soil system should be considered with a particular focus on their interactions with the canopy layer (Section 2.4). Four internal factors should be included in GeCap: canopy characteristics, processes, fluxes, and effects. Practically, canopy characteristics (e.g. canopy structures, surface materials, geometry, and function) should be introduced as input data to GeCap, the physical processes are then calculated in GeCap by modifying the fluxes (e.g. momentum flux, radiative flux, heat flux, etc.) in the governing equations (e.g. conservation of momentum equation, surface energy budget equation, water budget equation, etc.), and GeCap should aim to represent the important canopy effects mentioned above.

Q2: Can we achieve the wind profiles found within urban areas by using a simple parameterization?

A good estimate of vertical profiles of mean wind speeds and turbulence within urban canopies is important for urban planning, urban wind energy, and urban air quality studies. To capture these aerodynamic characteristics of urban canopies, the present thesis has developed a parameterization based on the nudging concept (Section 3.2). A nudging term was added as a sink term in the momentum equation to represent the lost momentum imposed by urban obstacles (buildings), and the resulting amount of lost energy is tracked and then added as a source term in the TKE equation in order to conserve energy. Additionally, 3D urban morphology information (building height and building surface fraction) was incorporated into the parameterization through the weighting function in the nudging term.

The GeCap parameterization was applied in the mesoscale model METRAS with a spatial resolution of 500 m and tested with idealized urban morphology (Section 3.3). The simulation results are assessed by comparing to the data taken from a microscale model that resolves obstacles. Comparison results showed that the extended nudging approach performed well in parameterizing the aerodynamic canopy effects, in terms of the quasi

exponential shape of the spatially-averaged mean velocity profile and enhanced turbulence intensity at the top of canopy, which were also obtained in the obstacle resolving model (Section 3.4). Therefore, the answer to this research question is yes, this parameterization based on the extended nudging approach is simple enough to be implemented in the atmospheric models yet effective enough to represent aerodynamic 1st order building effects within urban areas.

Q3: What are the influences of a simple parameterization on the urban heat island?

Like many mesoscale and global scale climate models, METRAS uses a slab land surface scheme to represent urban effects, but does not account for the energy exchange between the urban canopy with its 3D morphology and the atmosphere. GeCap has addressed this issue by introducing a nudging term into the conservation equation of momentum and the prognostic equation for potential temperature. For this, indoor temperature values are prescribed as the forcing data (Section 4.2.1). The simulation was performed for the city of Hamburg using realistic urban morphology data as input (Section 4.2.2). The model results show that GeCap can enhance the UHI effects simulated by the slab land surface scheme, with the highest UHI intensities occurring in the centre of Hamburg, where dense areas and tall buildings are located (Section 4.3). The simulated UHI intensity depends on the temperature difference between the indoor temperature and the ambient air temperature; if the indoor temperature is higher than the air temperature, a higher UHI intensity is obtained, suggesting that more anthropogenic heat is released from the buildings to the atmosphere. In addition, when both wind and temperature nudging approaches were performed in GeCap, a negative relationship between wind speed and UHI intensity can be seen, indicating that lower wind speeds at the surface affect the vertical exchange processes up to the roof height, thus keeping more heat close to the surface and increasing the intensity of the UHI.

This thesis presents a generalized canopy parameterization based on an extended nudging approach. This new parameterization, GeCap, is capable of representing the most important atmospheric features of urban canopies, including their aerodynamic and thermodynamic effects. It is suggested that this parameterization be implemented in global-scale climate models and applied to other types of canopy effects in the future, paving the way for including canopy effects in global models and to get a better understanding of the role of canopies in the climate system.

5.2. Implications and outlook

This section provides some possible directions for further work.

1. In this thesis, GeCap is performed with a model resolution of 500 m. When implementing the GeCap for a global-scale climate model with a typical resolution of ~1 km, the influence of the model resolution on the results must be considered. For example, for the same city Hamburg, the building surface fraction and averaged building height per grid cell vary with the model resolution. A lower resolution results in lower values of building surface fraction and building height. This results in different values of the weighting function in the nudging term, potentially leading to an underestimation of the obstacle induced turbulence intensity, as discussed in detail in the Appendix E.
2. As mentioned in Chapter 1, urban canopies are transitioning to forested urban canopies with an increased presence of urban forests and vegetation in cities. When applying GeCap for these forested urban canopies, the opposing atmospheric impacts of buildings and trees should be taken into account. For instance, the effects of trees in mitigating heat stress and urban heat island and the modification of urban energy consumption (space conditioning and lighting) should be considered, especially for simulating extreme heat wave weather conditions. Additionally, 3D morphological structures of trees may not be necessary as they are too fine for the global models, but the height dependent fraction of vegetation per grid cell is required as input data.
3. Different from other nudging studies that use observed air temperature as forcing data (e.g. Koopmans et al., 2023), this thesis uses indoor temperatures with fixed values, without considering spatial heterogeneity. However, when implementing this parameterization in large-scale climate models, the heterogeneity of indoor temperature due to environmental factors such as local climate and altitude, and socio-demographic factors such as building standards and cultural expectations should be taken into account. Furthermore, depending on the application of the parameterization, other variables can also be used for nudging, such as air pollutant and greenhouse gas concentrations.
4. The present thesis uses Level of Detail 1 (LoD1) 3D building model data with a very high spatial resolution of 1 m to derive building surface fraction and averaged building height values for each grid, which are used to determine the weighting function in the nudging term. Results show that the building effects on the mean wind

speeds are represented by GeCap; however, the turbulent kinetic energy production is underestimated (Section 3.4). This can be related to a lack of detailed representation of urban morphology and can potentially be addressed by incorporating more building parameters, such as aspect ratio, sky view factor, and building frontal fraction. On the other hand, while LoD1 data is available for many cities and states (Dukai et al., 2019; Anon, 2022), a global LoD1 mapping is not yet available, making it difficult to use as input in global scale models.

In this context, Local Climate Zone (LCZ) mapping data could be used instead. LCZ is a classification system consisting of ten urban classes and seven natural classes, each characterized by specific text descriptions, morphological parameters (e.g. sky view factor, aspect ratio, building surface fraction), and physical parameters (surface admittance, surface albedo, anthropogenic heat output) (Stewart and Oke, 2012). A global LCZ dataset with a resolution of 100 m has been developed by Demuzere et al. (2022). However, when converting LCZ to input data for the parameterization, some technical challenges may arise, as discussed in detail in Appendix F. For example, in models that already have land use and land cover classifications, combining existing land cover classifications with the LCZ classifications could be double work. Additionally, each LCZ class is defined by a specific range of values for the physical and morphological parameters, but it is unclear which value in the range to use. More efforts should be devoted to determine appropriate values for each LCZ class adapted to the urban environment of specific cities. Moreover, the physical parameters included in LCZ need to be supplemented with other important land-cover-dependent physical parameters (e.g. thermal diffusivity, thermal conductivity, soil water availability) to adequately parameterize the thermodynamic processes.

Given the finite computational resources, a trade-off between efficiency and level of model complexity is often encountered when developing a parameterization. This study focuses on the efficiency of the parameterization, thus only the most important canopy effects are represented. With continued improvement in both computer power, model resolution, as well as new mapping data, GeCap should be able to represent more processes in the future.

Acknowledgements

I am very fortunate to have had so many kind people providing me with unwavering support and encouragement on this PhD journey. I am grateful to each and every one of them for being such an integral part of this wonderful experience.

First and foremost, I would like to express my sincere gratitude to my supervisor, Prof. Dr. Heinke Schlünzen. Thank you, Heinke, for your excellent guidance and support throughout my doctoral thesis. Doing the PhD was like hiking through a vast, unknown forest in the dark, and your advice and encouragement were the North Star always guiding me; without it, I wouldn't have been able to make the journey.

I would like to thank my second supervisor Prof. Dr. Bernd Leitl and my panel chair, Dr. Frank Lunkeit. Thank you, Bernd and Frank for your helpful suggestions and support.

I would like further to thank Prof. Dr. Peter Rayner from the University of Melbourne and Dr. Marcus Thatcher from the Commonwealth Scientific and Industrial Research Organisation (CSIRO). Thank you, Peter and Marcus, it was a great pity that the plan for a joint PhD program was unable to come to fruition due to the pandemic, but I am still grateful for the consistent remote support you provided. Our regular online meetings were very beneficial, providing me with invaluable ideas and insights.

I would like to thank all the members of the MeMi working group for creating such a great working environment. Thank you, David, for your constant supply of insightful suggestions and for helping me to solve various modelling problems. Thank you, Vivien, I have always enjoyed working with you in office room 1607. Our time together, accompanied by enjoyable tea and lunch breaks, has made the working experience even more delightful. Thank you, Karo and Franzi, for the interesting discussions on our research topics, which inspired me a lot. Thank you, Marita, for your constant support, especially in handling the LoD1 data. Thank you, Ronny, Louisa and Christian, for your helpful support and advice.

I also want to thank Sylvio from the wind tunnel group for his work in collecting wind tunnel data to be used as validation datasets for my study and for providing insightful

advice.

I acknowledge the financial support through the Deutsche Forschungsgemeinschaft (DFG, German Research Foundation) under Germany's Excellence Strategy-EXC 2037 "CLICCS-Climate, Climatic Change, and Society"-Project Number: 390683824, contributing to the Center for Earth System Research and Sustainability (CEN) of Universität Hamburg.

I would like to thank my friends. Thank you, Yiqian, not only for being the best flatmate in the world, but also for bearing with me during all those happy, exciting, and anxious times. Thank you, Qiyun, Yumeng, Guannan, Zhongqi, and Wenlin, for our interesting discussions in the "Meteorology Discussion" WhatsApp group, both on topics related to meteorology and beyond it. Thank you, Christina, Helia, and Kai, for your constant support and encouragement. A special thanks goes to Yumeng; whenever I had questions about coding or mathematics, you have always been there to help - no matter day or night.

I would like to deeply thank my family for always being a constant and strong source of support and comfort for me. Thank you, grandparents, for your constant compliments.爷爷和奶奶, 谢谢你们一直以来的夸奖。 Thank you, auntie Yuan, uncle Qing and my cousin Timo, for always giving me supportive advice and helping me out whenever I needed it. A special thank you goes to Timo, thank you for patiently helping me improve my German, especially polishing my yearly Weihnachtsgedichte.

I would also like to thank my beloved grandpa, who passed away before I completed this thesis. Thank you, grandpa, for your unwavering belief in me and constant encouragement throughout my educational journey. 外公，谢谢你在我求学路上不断地鼓励我，永远怀念你。

Last but not least, I am eternally grateful to my parents for their unconditional support, constant encouragement and endless love. 爸爸妈妈，谢谢你们源源不断的鼓励和支持,以及无穷无尽的爱。

A. Code workflow for using the extended nudging approach in METRAS

Figure A.1 shows a code flowchart of the use of the extended nudging approach as a canopy parameterization in METRAS. The nudging coefficient and weighting function, as well as the forcing data are given as input data. When wind (temperature) nudging is implemented, wind speed (air temperature) at the urban grid cells covered by buildings ($bsf > 0$) is nudged. Wind nudging induces the lost kinetic energy between two time steps and this amount of energy is tracked and then added as a source term to the turbulent kinetic energy at each time step.

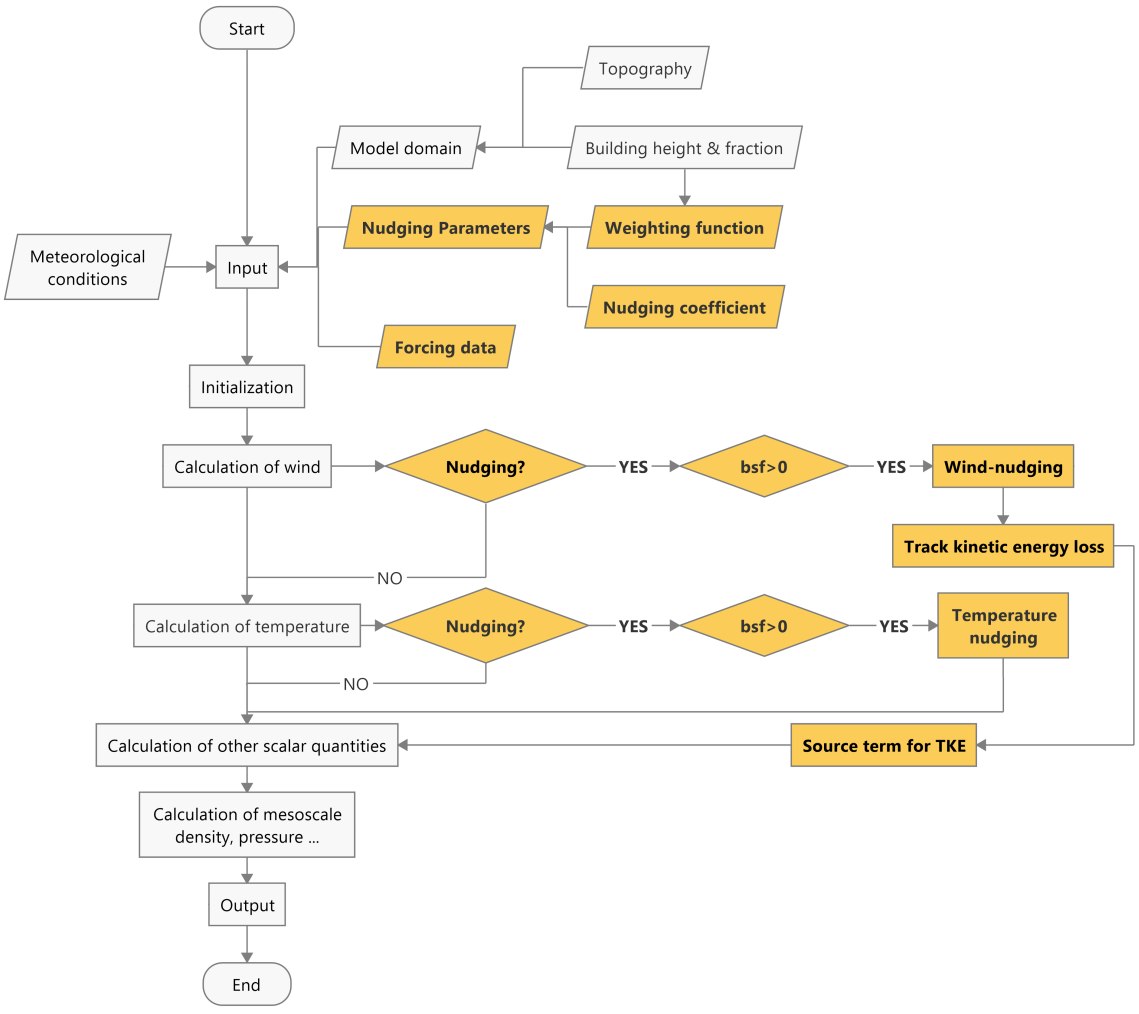

Figure A.1.: A code workflow for using the extended nudging approach as a canopy parameterization in METRAS. Yellow boxes indicate the steps related to nudging

B. Results of updrafts and downdrafts obtained from METRAS and MITRAS simulations

Figure B.1 and B.2 show the vertical profiles of horizontally averaged downdraft and updraft vertical velocities obtained from METRAS and MITRAS simulations.

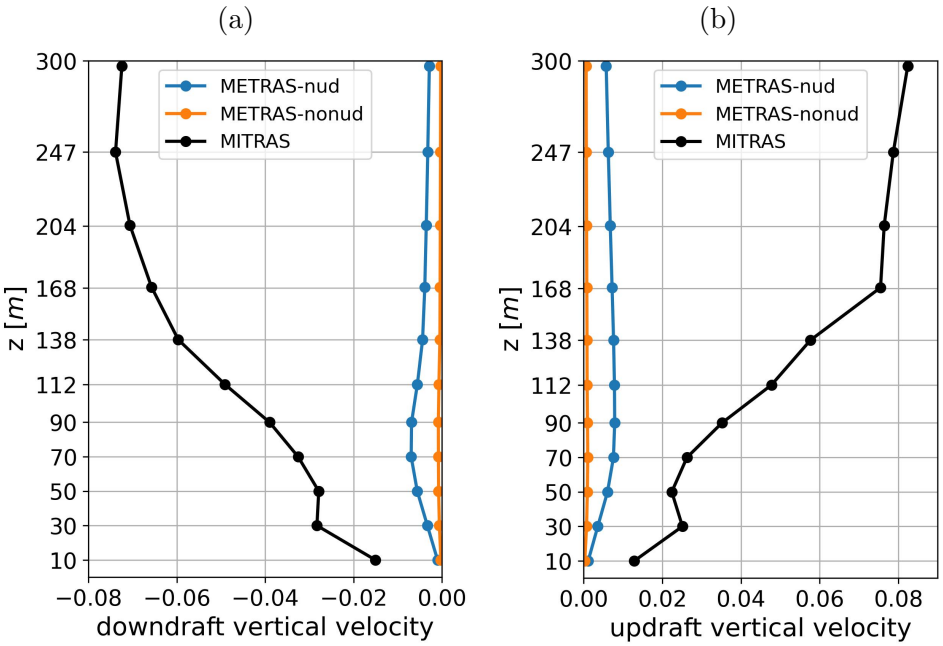

Figure B.1.: Vertical profiles of horizontally averaged (a) downdraft and (b) updraft vertical velocities. The blue line represents the METRAS simulation with nudging (METRAS-nud), the yellow line the METRAS simulation without nudging (METRAS-nonud), and the black line the MITRAS simulation. Velocities are normalized by the undisturbed horizontal wind speeds.

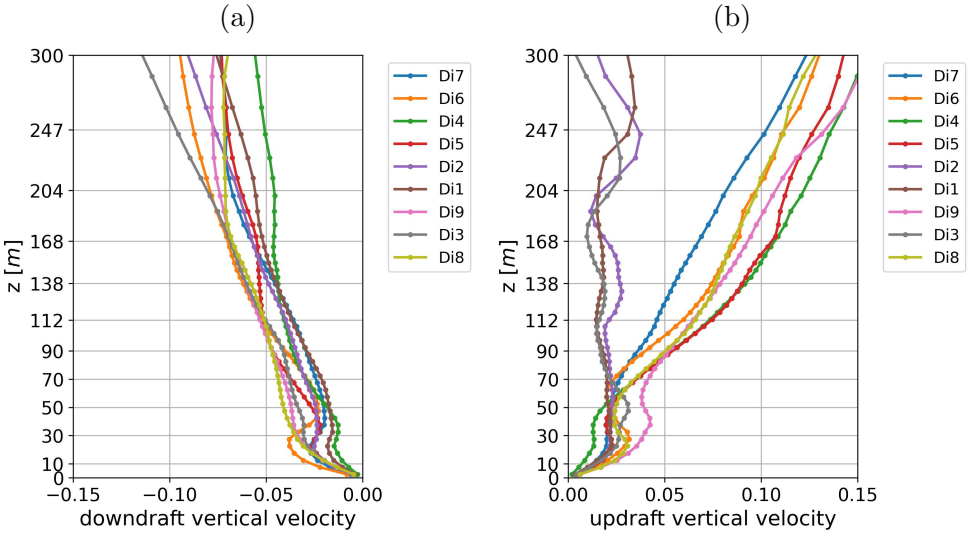

Figure B.2.: Vertical profiles of horizontally averaged (a) downdraft and (b) updraft vertical velocities for each subdomain in the *Di*. Velocities are normalized by the undisturbed horizontal wind speeds. Labels are sorted according to the building surface fraction at 0 to 20 m of each subdomain in *Di*, from highest (*Di7*) to lowest (*Di8*)

C. Processing of Level of Detail 1 (LoD1) 3D building data

Figure C.1 shows a workflow for converting LoD1 data to grid data for use in parameterization.

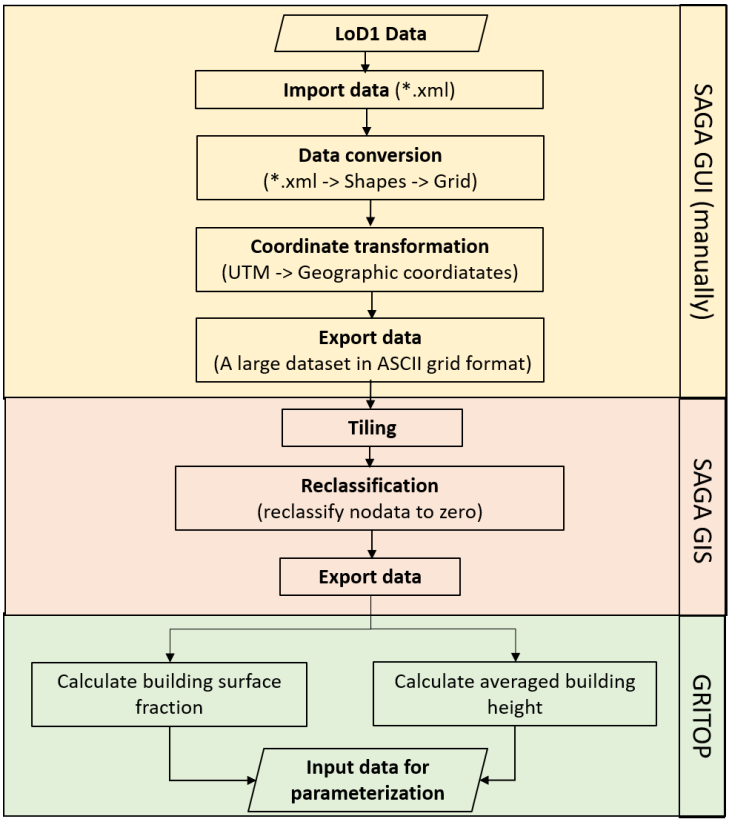

Figure C.1.: A workflow for processing LoD1 data by using SAGA (Conrad et al., 2015) and GRITOP (Schlünzen and Grawe, 2018)

Figure C.2 shows the spatial patterns of the building surface fraction at the second and third levels of the model domain. Compared to the first model level, the number of grid cells covered by buildings has decreased at the second level, and even fewer cells are covered by buildings at the third level.

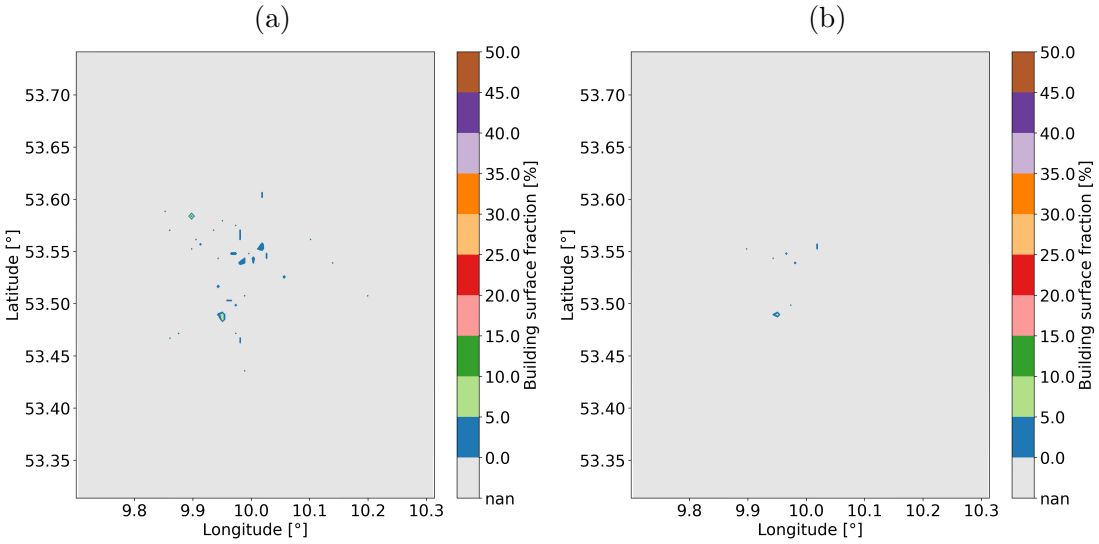

Figure C.2.: The spatial pattern of the building surface fraction at the (a) second model level and (b) third model level for the model domain with a resolution of 500 m

D. Time series of rain and cloud water

Figures D.1 to D.3 show the time series of the cloud water content and the rain water content for the different nudging groups.

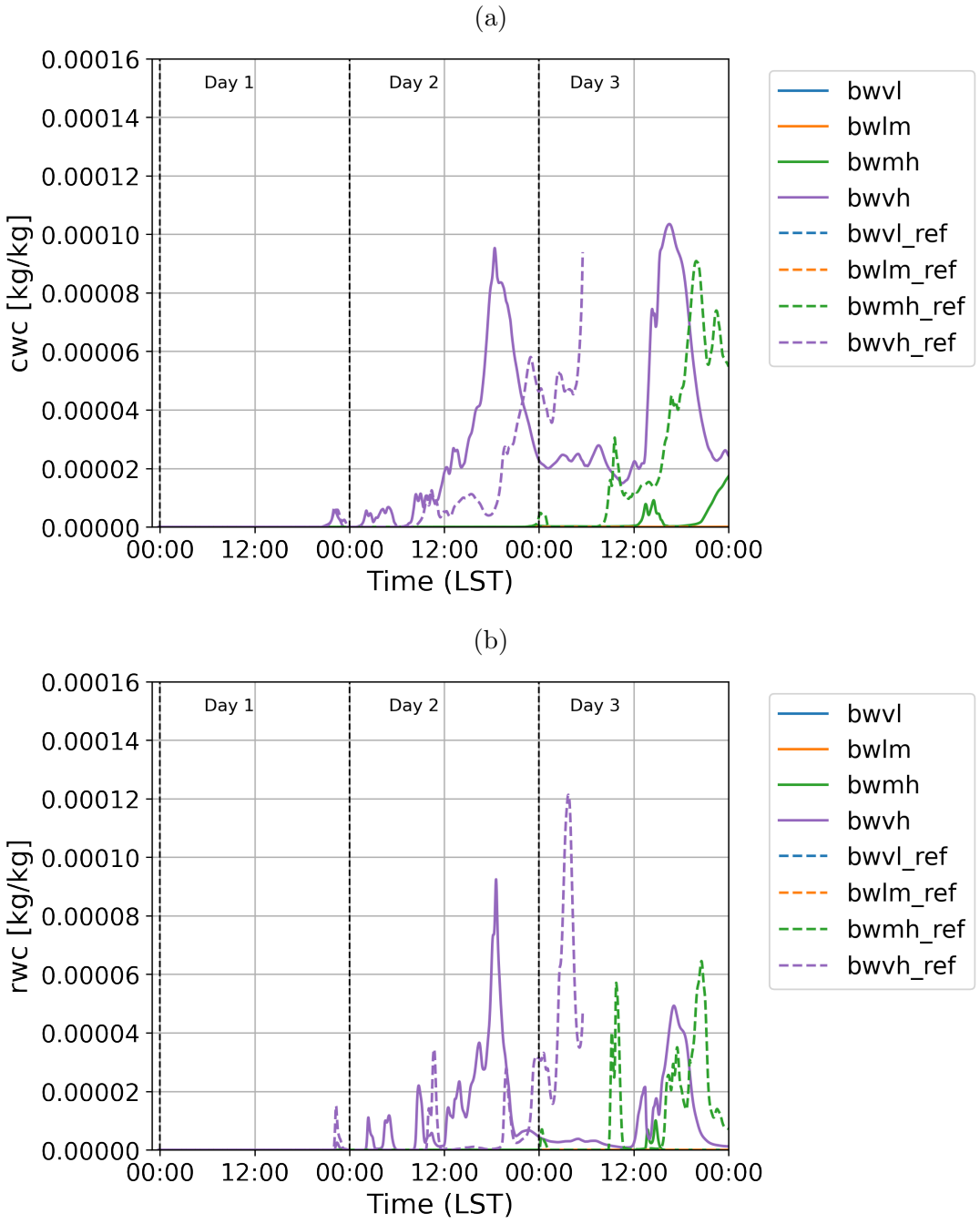

Figure D.1.: Time series of (a) cloud water content and (b) rain water content for the wind nudging *b*- group

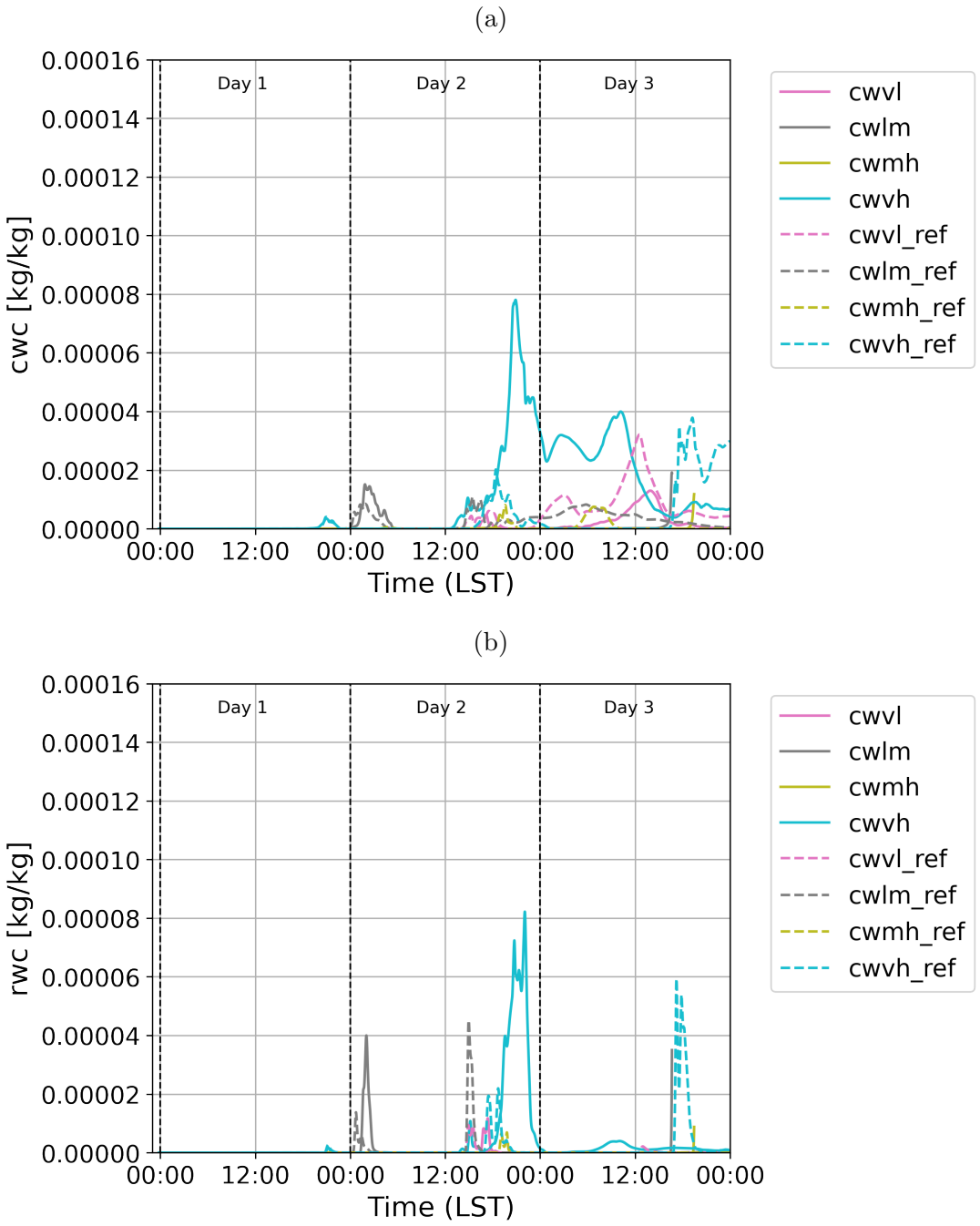

Figure D.2.: Time series of (a) cloud water content and (b) rain water content for the wind nudging *c*- group

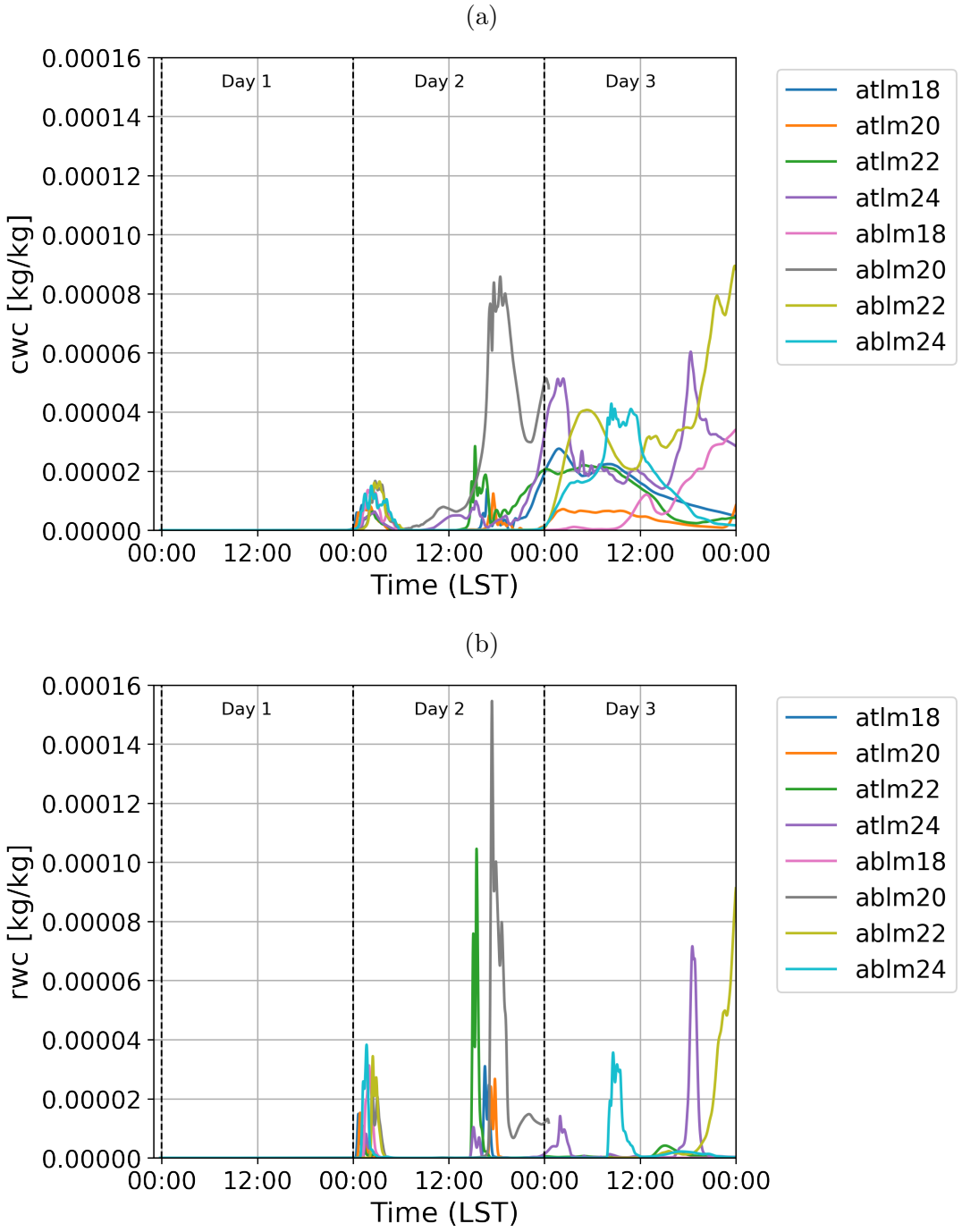

Figure D.3.: Time series of (a) cloud water content and (b) rain water content for the temperature nudging *at-* group and for the temperature and wind nudging *ab-* group

E. Verifying canopy parametrization effects with wind tunnel data

In this chapter, the canopy parameterization effects are evaluated using the wind tunnel data as a validation dataset. The relationship between the model resolution and the parameterization effect is also investigated.

E.1. Wind tunnel data

E.1.1. Experimental Set-up

The experiment was performed in the "Blasius" wind-tunnel facility of the Environmental Wind-tunnel Laboratory (EWTL) at the University of Hamburg. Blasius has no heating capabilities, thus neither diurnal cycle nor buoyancy effects are present. Coriolis force effects are neglected in Blasius and the modelled flows are neutrally stable. The test section is 1.5 m wide, 1 m high, and 7 m long. Four equidistant (in 6 cm width) isosceles-shaped spires (in 80 cm height) are placed at the start of the test section, followed by approximately 7 m of uniform roughness elements. The combination of spire arrays and roughness elements generates a scaled boundary layer flow with velocity and turbulence characteristics that are consistent with microscale urban canopy flows. With the roughness elements belonging to the "rough" class, the mean wind profile fits a logarithmic wind profile with a roughness length $z_0 = (0.5 \pm 0.11)$ and a power law with a profile exponent ($\alpha = 0.21 \pm 0.01$).

Flow data were measured using a Laser-Doppler Velocimeter (LDV) with a two-dimensional fiber-optic probe at sampling rates up to 6 Hz (at full-scale). A 3-minute time series was recorded at each measurement location corresponding to approximately 25 hours at full scale. With this measurement approach, small scale turbulence can be resolved in time.

E.1.2. Canopy geometries and measurement locations

A physical model with a scale of 1:500 has been designed by abstracting the model domain *Di* and incorporating building information, i.e., building height and building surface fraction. The model has a height of 60 m and consists of three vertical layers (Figure E.1). Each layer of the model has a shape of square cuboids with a height of 20 m at full scale, corresponding to the first three levels of *Di* (Figure 3.1). Since most buildings in *Di* are less than 60 metres high and the value of *bsf* at level four is less than 1 %, the physical model of the canopy consists of only three layers. The horizontal cross-sectional areas of the square cuboids are calculated using the *bsf* values for the *Di*.

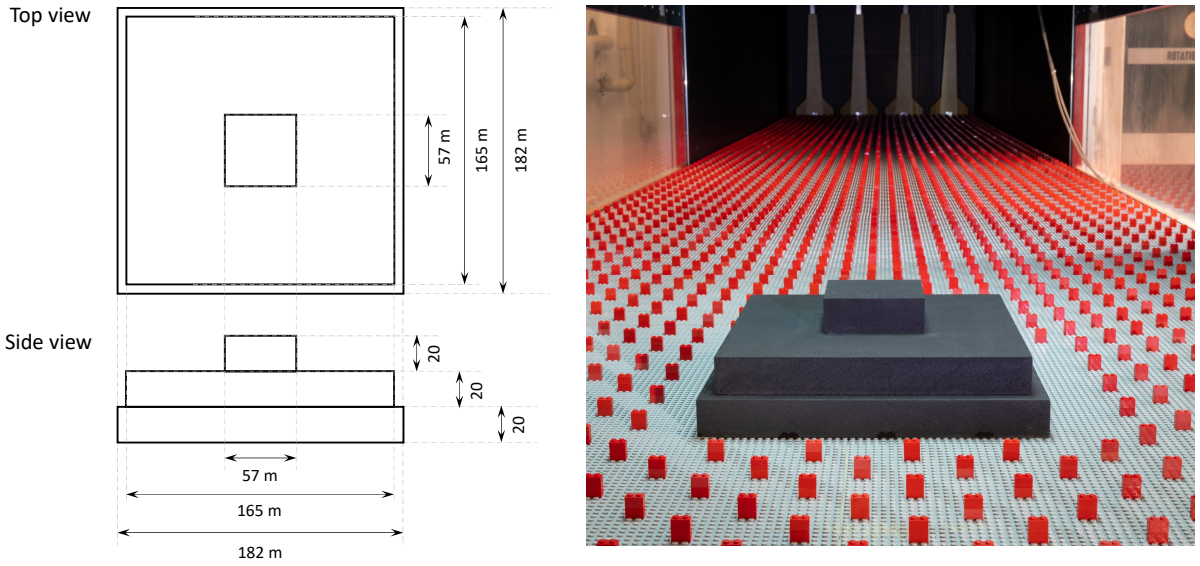

Figure E.1.: The shape and geometry information of the physical model in the wind tunnel. Figure provided by ©Freitas2021

For the analysis positions, ten measurement points (*P01* to *P10*) are defined horizontally, while in the vertical direction seven heights are measured ranging from 10 to 138 m (full scale) , and the seven heights correspond to the first seven vertical levels in *Di* (Figure E.2). For the point *P02* only four heights (70, 90, 112, and 138 m) are measured

as the levels from 0 to 50 m have been covered by the model itself. In total there are 64 analysis positions to compare with the mesoscale model results.

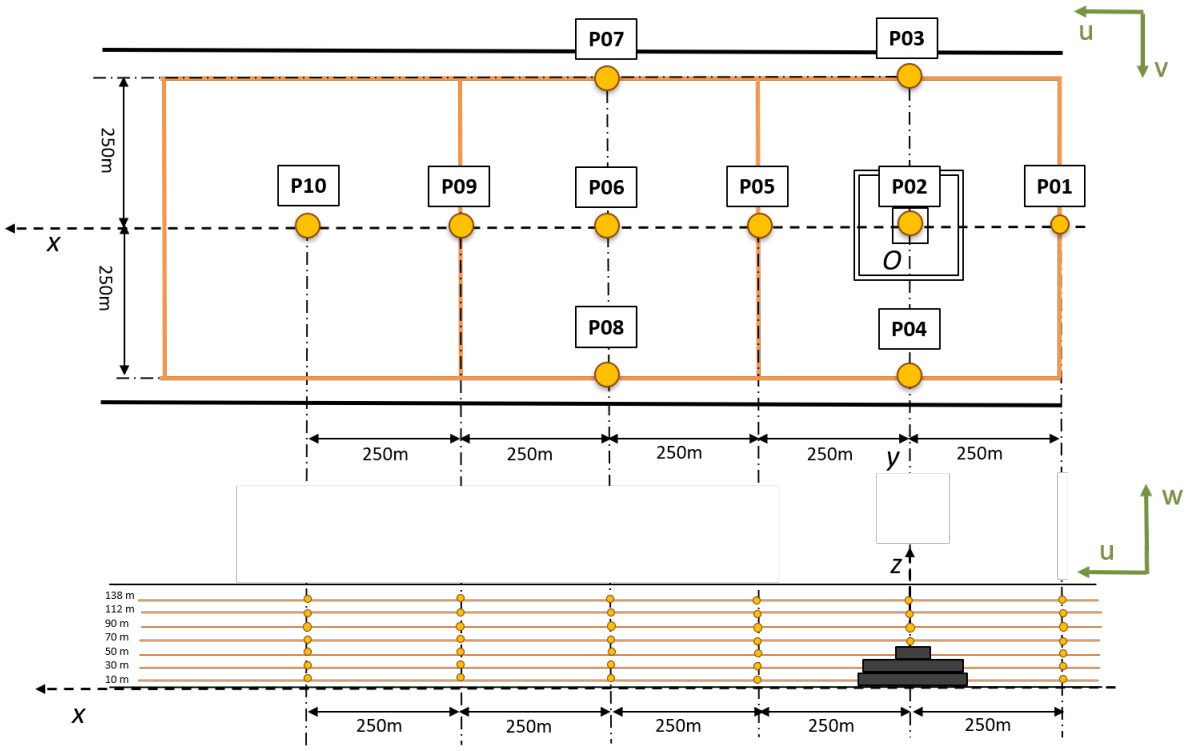

Figure E.2.: Geometries and measurement positions for the physical model of the canopy. All dimensions are in full scale. x, y, z are longitudinal, lateral and vertical coordinate axis, respectively. O is the orignial of coordinate system (0,0). u, v are the longitudinal (main) and lateral flow directions. The yellow points are the measurement points. The yellow boxes in the upper figure represent the mesoscale model grid cells, which have a resolution of 500 m. The yellow lines in the lower figure denote the vertical intervals in METRAS. The pyramid shape black box is the physical model

E.2. Model set-up and meteorological conditions of METRAS and wind tunnel experiments

A wind tunnel is comparable in resolution to an obstacle-resolving microscale model, making data comparison between the two scales common (Grawe et al., 2013a; Gronemeier et al., 2021). However, due to the coarse resolution of the mesoscale model, direct comparison of mesoscale model results and wind tunnel data is challenging. Grawe et al. (2013a) suggested that the limitations encountered while measuring datasets in a wind

tunnel should be considered when setting up numerical model simulations. In this chapter, two principles were followed in designing the set-ups of the METRAS runs and the wind tunnel experiment: i) keep the set-up of both approaches as equivalent as possible, in terms of meteorological conditions, roughness lengths, simulation duration, etc.; ii) take into account the limitations of the microscale wind tunnel datasets and preserve as many characteristics of the physical processes as possible. For example, Coriolis force effects (vertical wind rotation) are negligible at the microscale, but are important for mesoscale processes, and therefore need to be taken into account in METRAS. The set-ups of METRAS and wind tunnel experiments are summarized in Table E.1.

Table E.1.: Model set-up and meteorological conditions of METRAS and wind tunnel experiments

Parameter	**Wind Tunnel**	**METRAS**
Roughness length height	0.5+/-0.11 m	0.6 m
Stratification	Neutral	Neutral
Diurnal cycle	No	No
Simulation duration	25 hours (full scale)	25 hours
Coriolis force	No	Yes
Background winds	4.2 m/s	4.2 m/s
	Easterly winds	Easterly winds (at 125 m high)

In general the virtual measurement points selected in the METRAS model domain should be at the exact location of the measurement points in the wind tunnel. There are two difficulties in identifying the corresponding virtual measurement points in METRAS. First, only three grid cells from domain *De500* (with a horizontal resolution of 500 m, *De500* is the same as *De* used in Chapter 3) can be selected for analysis, since all the measurement points are located within these three grid cells (the three yellow boxes in Figure E.2). As these three grid cells are located together, differences in the modelled flow characteristics between them might not be obvious. Secondly, the wind tunnel employs geographic coordinates, whereas METRAS implements the Arakawa C-grid, i.e., scalar values are calculated at the center of the grid and the wind velocity components u and v are staggered at the west/east and south/north edges of the cell, respectively. Thus, only *P01*, *P05*, *P09* can be used to analyze the u component, *P03*, *P04*, *P07*, *P08* for the v component, and *P02*, *P06* and *P10* for scalar values, such as wind speeds and turbulent fluxes.

To overcome these two problems, and better understand the impact of the model resolution on the canopy parameterization effect, three further METRAS runs were performed

with the model domains at higher resolutions: 250 m (*De250*), 125m (*De125*), and 62.5 m (*De62*). Note that with increasing the resolution of the model domain, the domain areas remain the same for all four cases, but the number of building-covered grid cells, building surface fractions, and virtual measurement positions vary (Table E.2). For example, *De500* has only one grid cell covered by buildings, while *De62* has sixteen, with four grid cells at level 1 being fully covered by buildings (bsf=1.0), eight grid cells being 45% covered, and four grids being 20% covered. A schematic representation of the grid cells and virtual measurement positions in METRAS for each case is given in Figure E.3.

Table E.2.: Model domain information. *bsf* refers to building surface fraction and k to the number of the vertical model level

Case name	***De500***	***De250***	***De125***	***De62***
Resolution	500 m	250 m	125 m	62.5 m
Number of all grid cells across domain	30 x 30	60 x 60	120 x 120	240 x 240
Domain area (km^2)	15 x 15	15 x 15	15 x 15	15 x 15
Number of urban grids	1x1	2x2	2x2	4x4
bsf (k=1)	0.13	0.13	0.53	1.00; 0.45; 0.20
bsf (k=2)	0.11	0.11	0.44	1.00; 0.32; 0.10
bsf (k=3)	0.11	0.01	0.05	0.20; 0.00; 0.00

E.3. Results

Figure E.4 shows the horizontal cross-sections of the wind speeds at 50 m high for simulations with different model resolutions. It can be seen that the wind speeds are strongly reduced by the buildings in all four cases, with similar sizes of the building wake coverage areas. However, the magnitude of the maximum wind speed reduction varies depending on the model resolution. The strongest reduction is observed in the case *De*62, due to the largest building surface fraction, which results in the strongest wind nudging effects.

For the vertical cross sections, the time-averaged aerodynamic properties are analyzed: wind components u and v, turbulence intensities (I^{u}=σ^{u}/u, where σ is the standard deviation of u), and vertical momentum fluxes ($u'w'$). To compare the METRAS model results with the wind tunnel data, all the parameters are normalized using the reference data. The comparisons for the four cases are presented in Figures E.5 and E.6. As mentioned in Section E.1, only three points (*P02*, *P06*, *P10*) can be used for the comparison analysis for the case *De*500. These three measurement points are covered by three mesoscale grid

cells which are located together, resulting in only slight differences in the modelled flow and turbulence characteristics between the three points.

For the wind speeds, the METRAS results are in good agreement with the wind tunnel data, especially for the case *De*62 (Figure E.5 and E.6). For both turbulence intensities and vertical momentum fluxes, the values of the METRAS simulations are lower than the wind tunnel values, indicating that the turbulence production is underestimated by the parameterization. This is in line with the comparison results discussed in Chapter 3. Moreover, with increasing model resolution, a better comparison result between the wind tunnel data and the METRAS results can be seen, especially for the values at the measurement point *P05*. *P05* is located in the downwind area and closest to the canopy, so its wind and turbulence characteristics are the most strongly influenced by buildings. It can be seen that in all cases, *P05* has lower wind speeds and higher turbulence intensity as well as vertical fluxes, compared to the other measurement points.

In summary, for the representation of the mean wind speed reduction in the building wake, there is a good comparison between METRAS and wind tunnel data, especially at high model resolutions. For coarser resolutions the comparability of the results decreases and the agreement is lower. Sub-grid scale urban canopy effects can be parameterized sufficiently well for their impact on the average flow, but detailed changes can only be simulated at a sufficiently high resolution. In terms of turbulence characteristics, the canopy parameterization implemented in the METRAS tends to underestimate turbulence production, which is in line with the METRAS-MITRAS comparison results discussed in Chapter 3, suggesting that more source of turbulence should be added to the turbulence kinetic energy in the parameterization.

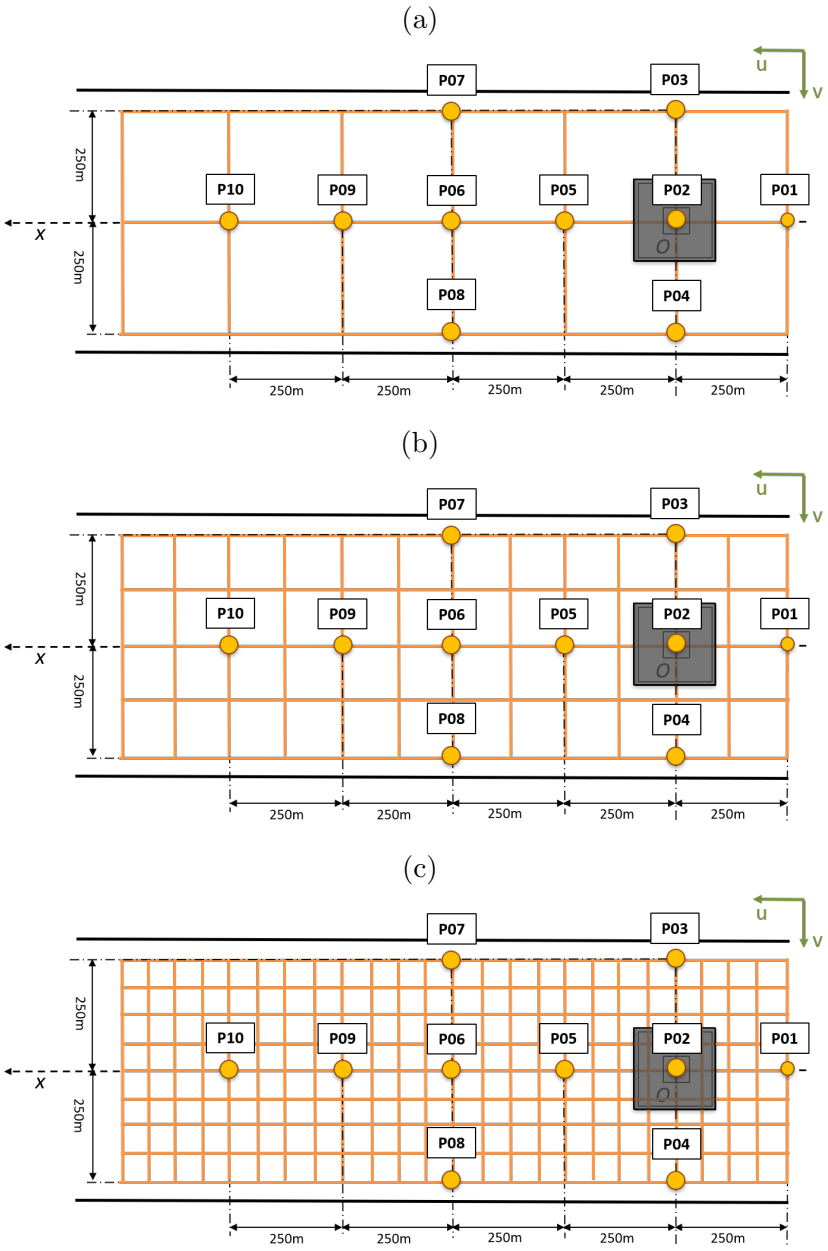

Figure E.3.: A schematic representation of the grid cells and virtual measurement points in the model domain for case (a) *De250* with a horizontal resolution of 250 m, (b) *De125* with a horizontal resolution of 125 m, and (c) *De62* with a horizontal resolution of 62 m. The yellow points are the measurement points. The yellow boxes in the upper figure represent the mesoscale model grid cells. The grey box refer to buildings. u, v are the longitudinal (main) and lateral flow direction

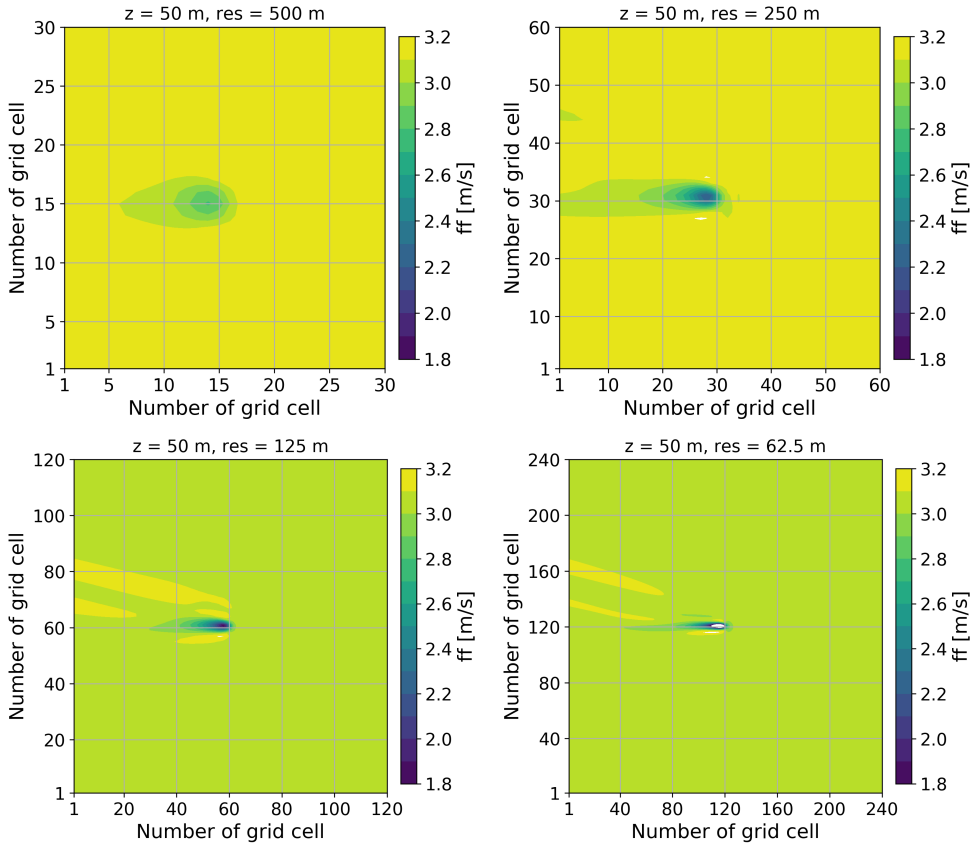

Figure E.4.: Horizontal cross sections of wind speeds ff at 50 m high for simulations with different model resolutions

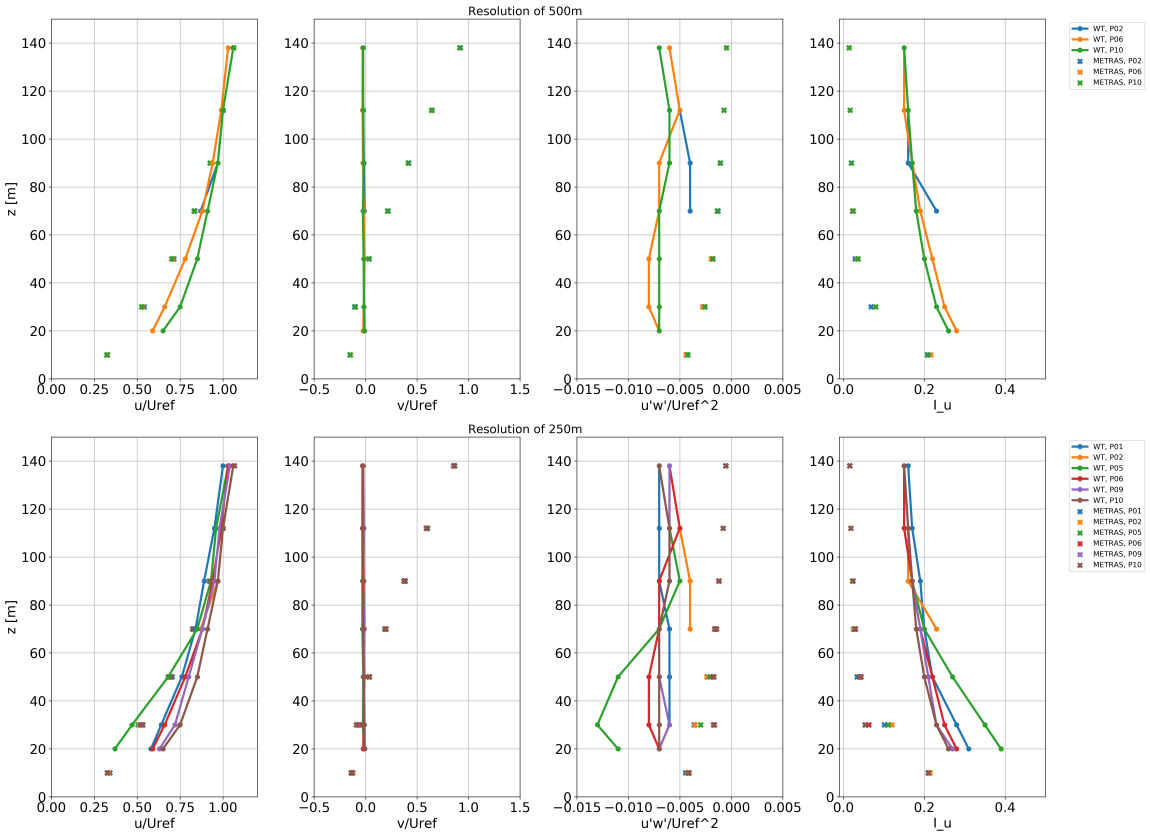

Figure E.5.: Vertical profiles of normalized mean u ($u/Uref$) and v ($v/Uref$) components, normalized mean vertical fluxes ($u'w'/Uref^2$), and normalized turbulence intensity (I_u) at all measurement points for cases $De500$ and $De250$. Line plots refer to METRAS results, and scatter points refer to wind tunnel data. WT for wind tunnel.

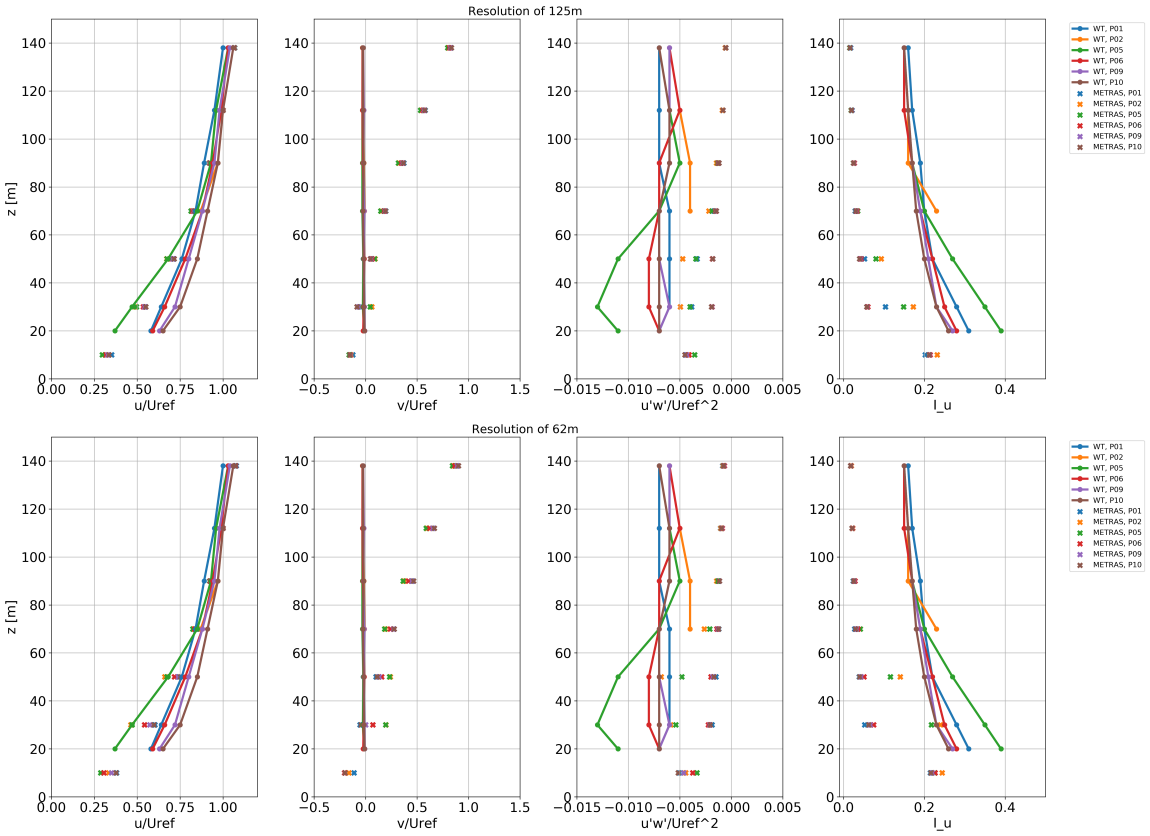

Figure E.6.: Same as Figure E.5, but for cases $De125$ and $De62$

F. Processing of Local Climate Zone data

F.1. An introduction to Local Climate Zone

Local Climate Zone (LCZ) developed by Stewart and Oke (2012) has been recognized as a generic, standardized classification of urban land cover types for urban studies. It consists of 17 standard classes, including 10 urban types (LCZ 1-10) and 7 natural land cover types (LCZ A-G). Each LCZ class is characterized by a range of values for different physical and morphological parameters, such as sky view factor, canyon aspect ratio, building surface fraction, and geometric average of building heights (Stewart and Oke, 2012).

LCZ data has been widely used as inputs for many urban canopy parametrizations (Alexander et al., 2015; Wouters et al., 2016) due to its four main advantages: 1) comprehensive coverage of urban canopy parameters; 2) being available online, mainly via the WUDAPT project; 3) ongoing research by research groups around the world to create, develop and evaluate the datasets; and 4) the generic nature of LCZ, which can capture the characteristics of most urban sites.

According to Stewart and Oke (2012), "The name is appropriate because the classes are *local* in scale, *climatic* in nature, and *zonal* in representation". To understand these terms, especially for those with an interdisciplinary background, it is necessary to provide some explanation. From a geographical perspective, *local* scale urban forms refer to blocks, courtyards, and neighbourhoods, with a typical horizontal extension of ~300-500 m and a vertical extent up to the top of the roughness sublayer. From a meteorological perspective, the atmospheric phenomena occurring at this scale belong to the microscale α phenomena (WMO, 2023). Moreover, LCZ classes do not directly describe climate zones, but rather land cover classes.

The World Urban Database and Access Portal Tools (WUDAPT) has made major contributions to the collection, storage, dissemination and application of Local Climate Zone data to improve global understanding of the form and function of cities (Bechtel

et al., 2015; Mills et al., 2015). Based on the spatial scale of the metadata, the WUDAPT data collection and products are divided into three levels of detail. Level 0 describes a city in terms of its landscape types using the LCZ scheme, with a resolution of 100-500 m; Level 1 provides more precise parameter values for each LCZ, but at the same resolution as Level 0; Level 2 includes the most comprehensive estimate of LCZ parameters at a resolution of 2 m (Mills et al., 2015; Ching et al., 2019; Bechtel et al., 2019). Level 0 maps have been developed for more than 120 cities and regions (Ching et al., 2019).

F.2. Processing of Local Climate Zone data for use as inputs to the model METRAS

This section describes the processing of LCZ data for use as inputs to the mesoscale model METRAS.

F.2.1. METRAS-50 classes and MEMI classes for the model METRAS

Firstly, two types of topography classes must be distinguished: METRAS-50 classes and MEMI classes. The METRAS-50 classes are used directly for the model METRAS, as each model grid cell is composed of one or more subgrid-scale METRAS-50 classes. METRAS-50 classes mainly describe material classes (e.g. sand, concrete, grass) and are characterised by different values for a set of physical parameters (e.g. albedo, thermal diffusivity, thermal conductivity, and roughness length). There are seven METRAS-50 classes relating to urban environments, namely asphalt, concrete, brick, steel, sealed urban, sparse sealed urban, and compact sealed urban (Schlünzen et al., 2012).

The topography metadata usually contains land cover than surface material information. MEMI classes, however, describe both land cover classes (e.g. airports, playgrounds, streets) and material classes (e.g. asphalt and concrete). Each MEMI class is composed of one or more METRAS-50 classes with different distributions. For example, the MEMI class "airport" consists of four METRAS-50 classes: asphalt (15%), short grass (65%), short bushes (10%), and sparse sealed urban (10%). To date, over seven hundred MEMI classes have been defined.

LCZ urban classes are defined by land cover types consisting of several material classes. For example, LCZ 1 (Compact high-rise) is defined as "Dense mix of tall buildings to tens

of stories. Few or no trees. Land cover mostly paved. Concrete, steel, stone, and glass construction materials". Therefore, all LCZ classes belong to MEMI classes.

F.2.2. Surface cover fraction for LCZ classes

A workflow for processing the LCZ data to be used as input for the model METRAS is presented in Figure F.1. The workflow consists of three main steps: (1) introducing LCZ classes into MEMI classes; (2) calculating the distribution of existing MEMI classes for each LCZ class; (3) calculating the fraction of METRAS-50 classes for each LCZ class.

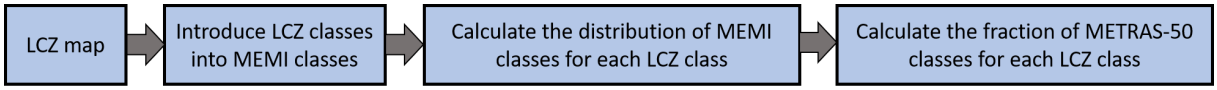

Figure F.1.: The workflow for processing LCZ to be used as inputs for METRAS

The LCZ raster dataset for the city of Hamburg (LCZmap_hh) was used. This map has a spatial resolution of 100 m and covers an area of 118.93 km^2. The LCZmap_hh includes seven LCZ classes: four urban classes (LCZ 2 Compact midrise, LCZ 5 Open midrise, LCZ 6 Open low-rise, and LCZ 8 Large low-rise) with a total fractional coverage of 14%, and three natural land cover classes (LCZ A Dense trees, LCZ D Low plants, and LCZ G Water) with a total coverage of 86% (Figure F.2). According to the definition by the WUDAPT, this dataset belongs to the Level 0 data. Only after the actual values for the parameters for each LCZ class have been determined is the dataset upgraded to Level 1.

In order to accurately assess the distribution of METRAS-50 classes for each LCZ class, a land cover dataset for the city of Hamburg (PK_LBM_hh) from the MEMI research group database was used. This dataset has a spatial resolution of 10 m and covers a much larger area than the LCZmap_hh. The data consists of 482 original MEMI classes and the corresponding METRAS-50 distributions for these classes are already known (listed in the table of MeMiClasses and corresponding METRAS50 distributions, not shown). In order to compare the two datasets and calculate the fraction of MEMI classes for each LCZ class, both datasets need to be converted into the same format, i.e. the features of both datasets should be the same including dimensions, coordinate reference system, coverage area, and resolution. The preprocessing of LCZmap_hh and PK_LBM_hh data is performed using the geographic information system computer program SAGA GIS (Conrad et al., 2015) and a workflow is given in Figure F.3. Figure F.4 shows the two datasets after the data preprocessing.

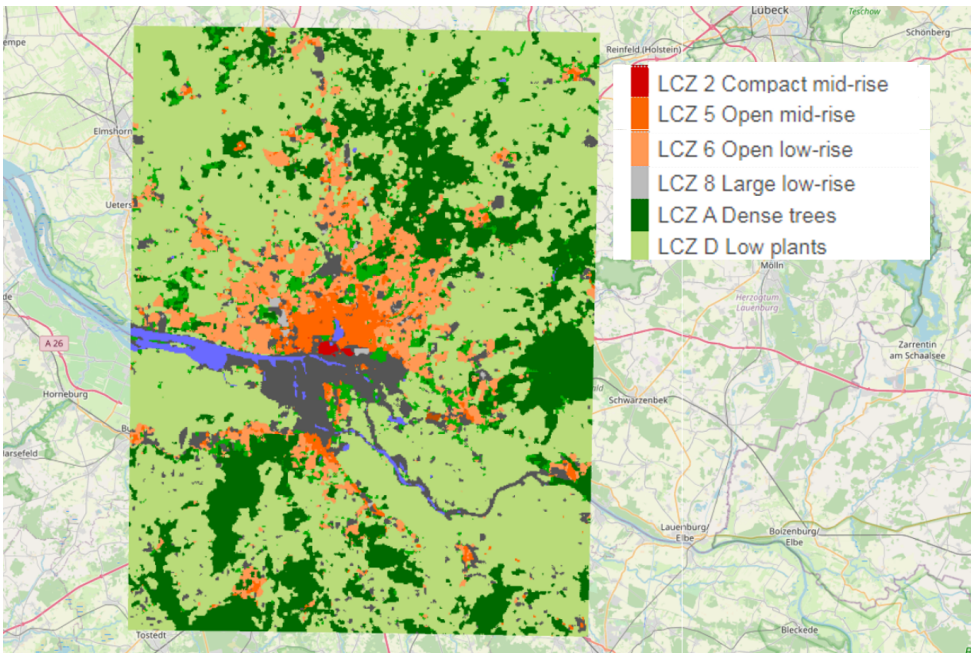

Figure F.2.: LCZ Map of Hamburg. Data from the WUDAPT website (WUDAPT, 2020)

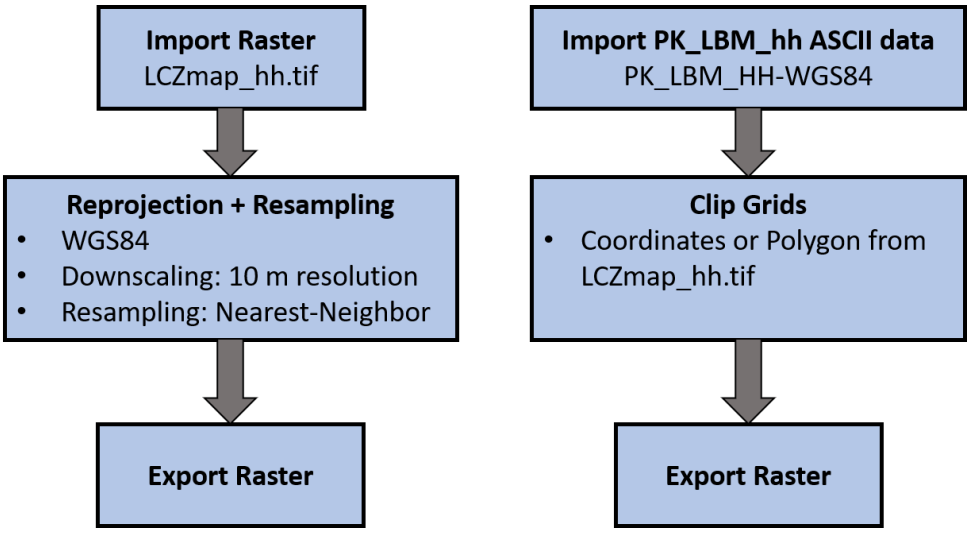

Figure F.3.: A workflow for converting PK_LBM_hh and LCZmap_HH data to the same format

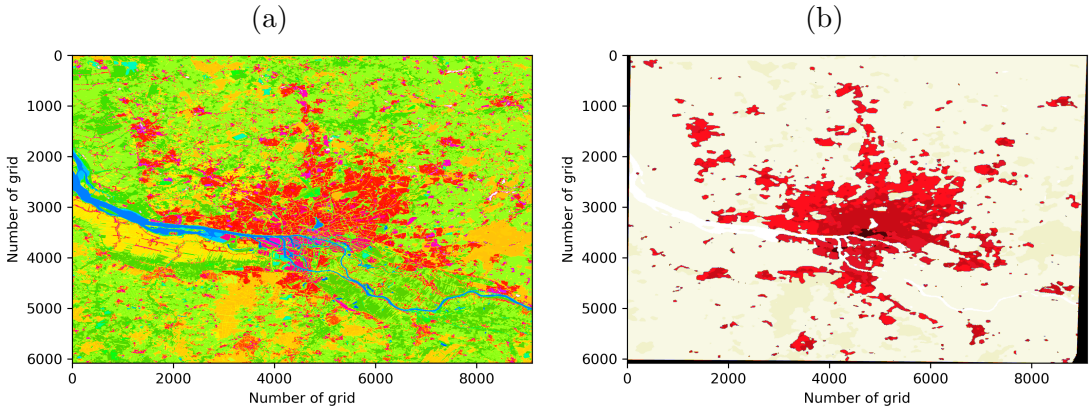

Figure F.4.: (a) PK_LBM_hh data and (b) LCZmap_hh data with the same spatial resolutions, coordinate systems and coverage areas after preprocessing

As the fractions of METRAS-50 classes for the original MEMI classes are known, and the distribution of original MEMI classes for each LCZ class has been calculated, the distribution of METRAS-50 classes for each LCZ class can be derived. Figure F.5 shows the distribution of MEME classes and METRAS-50 classes for the LCZ 2 (Compact midrise) class as an example. The LCZ 2 class consists of 74 MEMI classes, including port (12.3%, with MEMI number 6752), other buildings, innercity (12.1%, 7017), commercial space (12.1%, 6612), industrial area (6600, 10.0%), docks (9.5%, 1111), dense development for administration and services (8.6%, 6610), and other 68 MEMI classes (Figure F.5a). Then, the LCZ 2 class is further subdivided into 21 METRAS-50 classes. The main classes here are sparse sealed urban (29.4%, with METRAS-50 number 6005), compact sealed urban (24.0%, 6006), fresh water, stationary (18.4%, 1222), mixed forest (8.3%, 5300), and other 15 METRAS-50 classes (Figure F.5b). Due to the relatively coarse resolution of the LCZ_hh data (100 m, compared to the 10 m resolution of PK_LBM_hh), many ports and docks areas belong to the LCZ 2 class, which results in a high presence of water (18.4%) in this LCZ 2 for the city of Hamburg.

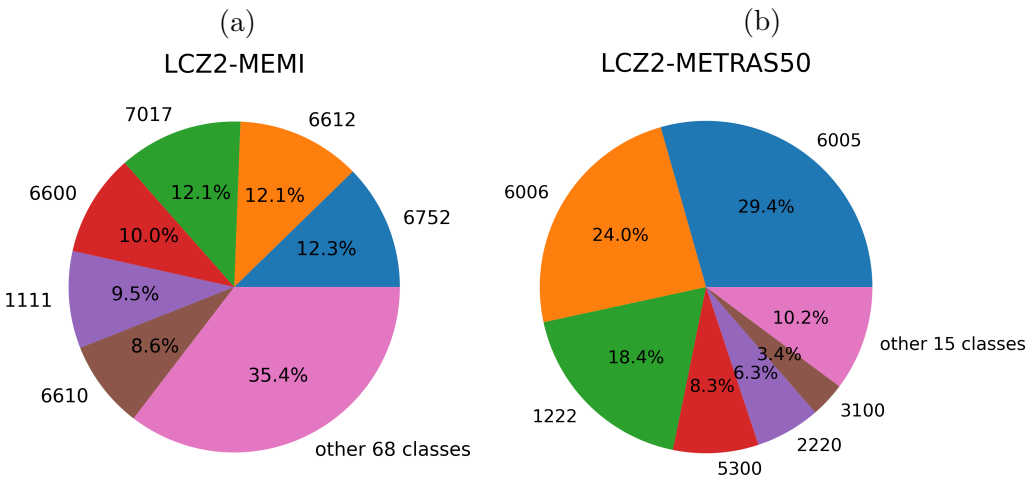

Figure F.5.: (a) Fraction of MEMI classes and (b) fraction of METRAS-50 classes for LCZ 2 class. The four-digit numbers refer to MEMI class or METRAS-50 class names.

F.3. Evaluation and summary

As mentioned in Section F.1, each LCZ class is defined by a range of values for the morphological parameters, including building surface fraction, impervious surface fraction, and pervious surface fraction. According to the definition of surface classes by Stewart and Oke (2012), the METRAS-50 classes can also be classified into these three categories: impervious, pervious and building surface. We use the range defined by Stewart and Oke (2012) to examine whether the shares of these three categories for the METRAS-50 classes in the LCZmap_hh align with the specified ranges. The three categories and their corresponding METRAS-50 classes are listed as follows:

- impervious surface classes: bare ground, rock, asphalt, concrete, brick/pavers, steel
- pervious surface classes: water, mudflats, gravel, sand, salt pit, bushes, grass, savanna, health, forest
- building surface classes: sealed urban, sparse sealed urban, compact sealed urban

The results of the fraction calculation are given in Table F.1. Note that the sum of the fraction values for three surface cover categories is 1. The results show that the fraction values of three categories for the natural classes (LCZ A, D, G) are within the defined range. However, the values for the impervious surface fraction and pervious surface fraction for all urban classes (LCZ 2, 5, 6, 8) are outside the defined range. The urban

LCZ classes have much lower impervious surface fraction and higher pervious surface fraction values than that defined by Stewart and Oke (2012). Possible reasons for the low impervious surface fraction might be that the three building surface METRAS-50 classes are not 100% covered by buildings; i.e., there are impervious surfaces included in this class. On the other hand, the high pervious surface fraction value might be related to the water areas specific to the city of Hamburg.

Table F.1.: Surface fraction evaluation for Hamburg. The ranges defined by Stewart and Oke (2012) for the morphological parameter of each LCZ class are listed in the parentheses. Values below the range are marked in blue, and values above the range are marked in red

LCZ	**Building surface fraction**	**Impervious surface fraction**	**Pervious surface fraction**
LCZ 2 Compact midrise	53.39 (40-70)	8 (30-50)	38.61 (<20)
LCZ 5 Open midrise	31.34 (20-40)	7.67 (30-50)	60.99 (20-40)
LCZ 6 Open low-rise	24.68 (20-40)	2.42 (20-50)	72.89 (30-60)
LCZ 8 Large low rise	48.41 (30-50)	8.15 (40-50)	43.44 (<20)
LCZ A Dense trees	0.88 (<10)	2.64 (<10)	97.35 (>90)
LCZ D Low plants	3.19 (<10)	4.80 (<10)	95.20 (>90)
LCZ G Water	2.66 (<10)	3.20 (<10)	96.80 (>90)

This chapter introduces the processing of LCZ data for use as input to a mesoscale model and shows some technical issues that arise. Firstly, the land cover definition in LCZ may not match the existing surface cover definition for the model, such as METRAS. Secondly, it is difficult to accurately determine the value for morphological parameters without other e.g. finer resolution building datasets being available. Additional effort should be made to adapt the values of the physical and morphological parameters for each LCZ class to the specifics of a particular city.

References

Abd Razak, A., Hagishima, A., Ikegaya, N. and Tanimoto, J. (2013) Analysis of airflow over building arrays for assessment of urban wind environment. *Building and Environment*, **59**, 56–65. URL: https://www.sciencedirect.com/science/article/pii/S0360132312002090.

Adane, Z. A., Nasta, P., Zlotnik, V. and Wedin, D. (2018) Impact of grassland conversion to forest on groundwater recharge in the Nebraska Sand Hills. *Journal of Hydrology: Regional Studies*, **15**, 171–183. URL: https://www.sciencedirect.com/science/article/pii/S2214581817302513.

Alaoui, A., Caduff, U., Gerke, H. and Weingartner, R. (2011) Preferential Flow Effects on Infiltration and Runoff in Grassland and Forest Soils. *Vadose Zone Journal*, **10**, 367–377. URL: https://acsess.onlinelibrary.wiley.com/doi/full/10.2136/vzj2010.0076.

Alexander, P. J., Mills, G. and Fealy, R. (2015) Using LCZ data to run an urban energy balance model. *Urban Climate*, **13**, 14–37. URL: https://www.sciencedirect.com/science/article/abs/pii/S2212095515000152.

Anderson, H. W., Hoover, M. D. and Reinhart, K. G. (1976) Forests and water: effects of forest management on floods, sedimentation, and water supply. *General Technical Report PSW-018. Berkeley, CA: U.S. Department of Agriculture, Forest Service, Pacific Southwest Forest and Range Experiment Station.* URL: https://www.fs.usda.gov/research/treesearch/24048.

Anon (2022) 3D building model NW LoD1. Last access: 03.06.2023. URL: https://data.europa.eu/data/datasets/c9a7710a-f2bf-447b-8c57-078dcd228f9a~~1?locale=en.

Arakawa, A. and Lamb, V. R. (1977) Computational Design of the Basic Dynamical Processes of the UCLA General Circulation Model. *Methods in Computational*

Physics, **17**, 173–265. URL: https://www.sciencedirect.com/science/article/pii/B9780124608177500094.

Armson, D., Stringer, P. and Ennos, A. (2013) The effect of street trees and amenity grass on urban surface water runoff in Manchester, UK. *Urban Forestry and Urban Greening*, **12**, 282–286. URL: https://www.sciencedirect.com/science/article/abs/pii/S1618866713000460.

Arnfield, A. J. (2003) Two decades of urban climate research: a review of turbulence, exchanges of energy and water, and the urban heat island. *International Journal of Climatology*, **23**, 1–26. URL: https://rmets.onlinelibrary.wiley.com/doi/10.1002/joc.859.

Aylor, D. E., Wang, Y. and Miller, D. R. (1993) Intermittent wind close to the ground within a grass canopy. *Boundary-Layer Meteorology*, **66**, 427–448. URL: https://link.springer.com/article/10.1007/BF00712732.

Baklanov, A., Grimmond, C., Carlson, D., Terblanche, D., Tang, X., Bouchet, V., Lee, B., Langendijk, G., Kolli, R. and Hovsepyan, A. (2018) From urban meteorology, climate and environment research to integrated city services. *Urban Climate*, **23**, 330–341. URL: https://www.sciencedirect.com/science/article/pii/S2212095517300408. ICUC9: The 9th International Conference on Urban Climate.

Baldocchi, D. D., Law, B. E. and Anthoni, P. M. (2000) On measuring and modeling energy fluxes above the floor of a homogeneous and heterogeneous conifer forest. *Agricultural and Forest Meteorology*, **102**, 187–206. URL: https://www.sciencedirect.com/science/article/pii/S0168192300000988.

Baldocchi, D. D., Xu, L. and Kiang, N. Y. (2004) How plant functional-type, weather, seasonal drought, and soil physical properties alter water and energy fluxes of an oak-grass savanna and an annual grassland. *Agric. Forest Meteorol.*, **123**, 13–39. URL: https://www.sciencedirect.com/science/article/abs/pii/S0168192303002739.

Barlow, J. F. (2014) Progress in observing and modelling the urban boundary layer. *Urban Climate*, **10**, 216–240. URL: https://www.sciencedirect.com/science/article/pii/S2212095514000558. ICUC8: The 8th International Conference on Urban Climate and the 10th Symposium on the Urban Environment.

Bauer, H.-S. and Wulfmeyer, V. (2009) Validation of components of the water cycle in the ECHAM4 general circulation model based on the Newtonian relaxation technique:

a case study of an intense winter cyclone. *Meteorology and Atmospheric Physics*, **104**, 135–162. URL: https://doi.org/10.1007/s00703-009-0018-7.

Baumbach, G. and Vogt, U. (2003) Influence of inversion layers on the distribution of air pollutants in urban areas. *Water, Air, & Soil Pollution: Focus*, **3**, 65–76. URL: https://link.springer.com/article/10.1023/A:1026098305581.

Bechtel, B., Alexander, P. J., Beck, C., Böhner, J., Brousse, O., Ching, J., Demuzere, M., Fonte, C., Gál, T., Hidalgo, J., Hoffmann, P., Middel, A., Mills, G., Ren, C., See, L., Sismanidis, P., Verdonck, M.-L., Xu, G. and Xu, Y. (2019) Generating WUDAPT Level 0 data – Current status of production and evaluation. *Urban Climate*, **27**, 24 – 45. URL: http://www.sciencedirect.com/science/article/pii/S221209551830302X.

Bechtel, B., Alexander, P. J., Böhner, J., Ching, J., Conrad, O., Feddema, J., Mills, G., See, L. and Stewart, I. (2015) Mapping Local Climate Zones for a Worldwide Database of the Form and Function of Cities. *ISPRS International Journal of Geo-Information*, **4**, 199–219. URL: https://www.mdpi.com/2220-9964/4/1/199.

Berardi, U., Jandaghian, Z. and Graham, J. (2020) Effects of greenery enhancements for the resilience to heat waves: A comparison of analysis performed through mesoscale (wrf) and microscale (envi-met) modeling. *Science of The Total Environment*, **747**, 141300. URL: https://www.sciencedirect.com/science/article/pii/S0048969720348294.

BKG (2012) Digitales Landbedeckungsmodell für Deutschland, Stand 2012 (LBM-DE2012). Bundesamt für Kartographie und Geodäsie. Last access: 03.06.2023. URL: https://gdz.bkg.bund.de/index.php/default/digitales-landbedeckungsmodell-fur-deutschland-stand-2012-lbm-de2012.html.

— (2020) 3D-Gebäudemodelle LoD1-DE Hamburg. Bundesamt für Kartographie und Geodäsie. Last access: 03.06.2023. URL: https://mis.bkg.bund.de/trefferanzeige?docuuid=6E7107C6-A9F0-4373-A906-A33E43C1117D.

Blankenstein, S. and Kuttler, W. (2004) Impact of street geometry on downward longwave radiation and air temperature in an urban environment. *Meteorologische Zeitschrift*, **13**, 373–379. URL: https://www.schweizerbart.de/papers/metz/detail/13/53321/Impact_of_street_geometry_on_downward_longwave_radiation_and_air_temperature_in_an_urban_environment.

Bohnenstengel, S. I., Hamilton, I., Davies, M. and Belcher, S. E. (2014) Impact of anthropogenic heat emissions on London's temperatures. *Quarterly Journal of the Royal Meteorological Society*, **140**, 687–698. URL: https://rmets.onlinelibrary.wiley.com/doi/abs/10.1002/qj.2144.

Bollmeyer, C., Keller, J. D., Ohlwein, C., Wahl, S., Crewell, S., Friederichs, P., Hense, A., Keune, J., Kneifel, S., Pscheidt, I., Redl, S. and Steinke, S. (2015) Towards a high-resolution regional reanalysis for the European CORDEX domain. *Quarterly Journal of the Royal Meteorological Society*, **141**, 1–15. URL: https://rmets.onlinelibrary.wiley.com/doi/abs/10.1002/qj.2486.

Bonan, G. B. (2008) Forests and climate change: Forcings, feedbacks, and the climate benefits of forests. *Science*, **320**, 1444–1449. URL: https://www.science.org/doi/10.1126/science.1155121.

Bonan, G. B., Patton, E. G., Harman, I. N., Oleson, K. W., Finnigan, J. J., Lu, Y. and Burakowski, E. A. (2018) Modeling canopy-induced turbulence in the Earth system: A unified parameterization of turbulent exchange within plant canopies and the roughness sublayer (CLM-ml v0). *Geoscientific Model Development*, **11**, 1467–1496. URL: https://gmd.copernicus.org/articles/11/1467/2018/.

Bowne, N. E. and Ball, J. T. (1970) Observational comparison of rural and urban boundary layer turbulence. *Journal of Applied Meteorology (1962-1982)*, **9**, 862–873. URL: http://www.jstor.org/stable/26174935.

Boyd, M. J., Bufill, M. C. and Knee, R. M. (1994) Predicting pervious and impervious storm runoff from urban drainage basins. *Hydrological Sciences Journal*, **39**, 321–332. URL: https://www.tandfonline.com/doi/abs/10.1080/02626669409492753.

Boysen, L. R., Brovkin, V., Pongratz, J., Lawrence, D. M., Lawrence, P., Vuichard, N., Peylin, P., Liddicoat, S., Hajima, T., Zhang, Y., Rocher, M., Delire, C., Séférian, R., Arora, V. K., Nieradzik, L., Anthoni, P., Thiery, W., Laguë, M. M., Lawrence, D. and Lo, M.-H. (2020) Global climate response to idealized deforestation in CMIP6 models. *Biogeosciences*, **17**, 5615–5638. URL: https://bg.copernicus.org/articles/17/5615/2020/.

Breil, M., Davin, E. L. and Rechid, D. (2021) What determines the sign of the evapotranspiration response to afforestation in European summer? *Biogeosciences*, **18**, 1499–1510. URL: https://bg.copernicus.org/articles/18/1499/2021/.

Brill, K. F., Uccellini, L. W., Manobianco, J., Kocin, P. J. and Homan, J. H. (1991) The use of successive dynamic initialization by nudging to simulate cyclogenesis during GALE IOP 1. *Meteorology and Atmospheric Physics*, **45**, 15–40. URL: https://doi.org/10.1007/BF01027473.

Brown, M. J. (2000) *Urban Parameterizations for Mesoscale Meteorological Models*, 193–255. Z. Boybeyi, Ed., Wessex Press.

Bullock, O. R., Alapaty, K., Herwehe, J. A., Mallard, M. S., Otte, T. L., Gilliam, R. C. and Nolte, C. G. (2014) An Observation-Based Investigation of Nudging in WRF for Downscaling Surface Climate Information to 12-km Grid Spacing. *Journal of Applied Meteorology and Climatology*, **53**, 20 – 33. URL: https://journals.ametsoc.org/view/journals/apme/53/1/jamc-d-13-030.1.xml.

Böttcher, M. (2017) *Selected climate mitigation and adaptation measures and their impact on the climate of the region of Hamburg*. Ph.D. thesis, University of Hamburg.

Chameides, W. L., Lindsay, R. W., Richardson, J. and Kiang, C. S. (1988) The Role of Biogenic Hydrocarbons in Urban Photochemical Smog: Atlanta as a Case Study. *Science*, **241**, 1473–1475. URL: https://www.science.org/doi/10.1126/science.3420404.

Chen, B., Dong, L., Liu, X., Shi, G. Y., Chen, L., Nakajima, T. and Habib, A. (2016) Exploring the possible effect of anthropogenic heat release due to global energy consumption upon global climate: a climate model study. *International Journal of Climatology*, **36**, 4790–4796. URL: https://rmets.onlinelibrary.wiley.com/doi/abs/10.1002/joc.4669.

Cheng, G. and Schlünzen, K. H. (2023) A conceptual model for a generalized canopy parametrization for atmospheric models. *Quarterly Journal of the Royal Meteorological Society*, **149**, 494–514. URL: https://rmets.onlinelibrary.wiley.com/doi/abs/10.1002/qj.4420.

Cheng, G., Schlünzen, K. H., Grawe, D., Voss, V., Thatcher, M. and Rayner, P. (2023) Parameterizing building effects on airflows within the urban canopy layer for high-resolution models using a nudging approach. *Quarterly Journal of the Royal Meteorological Society*, **149**, 2617–2633. URL: https://rmets.onlinelibrary.wiley.com/doi/abs/10.1002/qj.4524.

Chin, H.-N. S., Leach, M. J., Sugiyama, G. A., Leone, J. M., Walker, H., Nasstrom, J. S. and Brown, M. J. (2005) Evaluation of an Urban Canopy Parameterization in a Mesoscale Model Using VTMX and URBAN 2000 Data. *Monthly Weather Review*, **133**, 2043–2068. URL: https://journals.ametsoc.org/view/journals/mwre/133/7/mwr2962.1.xml.

Ching, J., Aliaga, D., Mills, G., Masson, V., See, L., Neophytou, M., Middel, A., Baklanov, A., Ren, C., Ng, E., Fung, J., Wong, M., Huang, Y., Martilli, A., Brousse, O., Stewart, I., Zhang, X., Shehata, A., Miao, S., Wang, X., Wang, W., Yamagata, Y., Duarte, D., Li, Y., Feddema, J., Bechtel, B., Hidalgo, J., Roustan, Y., Kim, Y. S., Simon, H., Kropp, T., Bruse, M., Lindberg, F., Grimmond, S., Demuzure, M., Chen, F., Li, C., Gonzales-Cruz, J., Bornstein, B., He, Q., Tzu-Ping, Hanna, A., Erell, E., Tapper, N., Mall, R. K. and Niyogi, D. (2019) Pathway using WUDAPT's Digital Synthetic City tool towards generating urban canopy parameters for multi-scale urban atmospheric modeling. *Urban Climate*, **28**. URL: https://www.sciencedirect.com/science/article/abs/pii/S2212095519300975.

Ching, J., Mills, G., Bechtel, B., See, L., Feddema, J., Wang, X., Ren, C., Brousse, O., Martilli, A., Neophytou, M., Mouzourides, P., Stewart, I., Hanna, A., Ng, E., Foley, M., Alexander, P., Aliaga, D., Niyogi, D., Shreevastava, A., Bhalachandran, P., Masson, V., Hidalgo, J., Fung, J., Andrade, M., Baklanov, A., Dai, W., Milcinski, G., Demuzere, M., Brunsell, N., Pesaresi, M., Miao, S., Mu, Q., Chen, F. and Theeuwes, N. (2018) WUDAPT: An Urban Weather, Climate, and Environmental Modeling Infrastructure for the Anthropocene. *Bulletin of the American Meteorological Society*, **99**, 1907 – 1924. URL: https://journals.ametsoc.org/view/journals/bams/99/9/bams-d-16-0236.1.xml.

Cho, E., Yoo, C., Kang, M., Song, S.-u. and Kim, S. (2020) Experiment of wind-driven-rain measurement on building walls and its in-situ validation. *Building and Environment*, **185**, 107269. URL: https://www.sciencedirect.com/science/article/pii/S0360132320306405.

Choi, H.-J., Lee, H. W., Sung, K.-H., Kim, M.-J., Kim, Y.-K. and Jung, W.-S. (2009) The impact of nudging coefficient for the initialization on the atmospheric flow field and the photochemical ozone concentration of Seoul, Korea. *Atmospheric Environment*, **43**, 4124–4136. URL: https://www.sciencedirect.com/science/article/pii/S1352231009004907.

Christen, A. and Vogt, R. (2004) Energy and radiation balance of a central european city. *International Journal of Climatology*, **24**, 1395–1421. URL: https://rmets.onlinelibrary.wiley.com/doi/abs/10.1002/joc.1074.

Cichowicz, R., Wielgosiński, G. and Fetter, W. (2017) Dispersion of atmospheric air pollution in summer and winter season. *Environmental Monitoring and Assessment*, **189**, 605. URL: https://doi.org/10.1007/s10661-017-6319-2.

Cleugh, H. and Grimmond, S. (2012) Urban Climates and Global Climate Change. In *The Future of the World's Climate* (eds. A. Henderson-Sellers and K. McGuffie), 47–76. Elsevier.

Coceal, O. and Belcher, S. E. (2005) Mean Winds Through an Inhomogeneous Urban Canopy. *Boundary-Layer Meteorology*, **115**, 47–68. URL: https://link.springer.com/article/10.1007/s10546-004-1591-4.

Conrad, O., Bechtel, B., Bock, M., Dietrich, H., Fischer, E., Gerlitz, L., Wehberg, J., Wichmann, V. and Böhner, J. (2015) System for Automated Geoscientific Analyses (SAGA) v. 2.1.4. *Geoscientific Model Development*, **8**, 1991–2007. URL: https://gmd.copernicus.org/articles/8/1991/2015/.

D'Amato, G., Cecchi, L., D'Amato, M. and Liccardi, G. (2010) Urban Air Pollution and Climate Change as Environmental Risk Factors of Respiratory Allergy: An Update. *Journal of investigational allergology and clinical immunology*, **20**, 95–102;.

Davies, H. C. (1976) A lateral boundary formulation for multi-level prediction models. *Quarterly Journal of the Royal Meteorological Society*, **102**, 405–418. URL: https://rmets.onlinelibrary.wiley.com/doi/abs/10.1002/qj.49710243210.

Deardorff, J. W. (1978) Efficient prediction of ground surface temperature and moisture, with inclusion of a layer of vegetation. *Journal of Geophysical Research: Oceans*, **83**, 1889–1903. URL: https://agupubs.onlinelibrary.wiley.com/doi/10.1029/JC083iC04p01889.

Demuzere, M., Kittner, J., Martilli, A., Mills, G., Moede, C., Stewart, I. D., van Vliet, J. and Bechtel, B. (2022) A global map of local climate zones to support earth system modelling and urban-scale environmental science. *Earth Syst. Sci. Data*, **14**, 3835–3873. URL: https://doi.org/10.5194/essd-14-3835-2022.

Dickinson, R. E., Henderson-Sellers, A.and Kennedy, P. J. and Wilson, M. F. (1986) *Biosphere-atmosphere Transfer Scheme (BATS) for the NCAR Community Climate Model (No. NCAR/TN-275-+STR)*. University Corporation for Atmospheric Research. URL: http://dx.doi.org/10.5065/D6668B58.

Dierer, S. and Schlünzen, K. H. (2005b) Influence parameters for a polar mesocyclone development. *Meteorologische Zeitschrift*, **14**, 781–792. URL: http://dx.doi.org/10.1127/0941-2948/2005/0077.

Dierer, S., Schlünzen, K. H., Birnbaum, G., Brümmer, B. and Müller, G. (2005a) Atmosphere–Sea Ice Interactions during a Cyclone Passage Investigated by Using Model Simulations and Measurements. *Monthly Weather Review*, **133**, 3678 – 3692. URL: https://journals.ametsoc.org/view/journals/mwre/133/12/mwr3076.1.xml.

Dong, Y., Varquez, A. and Kanda, M. (2017) Global anthropogenic heat flux database with high spatial resolution. *Atmospheric Environment*, **150**, 276–294. URL: https://www.sciencedirect.com/science/article/pii/S1352231016309232.

Dukai, B., Ledoux, H. and Stoter, J. (2019) A multi-height LoD1 model of all buildings in the Netherlands. *ISPRS Ann. Photogramm. Remote Sens. Spat. Inf. Sci*, **4**, 51–57. URL: https://isprs-annals.copernicus.org/articles/IV-4-W8/51/2019/.

Dupont, S., Otte, T. L. and Ching, J. K. S. (2004) Simulation of Meteorological Fields Within and Above Urban and Rural Canopies with a Mesoscale Model. *Boundary-Layer Meteorology*, **113**, 111–158. URL: https://link.springer.com/article/10.1023/B:BOUN.0000037327.19159.ac.

Eisenman, T. S., Churkina, G., Jariwala, S. P., Kumar, P., Lovasi, G. S., Pataki, D. E., Weinberger, K. R. and Whitlow, T. H. (2019) Urban trees, air quality, and asthma: An interdisciplinary review. *Landscape and Urban Planning*, **187**, 47–59. URL: https://doi.org/10.1016/j.landurbplan.2019.02.010.

Ellison, D., Morris, C. E., Locatelli, B., Sheil, D., Cohen, J., Murdiyarso, D., Gutierrez, V., van Noordwijk, M., Creed, I. F., Pokorny, J., Gaveau, D., Spracklen, D. V., Tobella, A. B., Ilstedt, U., Teuling, A. J., Gebrehiwot, S. G., Sands, D. C., Muys, B., Verbist, B., Springgay, E., Sugandi, Y. and Sullivan, C. A. (2017) Trees, forests and water: Cool insights for a hot world. *Global Environmental Change*, **43**, 51–61. URL: https://doi.org/10.1016/j.gloenvcha.2017.01.002.

ESA (2010) ESA Data User Element (GlobCover Land Cover Maps). Last access: 03.06.2023. URL: http://due.esrin.esa.int/page_globcover.php.

Essery, R., Pomeroy, J., Ellis, C. and Link, T. (2008) Modelling longwave radiation to snow beneath forest canopies using hemispherical photography or linear regression. *Hydrological Processes*, **22**, 2788–2800. URL: https://onlinelibrary.wiley.com/doi/abs/10.1002/hyp.6930.

European Environment Agency (EEA) (2018) Urban-Atlas 2018 and Street Tree Layer (STL) 2018. URL: https://land.copernicus.eu/local/urban-atlas.

FAO (2020) Global Forest Resources Assessment 2020: Main report. Rome. URL: https://doi.org/10.4060/ca9825en.

Fenger, J. (1999) Urban air quality. *Atmospheric Environment*, **33**, 4877 – 4900. URL: https://doi.org/10.1016/S1352-2310(99)00290-3.

Ferner, K., Boettcher, M. and Schlünzen, K. (2022) Modelling the heterogeneity of rain in an urban neighbourhood with an obstacle-resolving model. *Meteorologische Zeitschrift*, –. URL: http://dx.doi.org/10.1127/metz/2022/1149.

Fitzky, A. C., Sandén, H., Karl, T., Fares, S., Calfapietra, C., Grote, R., Saunier, A. and Rewald, B. (2019) The Interplay Between Ozone and Urban Vegetation—BVOC Emissions, Ozone Deposition, and Tree Ecophysiology. *Frontiers in Forests and Global Change*, **2**. URL: https://www.frontiersin.org/articles/10.3389/ffgc.2019.00050/full.

Garuma, G. F. (2018) Review of urban surface parameterizations for numerical climate models. *Urban Climate*, **24**, 830–851. URL: https://www.sciencedirect.com/science/article/pii/S2212095517300858.

Grawe, D. and Schlünzen, K. H. (2018) Preparation of land–cover and orography data for GRITOP-L. METRAS Technical Report 12. Last access: 03.06.2023. URL: https://www.mi.uni-hamburg.de/en/arbeitsgruppen/memi/modelle/metras-pcl/metras-pcl-download/gritop-l-data-1-0-0.pdf.

Grawe, D., Schlünzen, K. H. and Pascheke, F. (2013a) Comparison of results of an obstacle resolving microscale model with wind tunnel data. *Atmospheric Environment*, **79**, 495–509. URL: https://www.sciencedirect.com/science/article/pii/S1352231013004974.

Grawe, D., Thompson, H. L., Salmond, J. A., Cai, X.-M. and Schlünzen, K. H. (2013b) Modelling the impact of urbanisation on regional climate in the Greater London Area. *International Journal of Climatology*, **33**, 2388–2401. URL: https://rmets.onlinelibrary.wiley.com/doi/abs/10.1002/joc.3589.

Grimmond, C., Best, M., Barlow, J., Arnfield, A. J., Baik, J.-J., Baklanov, A., Belcher, S., Bruse, M., Calmet, I., Chen, F., Clark, P., Dandou, A., Erell, E., Fortuniak, K., Hamdi, R., Kanda, M., Kawai, T., Kondo, H., Krayenhoff, S., Lee, S. H., Limor, S.-B., Martilli, A., Masson, V., Miao, S., Mills, G., Moriwaki, R., Oleson, K., Porson, A., Sievers, U., Tombrou, M., Voogt, J. and Williamson, T. (2009) Urban Surface Energy Balance Models: Model Characteristics and Methodology for a Comparison Study. In *Meteorological and Air Quality Models for Urban Areas* (eds. A. Baklanov, S. Grimmond, M. Alexander and M. Athanassiadou), 97–123. Berlin, Heidelberg: Springer Berlin Heidelberg. URL: https://link.springer.com/chapter/10.1007/978-3-642-00298-4_11.

Grimmond, C. S. B. and Oke, T. R. (1991) An Evapotranspiration-Interception Model for Urban Areas. *Water Resources Research*. URL: https://agupubs.onlinelibrary.wiley.com/doi/abs/10.1029/91WR00557.

— (1999) Heat Storage in Urban Areas: Local-Scale Observations and Evaluation of a Simple Model. *Journal of Applied Meteorology*, **38**, 922–940. URL: https://journals.ametsoc.org/view/journals/apme/38/7/1520-0450_1999_038_0922_hsiual_2.0.co_2.xml.

Gronemeier, T., Surm, K., Harms, F., Leitl, B., Maronga, B. and Raasch, S. (2021) Evaluation of the dynamic core of the palm model system 6.0 in a neutrally stratified urban environment: comparison between les and wind-tunnel experiments. *Geoscientific Model Development*, **14**, 3317–3333. URL: https://gmd.copernicus.org/articles/14/3317/2021/.

Grøntoft, T. and Raychaudhuri, M. R. (2004) Compilation of tables of surface deposition velocities for O_3, NO_2 and SO_2 to a range of indoor surfaces. *Atmospheric Environment*, **38**, 533–544. URL: https://www.sciencedirect.com/science/article/pii/S1352231003008732.

Gustafsson, D., Lewan, E., van den Hurk, B. J., Viterbo, P., Grelle, A., Lindroth, A., Cienciala, E., Mölder, M., Halldin, S. and Lundin, L. C. (2003) Boreal forest surface parameterization in the ECMWF model - 1D test with NOPEX long-term data. *Journal*

of Applied Meteorology, **42**, 95–112. URL: https://journals.ametsoc.org/view/journals/apme/42/1/1520-0450_2003_042_0095_bfspit_2.0.co_2.xml.

Haarsma, R. J., Roberts, M. J., Vidale, P. L., Senior, C. A., Bellucci, A., Bao, Q., Chang, P., Corti, S., Fučkar, N. S., Guemas, V., von Hardenberg, J., Hazeleger, W., Kodama, C., Koenigk, T., Leung, L. R., Lu, J., Luo, J.-J., Mao, J., Mizielinski, M. S., Mizuta, R., Nobre, P., Satoh, M., Scoccimarro, E., Semmler, T., Small, J. and von Storch, J.-S. (2016) High Resolution Model Intercomparison Project (HighResMIP v1.0) for CMIP6. *Geoscientific Model Development*, **9**, 4185–4208. URL: https://gmd.copernicus.org/articles/9/4185/2016/.

Hamdi, R. and Masson, V. (2008) Inclusion of a Drag Approach in the Town Energy Balance (TEB) Scheme: Offline 1D Evaluation in a Street Canyon. *Journal of Applied Meteorology and Climatology*, **47**, 2627–2644. URL: https://journals.ametsoc.org/view/journals/apme/47/10/2008jamc1865.1.xml.

Han, J.-Y., Baik, J.-J. and Lee, H. (2014) Urban impacts on precipitation. *Asia-Pacific Journal of the Atmospheric Sciences*, **50**. URL: https://link.springer.com/article/10.1007/s13143-014-0016-7.

Haneef, S., Johnson, J., Dickinson, C., Thompson, G. and Wood, G. (1992) Effect of dry deposition of NO_x and SO_2 gaseous pollutants on the degradation of calcareous building stones. *Atmospheric Environment. Part A. General Topics*, **26**, 2963–2974. URL: https://www.sciencedirect.com/science/article/pii/096016869290288V.

Hardy, J., RA, M., Koenig, G., Marks, D., Winstral, A., Pomeroy, J. and Link, T. (2004) Solar Radiation Transmission Through Conifer Canopies. *Agricultural and Forest Meteorology*, **126**, 257–270. URL: https://www.sciencedirect.com/science/article/abs/pii/S0168192304001698.

Haverd, V., Cuntz, M. O., Leuning, R. and Keith, H. (2007) Air and biomass heat storage fluxes in a forest canopy: Calculation within a soil vegetation atmosphere transfer model. *Agricultural and Forest Meteorology*, **147**, 125–39. URL: https://www.sciencedirect.com/science/article/abs/pii/S0168192307001876.

He, K., Huo, H. and Zhang, Q. (2002) Urban Air Pollution in China: Current Status, Characteristics, and Progress. *Annual Review of Energy and the Environment*, **27**, 397–431. URL: https://doi.org/10.1146/annurev.energy.27.122001.083421.

Helbig, M., Gerken, T., Beamesderfer, E. R., Baldocchi, D. D., Banerjee, T., Biraud, S. C., Brown, W. O., Brunsell, N. A., Burakowski, E. A., Burns, S. P., Butterworth, B. J., Chan, W. S., Davis, K. J., Desai, A. R., Fuentes, J. D., Hollinger, D. Y., Kljun, N., Mauder, M., Novick, K. A., Perkins, J. M., Rahn, D. A., Rey-Sanchez, C., Santanello, J. A., Scott, R. L., Seyednasrollah, B., Stoy, P. C., Sullivan, R. C., de Arellano, J. V.-G., Wharton, S., Yi, C. and Richardson, A. D. (2021) Integrating continuous atmospheric boundary layer and tower-based flux measurements to advance understanding of land-atmosphere interactions. *Agricultural and Forest Meteorology*, **307**, 108509. URL: https://www.sciencedirect.com/science/article/pii/S0168192321001933.

Henderson-Sellers, A. (1993) A Factorial Assessment of the Sensitivity of the BATS Land-Surface Parameterization Scheme. *Journal of Climate*, **6**, 227 – 247. URL: https://journals.ametsoc.org/view/journals/clim/6/2/1520-0442_1993_006_0227_afaots_2_0_co_2.xml.

Hertwig, D., Efthimiou, G. C., Bartzis, J. G. and Leitl, B. (2012) CFD-RANS model validation of turbulent flow in a semi-idealized urban canopy. *Journal of Wind Engineering and Industrial Aerodynamics*, **111**, 61–72. URL: https://www.sciencedirect.com/science/article/pii/S0167610512002474.

Hoek van Dijke, A. J., Herold, M., Mallick, K., Benedict, I., Machwitz, M., Schlerf, M., Pranindita, A., Theeuwen, J. J. E., Bastin, J.-F. and Teuling, A. J. (2022) Shifts in regional water availability due to global tree restoration. *Nature Geoscience*, **15**, 363–368. URL: https://doi.org/10.1038/s41561-022-00935-0.

Hoffmann, P., Krueger, O. and Schlünzen, K. H. (2012) A statistical model for the urban heat island and its application to a climate change scenario. *International Journal of Climatology*, **32**, 1238–1248. URL: https://rmets.onlinelibrary.wiley.com/doi/abs/10.1002/joc.2348.

Hoffmann, P., Schoetter, R. and Schlünzen, H. (2018) Statistical-dynamical downscaling of the urban heat island in Hamburg, Germany. *Meteorologische Zeitschrift*, **27**, 89–109. URL: https://www.schweizerbart.de/papers/metz/detail/27/87180/Statistical_dynamical_downscaling_of_the_urban_heat_island_in_Hamburg_Germany.

Hoke, J. E. and Anthes, R. A. (1976) The initialization of numerical models by a dynamic-initialization technique. *Monthly Weather Review*, **104**, 1551

– 1556. URL: https://journals.ametsoc.org/view/journals/mwre/104/12/1520-0493_1976_104_1551_tionmb_2_0_co_2.xml.

Holst, J. and Mayer, H. (2006) Comparative analysis of albedo and surface energy balance of a grassland site and an adjacent Scots pine forest. *Climate Research*, **30**, 227–237. URL: https://doi.org/10.3354/cr030227.

IPCC (2022) Climate Change 2022: Impacts, Adaptation, and Vulnerability. Contribution of Working Group II to the Sixth Assessment Report of the Intergovernmental Panel on Climate Change [H.-O. Pörtner, D.C. Roberts, M. Tignor, E.S. Poloczanska, K. Mintenbeck, A. Alegría, M. Craig, S. Langsdorf, S. Löschke, V. Möller, A. Okem, B. Rama (eds.)] Cambridge University Press. Cambridge University Press, Cambridge, UK and New York, NY, USA, 90-1040 pp., doi:10.1017/9781009325844.

Jackson, T. L., Feddema, J. J., Oleson, K. W., Bonan, G. B. and Bauer, J. T. (2010) Parameterization of urban characteristics for global climate modeling. *Annals of the Association of American Geographers*, **100**, 848–865. URL: http://www.jstor.org/stable/40863606.

Jin, K., Wang, F., Chen, D., Liu, H., Ding, W. and Shi, S. (2019) A new global gridded anthropogenic heat flux dataset with high spatial resolution and long-term time series. *Scientific Data*, **6**, 139. URL: https://doi.org/10.1038/s41597-019-0143-1.

Kanda, M., Kawai, T., Kanega, M., Moriwaki, R., Narita, K. and Hagishima, A. (2005) A simple energy balance model for regular building arrays. *Boundary-Layer Meteorology*, **116**, 423–443. URL: https://link.springer.com/article/10.1007/s10546-004-7956-x.

Kastner-Klein, P. and Rotach, M. W. (2004) Mean flow and turbulence characteristics in an urban roughness sublayer. *Boundary-Layer Meteorology*, **111**, 55–84. URL: https://doi.org/10.1023/B:BOUN.0000010994.32240.b1.

Katzfey, J., Schlünzen, H., Hoffmann, P. and Thatcher, M. (2020) How an urban parameterization affects a high-resolution global climate simulation. *Quarterly Journal of the Royal Meteorological Society*, **146**, 3808–3829. URL: https://rmets.onlinelibrary.wiley.com/doi/abs/10.1002/qj.3874.

Kirsch, B., Hohenegger, C., Klocke, D., Senke, R., Offermann, M. and Ament, F. (2022) Sub-mesoscale observations of convective cold pools with a dense station network in

Hamburg, Germany. *Earth System Science Data*, **14**, 3531–3548. URL: https://essd.copernicus.org/articles/14/3531/2022/.

Klumpp, A., Ansel, W., Klumpp, G., Calatayud, V., Pierre Garrec, J., He, S., Peñuelas, J., Ribas, À., Ro-Poulsen, H., Rasmussen, S., Sanz, M. J. and Vergne, P. (2006) Ozone pollution and ozone biomonitoring in European cities. Part I: Ozone concentrations and cumulative exposure indices at urban and suburban sites. *Atmospheric Environment*, **40**, 7963–7974. URL: https://doi.org/10.1016/j.atmosenv.2006.07.017.

Knyazikhin, Y., Martonchik, J. V., Myneni, R. B., Diner, D. J. and Running, S. W. (1998) Synergistic algorithm for estimating vegetation canopy leaf area index and fraction of absorbed photosynthetically active radiation from MODIS and MISR data. *Journal of Geophysical Research: Atmospheres*, **103**, 32257–32275. URL: https://agupubs.onlinelibrary.wiley.com/doi/pdf/10.1029/98JD02462.

Koopmans, S., van Haren, R., Theeuwes, N., Ronda, R., Uijlenhoet, R., Holtslag, A. A. M. and Steeneveld, G.-J. (2023) The set-up and evaluation of fine-scale data assimilation for the urban climate of amsterdam. *Quarterly Journal of the Royal Meteorological Society*, **149**, 171–191. URL: https://rmets.onlinelibrary.wiley.com/doi/abs/10.1002/qj.4401.

Korsholm, U. S., Petersen, C., Sass, B. H., Nielsen, N. W., Jensen, D. G., Olsen, B. T., Gill, R. and Vedel, H. (2015) A new approach for assimilation of 2D radar precipitation in a high-resolution NWP model. *Meteorological Applications*, **22**, 48–59. URL: https://rmets.onlinelibrary.wiley.com/doi/abs/10.1002/met.1466.

Kotthaus, S. and Grimmond, C. (2014) Energy exchange in a dense urban environment – Part I: Temporal variability of long-term observations in central London. *Urban Climate*, **10**, 261–280. URL: https://doi.org/10.1016/j.uclim.2013.10.002. ICUC8: The 8th International Conference on Urban Climate and the 10th Symposium on the Urban Environment.

Krayenhoff, E. S., Christen, A., Martilli, A. and Oke, T. R. (2014) A Multi-layer Radiation Model for Urban Neighbourhoods with Trees. *Boundary-Layer Meteorology*, **151**, 139–178. URL: https://link.springer.com/article/10.1007/s10546-013-9883-1.

Krayenhoff, E. S., Jiang, T., Christen, A., Martilli, A., Oke, T. R., Bailey, B. N., Nazarian, N., Voogt, J. A., Giometto, M. G., Stastny, A. and Crawford, B. R. (2020) A multi-layer urban canopy meteorological model with trees (BEP-Tree): Street tree

impacts on pedestrian-level climate. *Urban Climate*, **32**, 100590. URL: https://www.sciencedirect.com/science/article/abs/pii/S2212095519302640.

Kruse, C. G., Bacmeister, J. T., Zarzycki, C. M., Larson, V. E. and Thayer-Calder, K. (2022) Do nudging tendencies depend on the nudging timescale chosen in atmospheric models? *Journal of Advances in Modeling Earth Systems*, **14**, e2022MS003024. URL: https://agupubs.onlinelibrary.wiley.com/doi/abs/10.1029/2022MS003024.

Kusaka, H., Kondo, H., Kikegawa, Y. and Kimura, F. (2001) A Simple Single-Layer Urban Canopy Model For Atmospheric Models: Comparison With Multi-Layer And Slab Models. *Boundary-Layer Meteorology*, **101**, 329–358. URL: https://link.springer.com/article/10.1023/a:1019207923078.

Källberg, P. (1977) Test of a lateral boundary relaxation scheme in a barotropic model. ECMWF, Research Department, Internal Report, Bracknell, 3.

Lawler, R. R. and Link, T. E. (2011) Quantification of incoming all-wave radiation in discontinuous forest canopies with application to snowmelt prediction. *Hydrological Processes*, **25**, 3322–3331. URL: https://onlinelibrary.wiley.com/doi/pdf/10.1002/hyp.8150.

Lawrence, D. and Vandecar, K. (2015) Effects of tropical deforestation on climate and agriculture. *Nature Climate Change*, **5**, 27–36. URL: https://doi.org/10.1038/nclimate2430.

Lee, H., Mayer, H. and Chen, L. (2016a) Contribution of trees and grasslands to the mitigation of human heat stress in a residential district of Freiburg, Southwest Germany. *Landscape and Urban Planning*, **148**, 37–50. URL: https://www.sciencedirect.com/science/article/pii/S0169204615002467.

Lee, S.-H., Lee, H., Park, S.-B., Woo, J.-W., Lee, D.-I. and Baik, J. J. (2016b) Impacts of in-canyon vegetation and canyon aspect ratio on the thermal environment of street canyons: numerical investigation using a coupled WRF-VUCM model. *Quarterly Journal of the Royal Meteorological Society*, **142**, 2562–2578. URL: https://rmets.onlinelibrary.wiley.com/doi/full/10.1002/qj.2847.

Lee, S.-H. and Park, S.-U. (2008) A Vegetated Urban Canopy Model for Meteorological and Environmental Modelling. *Boundary-Layer Meteorology*, **126**, 73–102. URL: https://link.springer.com/article/10.1007/s10546-007-9221-6.

Li, D., Sun, T., Liu, M., Yang, L., Wang, L. and Gao, Z. (2015) Contrasting responses of urban and rural surface energy budgets to heat waves explain synergies between urban heat islands and heat waves. *Environmental Research Letters*, **10**, 054009. URL: https://dx.doi.org/10.1088/1748-9326/10/5/054009.

Lindberg, F., Thorsson, S., Rayner, D. and Lau, K. (2016) The impact of urban planning strategies on heat stress in a climate-change perspective. *Sustainable Cities and Society*, **25**, 1–12. URL: https://www.sciencedirect.com/science/article/pii/S2210670716300579.

Lipson, M. J., Thatcher, M., Hart, M. A. and Pitman, A. (2018) A building energy demand and urban land surface model. *Quarterly Journal of the Royal Meteorological Society*, **144**, 1572–1590. URL: https://rmets.onlinelibrary.wiley.com/doi/abs/10.1002/qj.3317.

Liu, B. Y. and Jordan, R. C. (1960) The interrelationship and characteristic distribution of direct, diffuse and total solar radiation. *Solar Energy*, **4**, 1–19. URL: https://doi.org/10.1016/0038-092X(60)90062-1.

Liu, J. and Niyogi, D. (2019) Meta-analysis of urbanization impact on rainfall modification. *Scientific Reports*, **9**, 7301. URL: https://www.nature.com/articles/s41598-019-42494-2.

Liu, J., Yang, S., Ma, L., Bao, X., Wang, D. and Xu, D. (2013) An Initialization Scheme for Tropical Cyclone Numerical Prediction by Enhancing Humidity in Deep-Convection Region. *Journal of Applied Meteorology and Climatology*, **52**, 2260 – 2277. URL: https://journals.ametsoc.org/view/journals/apme/52/10/jamc-d-12-0310.1.xml.

Liu, Y., Liu, R. and Chen, J. M. (2012) Retrospective retrieval of long-term consistent global leaf area index (1981–2011) from combined AVHRR and MODIS data. *Journal of Geophysical Research: Biogeosciences*, **117**. URL: https://agupubs.onlinelibrary.wiley.com/doi/abs/10.1029/2012JG002084.

Lüpkes, C. and Schlünzen, K. H. (1996) Modelling the arctic convective boundary-layer with different turbulence parameterizations. *Boundary-Layer Meteorology*, **79**, 107–130. URL: https://doi.org/10.1007/BF00120077.

Martilli, A., Clappier, A. and Rotach, M. W. (2002) An Urban Surface Exchange Parameterisation for Mesoscale Models. *Boundary-Layer Meteorology*, **104**, 261–304. URL: https://link.springer.com/article/10.1023/A:1016099921195.

Martilli, A., Santiago, J. L. and Salamanca, F. (2015) On the representation of urban heterogeneities in mesoscale models. *Environmental Fluid Mechanics*, **15**, 305–328. URL: https://doi.org/10.1007/s10652-013-9321-4.

Masson, V. (2000) A physically-based scheme for the urban energy budget in atmospheric models. *Boundary-Layer Meteorology*, **94**, 357–397. URL: https://doi.org/10.1023/A:1002463829265.

— (2006) Urban surface modeling and the meso-scale impact of cities. *Theoretical and Applied Climatology*, **84**, 35–45. URL: https://doi.org/10.1007/s00704-005-0142-3.

Mayer, H. (1999) Air pollution in cities. *Atmospheric Environment*, **33**, 4029 – 4037. URL: https://doi.org/10.1016/S1352-2310(99)00144-2.

McCarthy, M. P., Best, M. J. and Betts, R. A. (2010) Climate change in cities due to global warming and urban effects. *Geophysical Research Letters*, **37**. URL: https://agupubs.onlinelibrary.wiley.com/doi/abs/10.1029/2010GL042845.

McNorton, J., Agustí-Panareda, A., Arduini, G., Balsamo, G., Bousserez, N., Boussetta, S., Chericoni, M., Choulga, M., Engelen, R. and Guevara, M. (2023) An urban scheme for the ecmwf integrated forecasting system: Global forecasts and residential co2 emissions. *Journal of Advances in Modeling Earth Systems*, **15**, e2022MS003286. URL: https://agupubs.onlinelibrary.wiley.com/doi/abs/10.1029/2022MS003286. E2022MS003286 2022MS003286.

Meier, R., Schwaab, J., Seneviratne, S. I., Sprenger, M., Lewis, E. and Davin, E. L. (2021) Empirical estimate of forestation-induced precipitation changes in Europe. *Nature Geoscience*, **14**, 473–478. URL: https://www.nature.com/articles/s41561-021-00773-6.

Mills, G. (1997) An urban canopy-layer climate model. *Theoretical and Applied Climatology*, **57**, 229–244. URL: https://link.springer.com/article/10.1007/bf00863615.

Mills, G.and Ching, J., See, L., Bechtel, B. and Foley, M. (2015) An Introduction to the WUDAPT project. 9th International Concerfence on Urban Climate, Toulouse. Last access: 03.06.2023. URL: https://www.wudapt.org/wp-content/uploads/2015/05/Mills_etal_ICUC9.pdf.

Miralles, D. G., Gash, J. H., Holmes, T. R. H., de Jeu, R. A. M. and Dolman, A. J. (2010) Global canopy interception from satellite observations. *Journal of Geophysical Research: Atmospheres*, **115**. URL: https://doi.org/10.1029/2009JD013530.

Moon, K., Duff, T. and Tolhurst, K. (2019) Sub-canopy forest winds: understanding wind profiles for fire behaviour simulation. *Fire Safety Journal*, **105**, 320 – 329. URL: https://doi.org/10.1016/j.firesaf.2016.02.005.

Moradi, M., Dyer, B., Nazem, A., Nambiar, M. K., Nahian, M. R., Bueno, B., Mackey, C., Vasanthakumar, S., Nazarian, N., Krayenhoff, E. S., Norford, L. K. and Aliabadi, A. A. (2021) The Vertical City Weather Generator (VCWG v1.3.2). *Geoscientific Model Development*, **14**, 961–984. URL: https://gmd.copernicus.org/articles/14/961/2021/.

Morakinyo, T. E., Dahanayake, K. K. C., Adegun, O. B. and Balogun, A. A. (2016) Modelling the effect of tree-shading on summer indoor and outdoor thermal condition of two similar buildings in a Nigerian university. *Energy and Buildings*, **130**, 721–732. URL: https://www.sciencedirect.com/science/article/pii/S0378778816307964.

Morris, C. J. G., Simmonds, I. and Plummer, N. (2001) Quantification of the influences of wind and cloud on the nocturnal urban heat island of a large city. *Journal of Applied Meteorology*, **40**, 169 – 182. URL: https://journals.ametsoc.org/view/journals/apme/40/2/1520-0450_2001_040_0169_qotiow_2.0.co_2.xml.

Nadkarni, N. M., Parker, G. G., Rinker, H. B. and Jarzen, D. M. (2004) The Nature of Forest Canopies. In *Forest Canopies (Second Edition)* (eds. M. D. Lowman and H. B. Rinker), Physiological Ecology, 3 – 23. San Diego: Academic Press, second edition edn. URL: https://doi.org/10.1016/B978-012457553-0/50005-8.

Nazarian, N., Krayenhoff, E. S. and Martilli, A. (2020) A one-dimensional model of turbulent flow through "urban" canopies (MLUCM v2.0): updates based on large-eddy simulation. *Geosci. Model Dev.*, **13**, 937–953. URL: https://doi.org/10.5194/gmd-13-937-2020.

Nielsen-Gammon, J. W., McNider, R. T., Angevine, W. M., White, A. B. and Knupp, K. (2007) Mesoscale model performance with assimilation of wind profiler data: Sensitivity to assimilation parameters and network configuration. *Journal of Geophysical Research: Atmospheres*, **112**. URL: https://agupubs.onlinelibrary.wiley.com/doi/abs/10.1029/2006JD007633.

Noilhan, J. and Planton, S. (1989) A Simple Parameterization of Land Surface Processes for Meteorological Models. *Monthly Weather Review*, **117**, 536–549. URL: https://doi.org/10.1175/1520-0493(1989)117<0536:ASPOLS>2.0.CO;2.

Nowak, D. J., Crane, D. E. and Stevens, J. C. (2006) Air pollution removal by urban trees and shrubs in the United States. *Urban Forestry and Urban Greening*, **4**, 115 – 123. URL: https://doi.org/10.1016/j.ufug.2006.01.007.

Nowak, D. J., Hirabayashi, S., Bodine, A. and Greenfield, E. (2014) Tree and forest effects on air quality and human health in the United States. *Environmental Pollution*, **193**, 119–129. URL: https://www.sciencedirect.com/science/article/abs/pii/S0269749114002395.

Ntelekos, A. A., Smith, J. A., Donner, L., Fast, J. D., Gustafson Jr, W. I., Chapman, E. G. and Krajewski, W. F. (2009) The effects of aerosols on intense convective precipitation in the northeastern United States. *Quarterly Journal of the Royal Meteorological Society*, **135**, 1367–1391. URL: https://rmets.onlinelibrary.wiley.com/doi/abs/10.1002/qj.476.

Oke, T. R. (1987) *Boundary Layer Climates*. Routledge.

— (1988a) Street design and urban canopy layer climate. *Energy and Buildings*, **11**, 103 – 113. URL: https://doi.org/10.1016/0378-7788(88)90026-6.

— (1988b) The urban energy balance. *Progress in Physical Geography*, **12**, 471–508. URL: https://doi.org/10.1177/030913338801200401.

— (1997) *Urban environments, in WG Bailey et al. (eds), The Surface Climates of Canada*. McGill-Queen's University Press.

Oke, T. R., Mills, G., Christen, A. and Voogt, J. A. (2017) *Urban Climates*. Cambridge, UK: Cambridge University Press, pp. 122-155, 168, 238-293,.

Oleson, K. W., Bonan, B., Feddema, J., Vertenstein, M. and Grimmond, C. S. (2008) An urban parameterization for a global climate model. Part 1: Formulation and evaluation for two cities. *Journal of Applied Meteorology and Climatology*, **47**, 1038–1060. URL: https://journals.ametsoc.org/view/journals/apme/47/4/2007jamc1597.1.xml.

Otte, T. L., Lacser, A., Dupont, S. and Ching, J. K. S. (2004) Implementation of an Urban Canopy Parameterization in a Mesoscale Meteorological Model. *Journal of Applied Meteorology*, **43**, 1648–1665. URL: https://doi.org/10.1175/JAM2164.1.

Park, M.-S., Ho, C.-H., Kim, J. and Elsberry, R. L. (2011) Diurnal circulations and their multi-scale interaction leading to rainfall over the South China Sea upstream of the

Philippines during intraseasonal monsoon westerly wind bursts. *Climate Dynamics*, **37**, 1483–1499. URL: https://doi.org/10.1007/s00382-010-0922-z.

Peings, Y., Saint-Martin, D. and Douville, H. (2012) A Numerical Sensitivity Study of the Influence of Siberian Snow on the Northern Annular Mode. *Journal of Climate*, **25**, 592 – 607. URL: https://journals.ametsoc.org/view/journals/clim/25/2/jcli-d-11-00038.1.xml.

Phillips, R. L., Ngugi, M. K., Hendrickson, J., Smith, A. and West, M. (2012) Mixed-Grass Prairie Canopy Structure and Spectral Reflectance Vary with Topographic Position. *Environmental Management*, **50**, 914–928. URL: https://doi.org/10.1007/s00267-012-9931-5.

von Randow, C., Manzi, A. O., Kruijt, B., de Oliveira, P. J., Zanchi, F. B., Silva, R. L., Hodnett, M. G., Gash, J. H. C., Elbers, J. A., Waterloo, M. J., Cardoso, F. L. and Kabat, P. (2004) Comparative measurements and seasonal variations in energy and carbon exchange over forest and pasture in South West Amazonia. *Theoretical and Applied Climatology*, **78**, 5–26. URL: https://link.springer.com/article/10.1007/s00704-004-0041-z.

Raupach, M. R., Antonia, R. A. and Rajagopalan, S. (1991) Rough-Wall Turbulent Boundary Layers. *Applied Mechanics Reviews*, **44**, 1–25. URL: https://doi.org/10.1115/1.3119492.

Redon, E., Lemonsu, A. and Masson, V. (2020) An urban trees parameterization for modeling microclimatic variables and thermal comfort conditions at street level with the Town Energy Balance model (TEB-SURFEX v8.0). *Geoscientific Model Development*, **13**, 385–399. URL: https://gmd.copernicus.org/articles/13/385/2020/.

Ries, H., Schlünzen, K. H., Brümmer, B., Claussen, M. and Müller, G. (2010) Impact of surface parameter uncertainties on the development of a trough in the Fram Strait region. *Tellus A*, **62**, 377–392. URL: https://onlinelibrary.wiley.com/doi/abs/10.1111/j.1600-0870.2010.00451.x.

Roberts, S. M., Oke, T. R., Grimmond, C. S. B. and Voogt, J. A. (2006) Comparison of Four Methods to Estimate Urban Heat Storage. *Journal of Applied Meteorology and Climatology*, **45**, 1766 – 1781. URL: https://doi.org/10.1175/JAM2432.1.

Ronda, R., Bruin, H. D. and Holstslag, A. (2001) Representation of the Canopy Conductance in Modeling the Surface Energy Budget for Low Vegetation. *American Meteorological Society*, **40**, 1431–1444. URL: https://doi.org/10.1175/1520-0450(2001)040<1431:ROTCCI>2.0.CO;2.

Ross, J. (1981) *The Radiation Regime and Architecture of Plant Stands*. The Hague: Dr W. Junk Publishers. URL: https://doi.org/10.1007/978-94-009-8647-3.

Rotach, M. W., Vogt, R., Bernhofer, C., Batchvarova, E., Christen, A., Clappier, A., Feddersen, B., Gryning, S.-E., Martucci, G., Mayer, H., Mitev, V., Oke, T. R., Parlow, E., Richner, H., Roth, M., Roulet, Y.-A., Ruffieux, D., Salmond, J. A., Schatzmann, M. and Voogt, J. A. (2005) BUBBLE – an Urban Boundary Layer Meteorology Project. *Theoretical and Applied Climatology*, **81**, 231–261. URL: https://doi.org/10.1007/s00704-004-0117-9.

Roth, M. (2000) Review of atmospheric turbulence over cities. *Quarterly Journal of the Royal Meteorological Society*, **126**, 941–990. URL: https://rmets.onlinelibrary.wiley.com/doi/10.1002/qj.49712656409.

Ryu, Y. H., Baik, J. J. and Lee, S. H. (2011) A new single-layer urban canopy model for use in mesoscale atmospheric models. *Journal of Applied Meteorology and Climatology*, **50**, 1773–1794. URL: https://doi.org/10.1175/2011JAMC2665.1.

Ryu, Y. H., Bou-Zeid, E., Wang, Z. H. and Smith, J. A. (2016) Realistic Representation of Trees in an Urban Canopy Model. *Boundary-Layer Meteorology*, **159**, 193–220. URL: https://link.springer.com/article/10.1007/s10546-015-0120-y.

Sailor, D. J. (2013) Energy Buildings and Urban Environment. In *Vulnerability of Energy to Climate* (ed. R. A. Pielke), 167–182. Oxford: Academic Press. URL: https://doi.org/10.1016/B978-0-12-384703-4.00321-X.

Sailor, D. J., Georgescu, M., Milne, J. M. and Hart, M. A. (2015) Development of a national anthropogenic heating database with an extrapolation for international cities. *Atmospheric Environment*, **118**, 7 – 18. URL: https://doi.org/10.1016/j.atmosenv.2015.07.016.

Salamanca, F., Martilli, A., Tewari, M. and Chen, F. (2011) A study of the urban boundary layer using different urban parameterizations and high-resolution urban canopy parameters with WRF. *Journal of Applied Meteorology and Climatology*,

50, 1107–1128. URL: https://journals.ametsoc.org/view/journals/apme/50/5/2010jamc2538.1.xml.

Salim, M. H., Schlünzen, K. H. and Grawe, D. (2015) Including trees in the numerical simulations of the wind flow in urban areas: Should we care? *Journal of Wind Engineering and Industrial Aerodynamics*, **144**, 84–95. URL: https://www.sciencedirect.com/science/article/pii/S0167610515001178.

Salim, M. H., Schlünzen, K. H., Grawe, D., Böttcher, M., Gierisch, A. M. U. and Fock, B. H. (2018) The microscale obstacle-resolving meteorological model MITRAS v2.0: model theory. *Geoscientific Model Development*, **11**, 3427–3445. URL: https://gmd.copernicus.org/articles/11/3427/2018/.

von Salzen, K., M. Claussen, M. and Schlünzen, K. H. (1996) Application of the concept of blending height to the calculation of surface fluxes in a mesoscale model. *Meteorologische Zeitschrift*, **5**, 60–66. URL: http://dx.doi.org/10.1127/metz/5/1996/60.

Santiago, J. L. and Martilli, A. (2010) A Dynamic Urban Canopy Parameterization for Mesoscale Models Based on Computational Fluid Dynamics Reynolds-Averaged Navier–Stokes Microscale Simulations. *Boundary-Layer Meteorology*, **137**, 417–439. URL: https://doi.org/10.1007/s10546-010-9538-4.

Schenk, H. and Jackson, R. (2003) *Global Distribution of Root Profiles in Terrestrial Ecosystems*. Oak Ridge, Tennessee, USA.: ORNL Distributed Active Archive Center. URL: https://doi.org/10.3334/ORNLDAAC/660.

Schlünzen, K. H. (1990) Numerical studies on the inland penetration of sea breeze fronts at a coastline with tidally flooded mudflats. *Contributions to Atmospheric Physics*, **63**, 243–256.

Schlünzen, K. H., Bungert, U., Flagg, D. D., Fock, B. H., Gierisch, A., Grawe, D., Kirschner, P., Lüpkes, C., Reinhardt, V., Ries, H., Schoetter, R., Spensberger, C. and Uphoff, M. (2012) Technical documentation of the multiscale model system M-SYS (METRAS, MITRAS, MECTM, MICTM, MESIM). MEMI Technical Report 3. Last access: 03.06.2023. URL: https://www.mi.uni-hamburg.de/en/arbeitsgruppen/memi/modelle/dokumentation/msys-technical-documentation.pdf.

Schlünzen, K. H., Böttcher, M., Fock, B. H., Gierisch, A., Grawe, D. and Salim, M. (2018) Scientific documentation of the multiscale model system M-SYS (METRAS, MITRAS, MECTM, MICTM, MESIM). MEMI Technical Report 4. Last

access: 03.06.2023. URL: https://www.mi.uni-hamburg.de/en/arbeitsgruppen/memi/modelle/dokumentation/msys-scientific-documentation-20180706.pdf.

Schlünzen, K. H. and Grawe, D. (2018) GRITOP-L Präprozessor zur Initialisierung von Topographiedaten für das Modell METRAS. METRAS Technical Report 11. Last access: 03.06.2023. URL: https://www.mi.uni-hamburg.de/en/arbeitsgruppen/memi/modelle/metras-pcl/metras-pcl-download/gritop-l-2-0-0.pdf.

Schlünzen, K. H., Grawe, D., Bohnenstengel, S. I., Schlüter, I. and Koppmann, R. (2011) Joint modelling of obstacle induced and mesoscale changes—current limits and challenges. *Journal of Wind Engineering and Industrial Aerodynamics*, **99**, 217 – 225. URL: https://doi.org/10.1016/j.jweia.2011.01.009. The Fifth International Symposium on Computational Wind Engineering.

Schlünzen, K. H., Grawe, D., Petrik, R., Schenk, E. and Weiner, O. (2019) Referenzimplementierung eines prognostischen mesoskaligen Windfeldmodells für die Ausbreitungsrechnung nach Anhang 3 der TA Luft zur Berücksichtigung von Geländeunebenheiten bei Steigungen über 1:5. Last access: 03.06.2023. URL: https://www.umweltbundesamt.de/sites/default/files/medien/1410/publikationen/2019-05-10_texte_45-2019_referenzimplementierung-windfeldmodell.pdf.

Schlünzen, K. H., Hinneburg, D., Knoth, O., Lambrecht, M., Leitl, B., Lopez, S., Lüpkes, C., Panskus, H., Renner, E., Schatzmann, M., Schoenmeyer, T., Trepte, S. and Wolke, R. (2003) Flow and transport in the obstacle layer : First results of the micro-scale model MITRAS. *Journal of Atmospheric Chemistry*, **44**, 113–130. URL: https://doi.org/10.1023/A:1022420130032.

Schlünzen, K. H., Hoffmann, P., Rosenhagen, G. and Riecke, W. (2010) Long-term changes and regional differences in temperature and precipitation in the metropolitan area of Hamburg. *International Journal of Climatology*, **30**, 1121–1136. URL: https://rmets.onlinelibrary.wiley.com/doi/abs/10.1002/joc.1968.

Schlünzen, K. H. and Katzfey, J. J. (2003) Relevance of sub-grid-scale land-use effects for mesoscale models. *Tellus A: Dynamic Meteorology and Oceanography*, **55**, 232–246. URL: https://doi.org/10.3402/tellusa.v55i3.12095.

Schraff, C., Reich, H., Rhodin, A., Schomburg, A., Stephan, K., Periáñez, A. and Potthast, R. (2016) Kilometre-scale ensemble data assimilation for the COSMO model

(KENDA). *Quarterly Journal of the Royal Meteorological Society*, **142**, 1453–1472. URL: https://rmets.onlinelibrary.wiley.com/doi/abs/10.1002/qj.2748.

Schraff, C. H. (1997) Mesoscale data assimilation and prediction of low stratus in the Alpine region. *Meteorology and Atmospheric Physics*, **64**, 21–50. URL: https://doi.org/10.1007/BF01044128.

Seinfeld, J. H. (1989) Urban Air Pollution: State of the Science. *Science*, **243**, 745–752. URL: https://www.science.org/doi/10.1126/science.243.4892.745.

Sellers, P., Randall, D., Collatz, G., Berry, J., Field, C., Dazlich, D., Zhang, C., Collelo, G. and Bounoua, L. (1996) A Revised Land Surface Parameterization (SiB2) for Atmospheric GCMS. Part I: Model Formulation. *Journal of Climate*, **9**, 676 – 705. URL: https://doi.org/10.1175/1520-0442(1996)009<0676:ARLSPF>2.0.CO;2.

Sellers, P. J., Mintz, Y., Sud, Y. C. and Dalcher, A. (1986) A Simple Biosphere Model (SIB) for Use within General Circulation Models. *Journal of the Atmospheric Sciences*, **43**, 505–531. URL: https://doi.org/10.1175/1520-0469(1986)043<0505:ASBMFU>2.0.CO;2.

Sharma, A., Wuebbles, D. J. and Kotamarthi, R. (2021) The need for urban-resolving climate modeling across scales. *AGU Advances*, **2**, e2020AV000271. URL: https://agupubs.onlinelibrary.wiley.com/doi/abs/10.1029/2020AV000271. E2020AV000271 2020AV000271.

Shepherd, J. M. (2005) A Review of Current Investigations of Urban-Induced Rainfall and Recommendations for the Future. *Earth Interactions*, **9**, 1 – 27. URL: https://journals.ametsoc.org/view/journals/eint/9/12/ei156.1.xml.

Siebert, S., Döll, P., Feick, S., Hoogeveen, J., Faures, J. and Frenken, K. (2007) The Global Map of Irrigation Areas. Johann Wolfgang Goethe University, Frankfurt am Main, Germany/Food and Agriculture Organization of the United Nations, Rome, Italy.

Skamarock, W. C., Klemp, J. B., Dudhia, J., Gill, D. O., Liu, Z., Berner, J., Wang, W., Powers, J. G., Duda, M. G., Barker, D. M. and Huang, X.-Y. (2019) A Description of the Advanced Research WRF Version 4. (No. NCAR/TN-556+STR). URL: http://dx.doi.org/10.5065/1dfh-6p97.

Solman, S. A. and Pessacg, N. L. (2012) Regional climate simulations over South America: sensitivity to model physics and to the treatment of lateral boundary conditions using

the MM5 model. *Climate Dynamics*, **38**, 281–300. URL: https://doi.org/10.1007/s00382-011-1049-6.

Srinivas, C. V., Yesubabu, V., Venkatesan, R. and Ramarkrishna, S. S. V. S. (2010) Impact of assimilation of conventional and satellite meteorological observations on the numerical simulation of a Bay of Bengal Tropical Cyclone of November 2008 near Tamilnadu using WRF model. *Meteorology and Atmospheric Physics*, **110**, 19–44. URL: https://doi.org/10.1007/s00703-010-0102-z.

Stauffer, D. R., Seaman, N. L. and Binkowski, F. S. (1991) Use of Four-Dimensional Data Assimilation in a Limited-Area Mesoscale Model Part II: Effects of Data Assimilation within the Planetary Boundary Layer. *Monthly Weather Review*, **119**, 734 – 754. URL: https://journals.ametsoc.org/view/journals/mwre/119/3/1520-0493_1991_119_0734_uofdda_2_0_co_2.xml.

Stensrud, D. J. and Bao, J.-W. (1992) Behaviors of Variational and Nudging Assimilation Techniques with a Chaotic Low-Order Model. *Monthly Weather Review*, **120**, 3016 – 3028. URL: https://journals.ametsoc.org/view/journals/mwre/120/12/1520-0493_1992_120_3016_bovana_2_0_co_2.xml.

Sterling, S. M., Ducharne, A. and Polcher, J. (2013) The impact of global land-cover change on the terrestrial water cycle. *Nature Climate Change*, **3**, 385–390. URL: https://doi.org/10.1038/nclimate1690.

Stewart, I. D. and Oke, T. R. (2012) Local climate zones for urban temperature studies. *Bulletin of the American Meteorological Society*, **93**, 1879–1900. URL: https://doi.org/10.1175/BAMS-D-11-00019.1.

Stull, R. B. (1988) *An Introduction to Boundary Layer Meteorology.* Kluwer Academic, Dordrecht, pp. 115-149. URL: https://link.springer.com/book/10.1007/978-94-009-3027-8.

Teuling, A. J., Seneviratne, S. I., Stöckli, R., Reichstein, M., Moors, E., Ciais, P., Luyssaert, S., van den Hurk, B., Ammann, C., Bernhofer, C., Dellwik, E., Gianelle, D., Gielen, B., Grünwald, T., Klumpp, K., Montagnani, L., Moureaux, C., Sottocornola, M. and Wohlfahrt, G. (2010) Contrasting response of European forest and grassland energy exchange to heatwaves. *Nature Geoscience*, **3**, 722–727. URL: https://www.nature.com/articles/ngeo950.

Trusilova, K., Früh, B., Brienen, S., Walter, A., Masson, V., Pigeon, G. and Becker, P. (2013) Implementation of an Urban Parameterization Scheme into the Regional Climate Model COSMO-CLM. *Journal of Applied Meteorology and Climatology*, **52**, 2296–2311. URL: https://doi.org/10.1175/JAMC-D-12-0209.1.

UN (2019) World urbanization prospects: The 2018 revision (ST/ESA/SER.A/420). United Nations, Department of Economic and Social Affairs, Population Division. Last access: 03.06.2023. URL: https://population.un.org/wup/Publications/Files/WUP2018-Report.pdf.

van den Heever, S. C. and Cotton, W. R. (2007) Urban aerosol impacts on downwind convective storms. *Journal of Applied Meteorology and Climatology*, **46**, 828–850. URL: http://www.jstor.org/stable/26171943.

van Heerwaarden, C. C. and Teuling, A. J. (2014) Disentangling the response of forest and grassland energy exchange to heatwaves under idealized land–atmosphere coupling. *Biogeosciences*, **11**, 6159–6171. URL: https://bg.copernicus.org/articles/11/6159/2014/bg-11-6159-2014.html.

Velasco, E., Márquez, C., Bueno, E., Bernabé, R. M., Sánchez, A., Fentanes, O., Wöhrnschimmel, H., Cárdenas, B., Kamilla, A., Wakamatsu, S. and Molina, L. T. (2008) Vertical distribution of ozone and VOCs in the low boundary layer of Mexico City. *Atmospheric Chemistry and Physics*, **8**, 3061–3079. URL: https://acp.copernicus.org/articles/8/3061/2008/.

Vinodkumar, Chandrasekar, A., Alapaty, K. and Niyogi, D. (2008) The Impacts of Indirect Soil Moisture Assimilation and Direct Surface Temperature and Humidity Assimilation on a Mesoscale Model Simulation of an Indian Monsoon Depression. *Journal of Applied Meteorology and Climatology*, **47**, 1393 – 1412. URL: https://journals.ametsoc.org/view/journals/apme/47/5/2007jamc1599.1.xml.

Voss, V. (2023) High resolution obstacle-resolved model results for the city centre of Hamburg, Germany, from the microscale transport and stream model MITRAS on 21 June 2000. URL: https://www.wdc-climate.de/ui/entry?acronym=MITRAS_ATMODAT.

Vuckovic, M., Loibl, W., Tötzer, T. and Stollnberger, R. (2019) Potential of urban densification to mitigate the effects of heat island in vienna, austria. *Environments*, **6**. URL: https://www.mdpi.com/2076-3298/6/7/82.

Walko, R. L., Band, L. E., Baron, J., Kittel, T. G. F., Lammers, R., Lee, T. J., Ojima, D., Pielke, R. A., Taylor, C., Tague, C., Tremback, C. J. and Vidale, P. L. (2000) Coupled Atmosphere–Biophysics–Hydrology Models for Environmental Modeling. *Journal of Applied Meteorology*, **39**, 931–944. URL: https://doi.org/10.1175/1520-0450(2000)039<0931:CABHMF>2.0.CO;2.

Wang, C., Wang, Z.-H. and Ryu, Y.-H. (2021) A single-layer urban canopy model with transmissive radiation exchange between trees and street canyons. *Building and Environment*, **191**, 107593. URL: https://www.sciencedirect.com/science/article/pii/S0360132321000093.

Wang, H., Liu, Y., Zhao, T., Liu, Y., Xu, M., Shen, S., Jiang, Y., Yang, H. and Feng, S. (2018) Continuous assimilation of lightning data using time-lagged ensembles for a convection-allowing numerical weather prediction model. *Journal of Geophysical Research: Atmospheres*, **123**, 9652–9673. URL: https://agupubs.onlinelibrary.wiley.com/doi/abs/10.1029/2018JD028494.

Wang, L., Gao, Z., Miao, S., Guo, X., Sun, T., Liu, M. and Li, D. (2015) Contrasting characteristics of the surface energy balance between the urban and rural areas of Beijing. *Advances in Atmospheric Sciences*, **32**, 505–514. URL: https://link.springer.com/article/10.1007/s00376-014-3222-4.

Wang, Z.-H. (2014) Monte Carlo simulations of radiative heat exchange in a street canyon with trees. *Solar Energy*, **110**, 704 – 713. URL: https://doi.org/10.1016/j.solener.2014.10.012.

Wang, Z. H., Bou-Zeid, E. and Smith, J. A. (2013) A coupled energy transport and hydrological model for urban canopies evaluated using a wireless sensor network. *Quarterly Journal of the Royal Meteorological Society*, **139**, 1643–1657. URL: https://rmets.onlinelibrary.wiley.com/doi/full/10.1002/qj.2032.

Wedi, N. P., Polichtchouk, I., Dueben, P., Anantharaj, V. G., Bauer, P., Boussetta, S., Browne, P., Deconinck, W., Gaudin, W., Hadade, I., Hatfield, S., Iffrig, O., Lopez, P., Maciel, P., Mueller, A., Saarinen, S., Sandu, I., Quintino, T. and Vitart, F. (2020) A baseline for global weather and climate simulations at 1 km resolution. *Journal of Advances in Modeling Earth Systems*, **12**, e2020MS002192. URL: https://agupubs.onlinelibrary.wiley.com/doi/abs/10.1029/2020MS002192. E2020MS002192 10.1029/2020MS002192.

Wicke, W. and Bernhofer, C. (1996) Energy balance comparison of the Hartheim forest and an adjacent grassland site during the HartX experiment. *Theoretical and Applied Climatology*, **53**, 49–58. URL: https://link.springer.com/article/10.1007/BF00866410.

WMO (2023) Guidance on Measuring, Modelling and Monitoring the Canopy Layer Urban Heat Island (CL-UHI). Schlünzen, K. H., Grimmond, S. and Baklanov, A. (edts), World Meteorological Organization, WMO-No. 1292. URL: https://library.wmo.int/doc_num.php?explnum_id=11537.

Wouters, H., Demuzere, M., Blahak, U., Fortuniak, K., Maiheu, B., Camps, J., Tielemans, D. and van Lipzig, N. P. M. (2016) The efficient urban canopy dependency parametrization (SURY) v1.0 for atmospheric modelling: description and application with the COSMO-CLM model for a Belgian summer. *Geoscientific Model Development*, **9**, 3027–3054. URL: https://gmd.copernicus.org/articles/9/3027/2016/.

WUDAPT (2020) Geopedia-World Urban Database and Access Portal Tools. Last access: 03.06.2023. URL: https://geopedia.world/#T4_x1122936.3825375163_y7087011.951516682_s10_b2345.

Xiao, Q. and McPherson, E. G. (2002) Rainfall interception by Santa Monica's municipal urban forest. *Urban Ecosystems*, **6**, 291–302. URL: https://link.springer.com/article/10.1023/B:UECO.0000004828.05143.67.

Yamada, T. (1982) A Numerical Model Study of Turbulent Airflow in and Above a Forest Canopy. *Journal of the Meteorological Society of Japan. Ser. II*, **60**, 439–454. URL: https://doi.org/10.2151/jmsj1965.60.1_439.

Yang, X. and Li, Y. (2015) The impact of building density and building height heterogeneity on average urban albedo and street surface temperature. *Building and Environment*, **90**, 146–156. URL: https://www.sciencedirect.com/science/article/pii/S0360132315001559.

Yazid, A. W. M., Sidik, N. A. C., Salim, S. M. and Saqr, K. M. (2014) A review on the flow structure and pollutant dispersion in urban street canyons for urban planning strategies. *SIMULATION*, **90**, 892–916. URL: https://doi.org/10.1177/0037549714528046.

Yoo, C., Cho, E., Na, W., Kang, M. and Lee, M. (2021) Change of rainfall–runoff processes in urban areas due to high-rise buildings. *Journal of Hydrology*, **597**, 126155. URL: https://www.sciencedirect.com/science/article/pii/S002216942100202X.

Zeng, P. and Takahashi, H. (2000) A first-order closure model for the wind flow within and above vegetation canopies. *Agricultural and Forest Meteorology*, **103**, 301 – 313.

Zhang, G. J., Cai, M. and Hu, A. (2013) Energy consumption and the unexplained winter warming over northern Asia and North America. *Nature Climate Change*, **3**, 466–470. URL: https://doi.org/10.1038/nclimate1803.

Zou, X., Navon, I. M. and Ledimet, F. X. (1992) An optimal nudging data assimilation scheme using parameter estimation. *Quarterly Journal of the Royal Meteorological Society*, **118**, 1163–1186. URL: https://rmets.onlinelibrary.wiley.com/doi/abs/10.1002/qj.49711850808.

Zängl, G., Reinert, D., and Prill, F. (2022) Grid refinement in ICON v2.6.4. *Geoscientific Model Development*, **15**, 7153–7176. URL: https://doi.org/10.5194/gmd-15-7153-2022.

Eidesstattliche Versicherung

Hiermit erkläre ich an Eides statt, dass ich die vorliegende Dissertationsschrift selbst verfasst und keine anderen als die angegebenen Quellen und Hilfsmittel benutzt habe.

Ort, den	Unterschrift